COLLEGE DOCTORAL PAYS DE LA LOIRE
ED MATIERE, MOLECULES MATERIAUX ET GEOSCIENCES

université angers

NICOLAUS COPERNICUS UNIVERSITY IN TORUŃ
Doctoral Schools

THESE DE DOCTORAT

L'UNIVERSITÉ D'ANGERS
SOUS LE SCEAU DE
LA COMUE ANGERS – LE MANS

ECOLE DOCTORALE N° 596
Matičre, Molécules, Matériaux et Géosciences
Spécialité: Sciences des Matériaux

NICOLAUS COPERNICUS UNIVERSITY IN TORUŃ

DOCTORAL SCHOOL AT THE NICOLAUS COPERNICUS UNIVERSITY IN TORUŃ
Doctoral School of Exact and Natural Sciences
Speciality: Physical Sciences

Par
Agnieszka MARJANOWSKA

Photovoltaic and nonlinear optical effects of thin films based on perovskites

Thèse présentée et soutenue à Toruń, Pologne, 2026
Unité de recherche: Laboratoire de Photonique d'Angers (LPhiA), EA 4464
Institute of Physics, Faculty of Physics, Astronomy and Informatics (NCU, Poland)

Rapporteurs avant soutenance:

Composition du Jury:

Examinateurs:

Dir. de thèse:	Anna Zawadzka	Professor, Nicolaus Copernicus University in Toruń, Toruń, Poland
	Bouchta Sahraoui	Professor, University of Angers, Angers, France

NICOLAUS COPERNICUS UNIVERSITY IN TORUŃ
Institute of Physics
Faculty of Physics, Astronomy and Informatics
Doctoral School of Exact and Natural Sciences
Scientific discipline: Physical Sciences

UNIVERSITY OF ANGERS
Laboratoire de Photonique d'Angers
Ecole Doctorale Matičre, Molécules, Matériaux et Géosciences
Scientific discipline: Sciences des Matériaux

Photovoltaic and nonlinear optical effects of thin films based on perovskites

---

Agnieszka Marjanowska

MSc in Technical Physics

Thesis supervised by Dr hab. Anna Zawadzka, Prof. NCU, Institute of Physics,
Nicolaus Copernicus University in Toruń, Poland,
and Prof. Bouchta Sahraoui, University of Angers, France

Thesis written in the *cotutelle* system between
Nicolaus Copernicus University in Toruń, Poland, and the University of Angers, France

Dissertation submitted in total fulfillment
of the requirements for the degree of
DOCTOR OF PHYSICS

Toruń 2025

The doctoral project was carried out in a *cotutelle* system between Nicolaus Copernicus University in Toruń, Poland, and the University of Angers, France, thanks to the French Government's scholarship program – Doctorate 2022. Funding and support were received from the French Embassy in Poland and Campus France Pologne.

ACKNOWLEDGEMENTS

Completing this doctoral dissertation marks an important stage of my scientific journey, made possible thanks to the support, understanding, and kindness of many people. I sincerely thank everyone who contributed to the completion of this project.

First and foremost, I would like to thank **Prof. Anna Zawadzka** and **Prof. Bouchta Sahraoui**, my thesis directors. Your knowledge, insightful remarks, continuous support, and commitment have shaped the direction of my research, given me the courage to take on new challenges, and provided the confidence to overcome the difficulties along the way.

I am grateful to the members of the Laboratory of Low-Dimensional Structures in Toruń and the LPhiA laboratory for creating a friendly and inspiring research environment. I sincerely thank **Dr Przemysław Płóciennik** and **Dr Krzysztof Wisniewski** from the Laboratory of Low-Dimensional Structures for all the valuable advice and technical guidance I received during our collaboration. Working with you was an unforgettable experience. I also wish to thank **Dr Said Taboukhat**, **Dr Dominique Guichaoua**, and **Dr Houda El Karout** from the LPhiA group, who were always available to help and share their expertise in nonlinear optics.

I also thank the **French Embassy in Poland** and **Campus France** for the opportunity to complete my doctoral dissertation under the cotutelle system, for their financial support, and for their valuable mentoring during my international experience.

I thank **Prof. Anna Migalska-Zalas** and **Dr Abdelkrim El-Ghayoury** for monitoring my progress throughout my studies and for all the constructive comments, kindness, and understanding I experienced during our meetings.

I cannot forget **MSc Agnieszka Górska-Pukownik**, secretary of the Doctoral School of Exact and Natural Sciences, whose constant kindness and administrative support ensured the smooth running of my studies. Thank you for your commitment and understanding, which I experienced numerous times.

I also thank my Friends from the lab – **Amina**, **Houda**, **Oumaima**, **Julien**, and **Mateusz**. Your presence throughout this journey was invaluable. **Amina** and **Houda** – you were a tremendous support every step of the way. The countless hours spent together in the lab, your help, and your positive energy will remain in my memory. **Oumaima**, **Julien**, and **Mateusz** – your presence allowed me to balance work and everyday life, and your sense of humor brightened every day in the lab.

I also extend my deepest gratitude to my **Family** and **Friends** for their constant support, faith, motivation, understanding, and help. Special thanks to my **Parents**, **Natalia**, **Gosia**, **Arek**, and **Paulina** – your faith in me gave me the strength to see this project through to the end.

To all those who contributed in any way to the creation of this dissertation - both those mentioned here and those who cannot be named - I offer my sincere thanks. Thank you.

CONTENTS

INTRODUCTION

In recent years, modern optoelectronics has focused on finding materials that combine high energy conversion efficiency with exceptional optical properties. Among these materials are hybrid perovskites. Thanks to their unique properties, such as light absorption, long carrier diffusion length, the ability to design and chemically synthesize materials, and thus the ability to precisely tailor photo-optical and electrical properties to specific applications, they have found application in next-generation photovoltaics. Perovskite structures can also exhibit nonlinear optical responses, making them attractive materials for nonlinear optics and photonics applications. Despite the significant interest in perovskites, which has increased significantly over the past decade, their fundamental optoelectric properties are poorly understood enough to be implemented successfully in comprehensive optoelectronic solutions. This monograph describes the relationships between the structure of perovskite thin films and their photovoltaic and nonlinear properties. It also discusses research on surface topography, the influence of external factors on optical and structural properties, and phase transitions in low-dimensional perovskite structures.

This dissertation explains the theoretical principles of photovoltaics (*Chapter 1*) and nonlinear optics (*Chapter 2*). The chapter on photovoltaics provides a comprehensive description of energy band models for inorganic and organic materials, with special attention paid to the semiconductor *p-n* junction, the fundamental optoelectronic element in solar cells. *Chapter 1* also details the structural and electrical model of photovoltaics, the classification of photovoltaic cells, including perovskite photovoltaic cells, a description of electrical parameters characterizing cell operation, and current advances in photovoltaic technology. *Chapter 2* explains the origin of optical nonlinear effects. This chapter discusses the wave equation, which describes light propagation in various media. Then it presents the sources of second- and third-order nonlinear optical effects, culminating in a description of nonlinear absorption and nonlinear changes in the refractive index. This section also describes NLO applications in various fields, such as photonics, telecommunications, medicine, and quantum technologies. The theoretical background presented in *Chapters 1* and *2* is essential for a proper understanding of the content of the subsequent chapters.

Chapter 3 describes experimental techniques for obtaining perovskite thin films and investigating their structural, optical, and photovoltaic properties. The methods discussed include a detailed description of the PVco-D technique used to get all the thin film structures studied in this work. The following sections present all measurement techniques used in the research. These include descriptions of the AFM technique with details of MFs, standard UV-VIS-NIR spectroscopy, PL measurements, UV-VIS-NIR and PL spectroscopic measurements as a function of temperature, and measurements used to conduct aging tests of samples. The chapter also provides a detailed description of the measurement equipment used to measure nonlinear optical effects and selected theoretical models, knowledge of which is necessary for calculating second- and third-order nonlinear electrical susceptibility. *Chapter 3* concludes with an explanation of the electrical measurement technique used to determine the photovoltaic parameters of solar cells.

The next section presents research results on photovoltaics and nonlinear optics phenomena. *Chapter 4* begins with a discussion of the general properties of the studied materials, i.e., perovskites, followed by a description of the preparation of thin films of hybrid perovskites using the PVco-D technique. This section identifies perovskites with specific chemical structures. Since 14 samples were tested, each was assigned a specific designation (I.1-I.7, Cl.1-Cl.3, Br.1-Br.4) to simplify the nomenclature. Subsequent subsections of *Chapter 4* provide the results of AFM structural studies, UV-VIS-NIR spectroscopic studies, aging tests, phase transition studies, and nonlinear optical effects (SHG, THG, and Z-scan). The chapter concludes by describing the designed photovoltaic structures and the results of electrical tests used to determine the parameters characterizing these photovoltaic cells. *Chapter 4* is organized to compare a given property across all the samples studied. Each subsection describing a given property concludes with a summary that compares the results obtained for all the perovskites studied.

The dissertation ends with a concise summary, including a comprehensive analysis of the obtained experimental data, final conclusions, and perspectives for future research directions on perovskite materials in the context of photovoltaics and nonlinear optics applications.

CHAPTER 1: PHOTOVOLTAICS

Photovoltaics enable the conversion of solar radiation energy into electricity through the internal photoelectric phenomenon. It is one of the fastest-growing areas of renewable energy in the world. *Chapter 1* contains basic information related to photovoltaics. It discusses what a solar cell is and the mechanisms enabling electric current and voltage generation. This section also looks at the materials used in photovoltaics, the construction of photovoltaic cells, and the parameters describing their operation.

1.1. Inorganic materials

Inorganic materials are currently the most popular materials used in photovoltaic cells. They are the most important component of inorganic photovoltaic cells, characterized by high efficiency, durability, and reliability. The best-known inorganic photovoltaic cells are the standard silicon photovoltaic cells. Other well-known inorganic materials that have been used for many years to manufacture photovoltaic cells are cadmium telluride, copper, indium, gallium, selenium, as well as oxides of zinc, titanium, tin, and many others [1,2]. The materials' mechanical, optical, and electrical properties are determined by the crystal structure, i.e., the crystal lattice of interacting atoms.

The interaction of atoms in the crystal lattice of a material results in the formation of electron energy bands. The simplest energy band model assumes three bands – the valence band, the energy gap, and the conduction band, along with the Fermi energy level E_F (Figure 1.1). Due to the Pauli exclusion principle, the valence band is filled with electrons that are not allowed to move. The energy gap has no energy levels, so electrons cannot reside there. In contrast, in the conduction band, there are no electrons in the atom's ground state. In the excited state of the atom, as a result of sufficiently high energy being supplied, it is possible to transfer an electron from the valence band to the conduction band. The difference in energy between the bottom of the conduction band and the top of the valence band determines the width of the forbidden band and is called the energy gap E_g. E_F is the theoretical energy level of an electron for which the probability of occupying the valence and conduction bands is 50%. To release an electron from the valence band and move it to the conduction band, the energy supplied from outside to the atom must be equal

to or greater than E_g. As a result of the release of an electron in the valence band, a hole is created (equivalent to the formation of a positively charged ion), which is called the generation of electron-hole pairs. An electron transferred to the conduction band moves freely, but chaotically, in the conduction band. Applying an external voltage to the material brings order to the movement of the charges, causing current to flow. Based on a simplified energy band model and depending on the E_g value, inorganic materials are divided into conductors ($E_g = 0$), semiconductors ($E_g < 3\,eV$), and insulators ($E_g > 3\,eV$) [3]. From the point of view of the present work, semiconducting materials are of particular interest, and it is to them that more attention is paid.

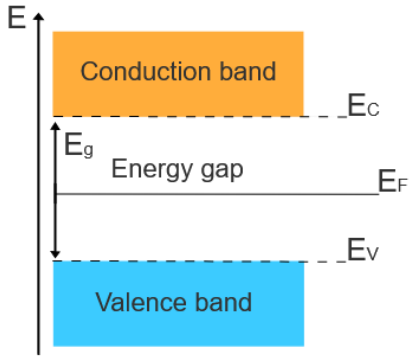

Figure 1.1. General energy band model of inorganic materials; E – Energy, E_C – Conduction band edge energy level, E_V – Valence band edge energy level, E_F – Fermi energy level, E_g – Energy gap.

1.1.1. Energy band model of semiconductors

The division of elemental semiconductors comprises undoped (intrinsic) and doped semiconductors. Undoped semiconductors are pure materials without defects or dopants in the crystal structure. In the excited state, the number of electrons and holes generated in an undoped semiconductor are equal, and the E_F lies precisely in the centre of the band gap. Doped semiconductors are created by deliberately replacing an atom in the semiconductor's crystal lattice with another atom. The changes made to the material's crystal lattice are synonymous with modifications to their physico-chemical properties. Depending on the type of dopant introduced, a distinction is made between *p-type* and *n-type* semiconductors. Introducing acceptor dopants into the material causes a shortage of electrons,

and holes are generated. Such a semiconductor is conducted using holes, which are the majority of charges, and is called a *p-type* semiconductor. An *n-type* semiconductor is created by introducing donor dopants into the material, causing excess electrons. It is conducted using electrons, which comprise most of the charges. Introducing dopants creates an additional energy level - the acceptor level E_A in the case of *p-type* doping and the donor level E_D in the case of *n-type* doping. Doping also shifts the position of the E_F [4]. The acceptor level stores electrons that can pass into it from the valence band, while the donor level stores excess electrons from the conduction band. Band models of intrinsic and doped semiconductors at T = 0 K, containing the additional energy levels described above, are shown in Figure 1.2.

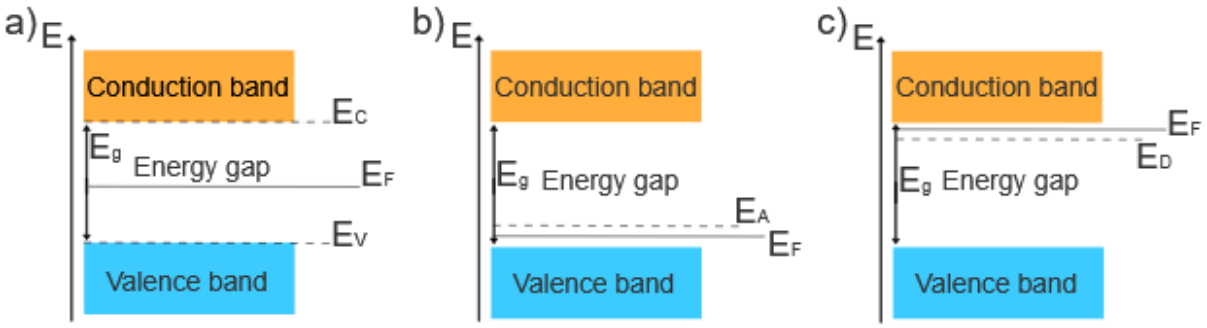

Figure 1.2. Energy band model of a semiconductor at T = 0 K: intrinsic (a), *p-type* doped (b), *n-type* doped (c); E – Energy, E_C – Conduction band edge energy level, E_V – Valence band edge energy level, E_F – Fermi energy level, E_g – Energy gap, E_A - Acceptor level, E_D - Donor level.

The above figure refers to intrinsic and doped semiconductors at T = 0 K. When T increases, the position E_F in doped semiconductors shifts on the energy scale, as some electrons are thermally excited into the conduction band. Their band energy models for T ≠ 0 K are shown in Figure 1.3.

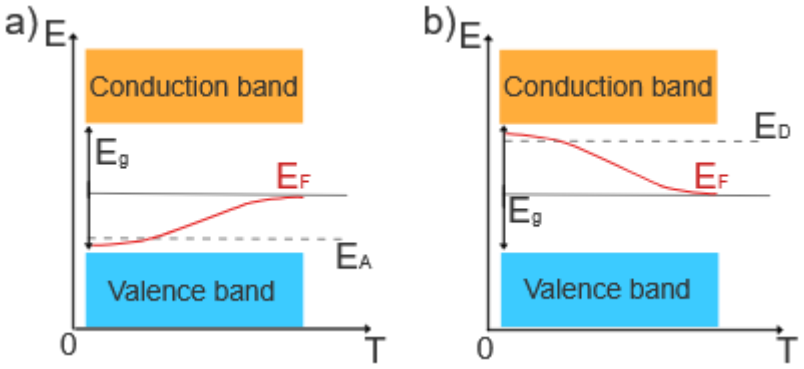

Figure 1.3. Energy band model of a semiconductor at T ≠ 0 K: *p-type* doped (a), *n-type* doped (b); E – Energy, E_F – Fermi energy level, E_g – Energy gap, E_A - Acceptor level, E_D - Donor level.

1.1.2. Semiconductor *p-n* junction

The purpose of using solar cells is to generate voltage and electric current. To explain how a photovoltaic cell generates an electrical voltage, it is necessary to look at the operation of the *p-n* junction, which is the fundamental element of a photovoltaic cell and a semiconductor diode.

A *p-n* junction combines *p-type* and *n-type* semiconductors. *P-type* and *n-type* semiconductors contain majority and minority carriers. The majority carriers in *p-type* semiconductors are holes, while the minority carriers are electrons. In *n-type* semiconductors, the majority carriers are electrons, and the minority carriers are holes. When a *p-type* and an *n-type* semiconductor are combined, a *p-n* junction is formed at the junction boundary. Due to the significant difference in concentration of the mobile charge carriers, i.e., a high concentration of holes on the *p* side and a high concentration of electrons on the *n* side, a diffusion process takes place from the *n* to the *p* area for electrons and from the *p* to the *n* area for holes. As a result of the separation of electrons and holes in the *p-n* junction area, an electric field is created, creating a so-called potential barrier, also called a depleted layer, which prevents further diffusion of the majority carriers. The abovementioned situation is where an external voltage does not polarize the *p-n* junction. Figure 1.4 shows the *p-n* junction and its energy band models in three situations: when it is not polarized, when it is polarized in the forward bias, and when it is polarized in the reverse bias.

Polarization in the forward bias is the attachment of an external electrical voltage to the *p-n* junction, such that the positive potential connects to the *p* part and the negative potential to the *n* part. In this situation, the potential barrier of the junction decreases with the value of the external voltage applied, and the width of the *p-n* junction area decreases. Electrons from the *p* area flow into the positive electrode, and electrons from the negative electrode are injected into the *n* area, where current flows through the junction. Polarization in the reverse bias is the attachment of an external electrical voltage to the *p-n* junction, such that the positive potential connects to the *n* part and the negative potential to the *p* part. It causes an increase in the potential barrier and the width of the *p-n* junction. The flow of majority carriers is impeded, and only a small minority carrier current flows through the junction, which is called the reverse current. About the bandgap energy model of the *p-n* junction, it should be noted that after the formation of the *p-n* junction, the Fermi levels are aligned, resulting in the curvature of the valence and conduction levels in the depleted region. Depending on the type of external polarization of the junction, its energy band model changes, as schematically shown in Figure 1.4.

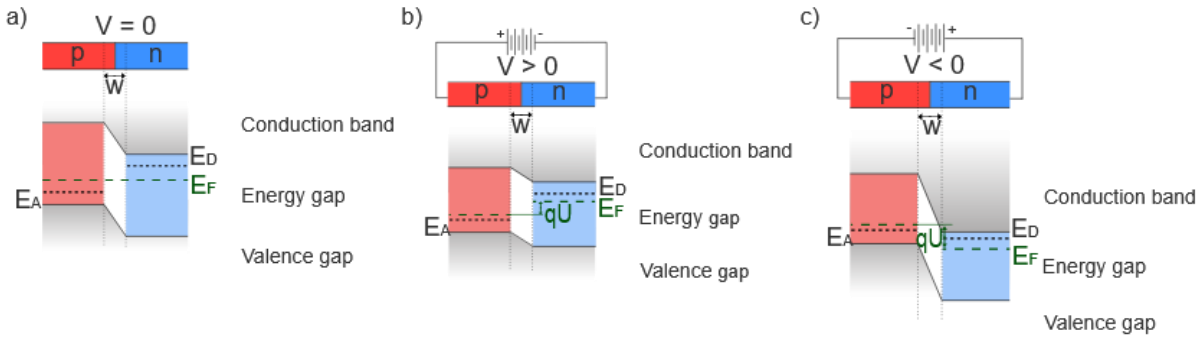

Figure 1.4. The *p-n* junction and its energy band model at T ≠ 0 K in the case of no external bias (a), forward bias (b), and reverse bias (c); V - External bias voltage, w - Width of the *p-n* junction, q – Elementary charge, E_F - Fermi energy level, E_A - Acceptor level, E_D - Donor level.

The *p-n* junction is distinguished by its current-voltage (I-V) characteristics among many electronic devices. This is a typical diode characteristic (Figure 1.5a) and is described by the Shockley equation (Eq. 1.1). From a physical point of view, the I-V characteristic reads out basic information about the conduction of a given junction.

For positive voltages ($V > 0$), the *p-n* junction is conducting. From the I-V characteristic, one can read the so-called threshold voltage, above which the current rapidly increases. For negative voltages ($V < 0$), only a small saturation current I_S flows through the junction, and the junction acts as a barrier. If the stop voltage exceeds a particular critical value, a so-called junction breakdown will occur, which causes an avalanche effect and can lead to damage to the *p-n* junction. For example, the junction avalanche effect is induced intentionally in Zener diodes [5]. The threshold and breakdown voltages depend on the *p-n* junction material and are characteristic quantities.

$$I = I_S\left(e^{\frac{qV}{nkT_K}} - 1\right) \qquad \text{(Eq. 1.1)}$$

I_S – saturation current of the *p-n* junction

q – elementary charge

V – external bias voltage

n – diode ideality factor

k – Boltzmann constant

T_K – absolute temperature

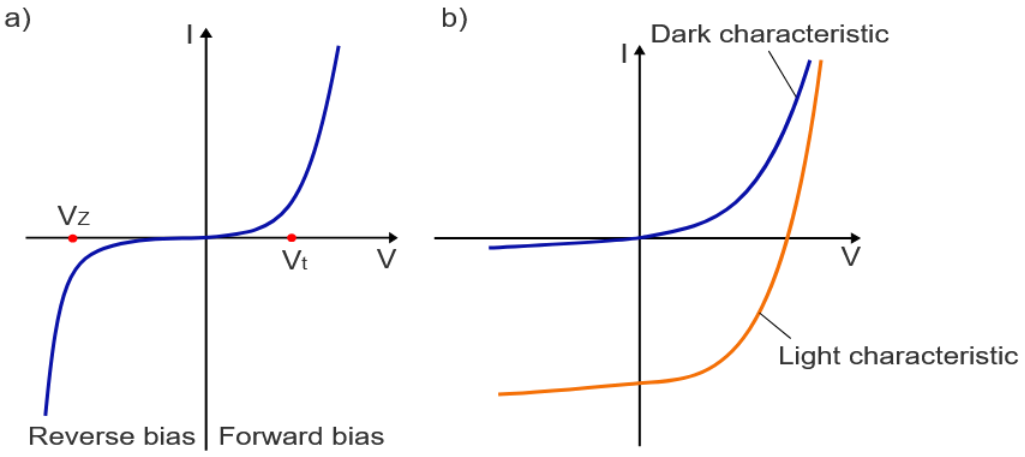

Figure 1.5. I-V characteristics of a *p-n* junction – Zener diode characteristic (a), and a photovoltaic cell - dark and light characteristics (b); V_Z - Zener voltage, V_t - threshold voltage.

As mentioned above, the *p-n* junction is the fundamental element of a photovoltaic cell, so the operation of the cell can also be described based on its I-V characteristics. When a photovoltaic cell is illuminated, energy in the form of radiation quanta is supplied to the crystal lattice atoms. Absorption of the incident electromagnetic radiation occurs in both the *p-type* and *n-type* regions. The energy supply at least equal to E_g to the crystal lattice can transfer electrons to the conduction band. This generates additional electron-hole pairs called excitons, which decay into a free electron and a hole and later participate in conduction according to the principles described above for the *p-n* junction. Once the photocell is polarized, an electric current will flow through it, and the I-V characteristic will look very similar to a diode. The I-V characteristics of the unlit and lit photovoltaic cells are shown in Figure 1.5b and are referred to as the dark and light characteristics, respectively.

The amount of electromagnetic radiation absorbed by a photovoltaic cell depends, among other things, on the size of the energy gap [6]. The quality of the photovoltaic device also influences how much incident light is converted into electricity. This is because the conversion process is subject to losses, which result, among other things, from reflection and transmission of incident light onto the photovoltaic cell, recombination and charge mobility limitations, or resistance at the semiconductor-electrode interface [7,8].

1.2. Organic materials

In addition to inorganic materials, organic materials are used in photovoltaics - most commonly conjugated polymers, fullerene derivatives, and non-fullerene materials [9-11]. Like inorganic semiconductors, they can absorb electromagnetic radiation and conduct. Unlike inorganic materials, they are composed of organic molecules. Thanks to these materials, photovoltaic cells can be flexible, lightweight, and transparent. It all depends on the properties of the specific material.

From the point of view of photovoltaic applications, an interesting aspect is the energy structure and conductivity of organic materials. Energy levels characterize each molecule of an organic material. At equilibrium, all levels are occupied up to the highest occupied orbital, the Highest Occupied Molecular Orbital (HOMO), and above this are the unoccupied energy levels. The lowest unoccupied level is called the Lowest Unoccupied Molecular Orbital (LUMO). The energy levels below the HOMO and above the LUMO are considered equivalent to the valence and conduction bands. The energy region between the HOMO and LUMO levels is comparable to the energy gap E_g. To illustrate the situation described, the energy structure of a single organic molecule is shown in Figure 1.6a. When a photon of at least E_g energy falls on an organic molecule, an electron from the HOMO level is excited to the LUMO level. In this way, an exciton is generated. An exciton, or electron-hole pair, compared to an inorganic semiconductor, is strongly electrostatically bonded to each other and can move through the material. When two organic molecules, acceptor and donor, with different HOMO and LUMO levels are joined, a potential difference will be created. Due to diffusion, the exciton will move towards the interface of the molecules, and there, thanks to the potential difference, the exciton bond will be broken, and the electron-hole pair will be separated. The electron will jump from the LUMO level of the donor to the LUMO level of the acceptor, and the hole will remain in the HOMO level of the donor. This creates a free charge pair that generates electrical voltage in the organic photocell (Figure 1.6b).

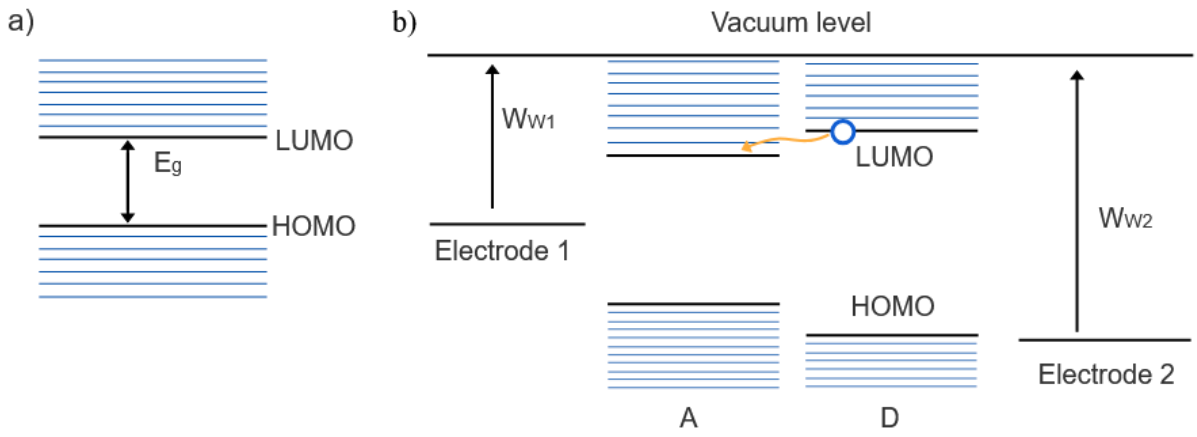

Figure 1.6. Energy model of an organic molecule (a) and an organic photovoltaic cell (b); W_{W1} - Work function of Electrode 1, W_{W2} - Work function of Electrode 2.

1.3. Structure and electrical model of a solar cell

For a photocell to function correctly, it should have a specific physical and electrical structure, and the materials forming it should be selected accordingly. When choosing the semiconductor materials that make up the photovoltaic cell, attention should be paid to the mobility of charge carriers, electron lifetime, and absorption coefficient. If we imagine a photovoltaic cell as a system of layers superimposed on each other, several characteristic layers can be distinguished in their structure, performing specific functions. A schematic diagram of the structure of a photovoltaic cell is shown in Figure 1.7, with the substrate, the bottom electrode, the hole transport layer (HTL), the semiconductor active layer, the electron transport layer (ETL), and the top electrode in sequence [12,13].

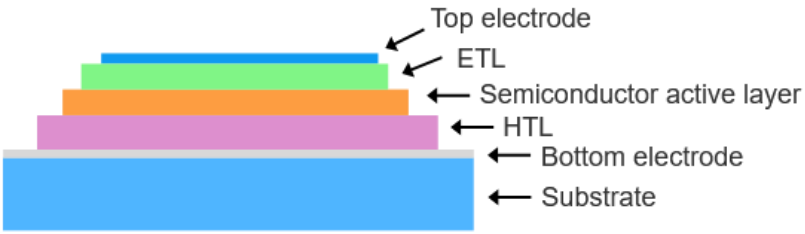

Figure 1.7. General schematic diagram of photovoltaic cell construction.

The substrate is the base of the photovoltaic cell - it can be glass or PET film. The function of the bottom electrode is to collect holes, and the function of the top electrode is to collect electrons, i.e., the carriers at the *p-n* junction. Between the electrodes of the photovoltaic cell is the active layer, or *p-n* junction, which is directly responsible for the photogeneration of electron-hole pairs. In the active layer, absorption of electromagnetic radiation, photogeneration, and exciton separation in an organic cell occur. The active layer is the most essential element of the photocell and determines its parameters, but without the coexistence with the other layers, it will not work as a photocell.

In addition to the physical structure of the photovoltaic cell, special attention should be paid to its electrical model, which is shown in Figure 1.8 [14]. It features elements such as the photovoltaic diode D, the shunt resistor R_{SH}, defining the resistance resulting from surface recombination of charge carriers, and the resistor R_S representing the sum of series resistances across the circuit. The symbols I_D, I_{SH}, I denote the corresponding currents flowing through these components. The current I is the current at the output of the circuit. In Figure 1.8, there is also a branch through which current I_L flows, representing the current generated by photogeneration.

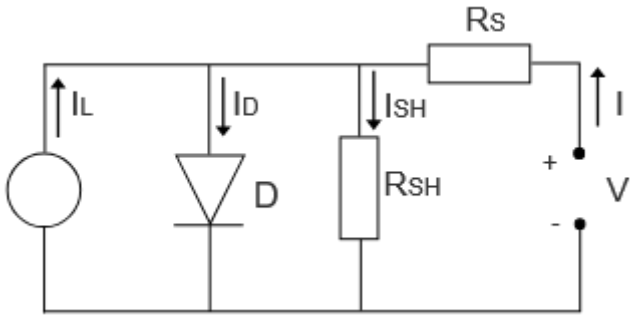

Figure 1.8. Electrical model of a photovoltaic cell; I_L - Photogeneration current, I_D - Diode current, I_{SH} - Shunt resistance current, D - Diode, R_{SH} - Shunt resistance, R_S - Series resistance.

Based on the above electrical diagram of the cell and taking into account losses, Kirchhoff's laws, and Shockley's equation (Eq. 1.1), the current I at the output of the system is expressed:

$$I = \left(I_L - \frac{V}{R_{SH}}\right)\frac{R_{SH}}{R_{SH}+R_S} - I_0\frac{R_{SH}}{R_{SH}+R_S}\left(e^{\frac{q(V-IR_S)}{nkT_K}} - 1\right) \qquad \text{(Eq. 1.2)}$$

Equation 1.2 describes the performance of the photovoltaic cell, including the effects of R_S, R_{SH}, I_L, and changes in T. The impact of R_S, R_{SH}, I_L, and T on the I-V characteristics is shown in Figure 1.9.

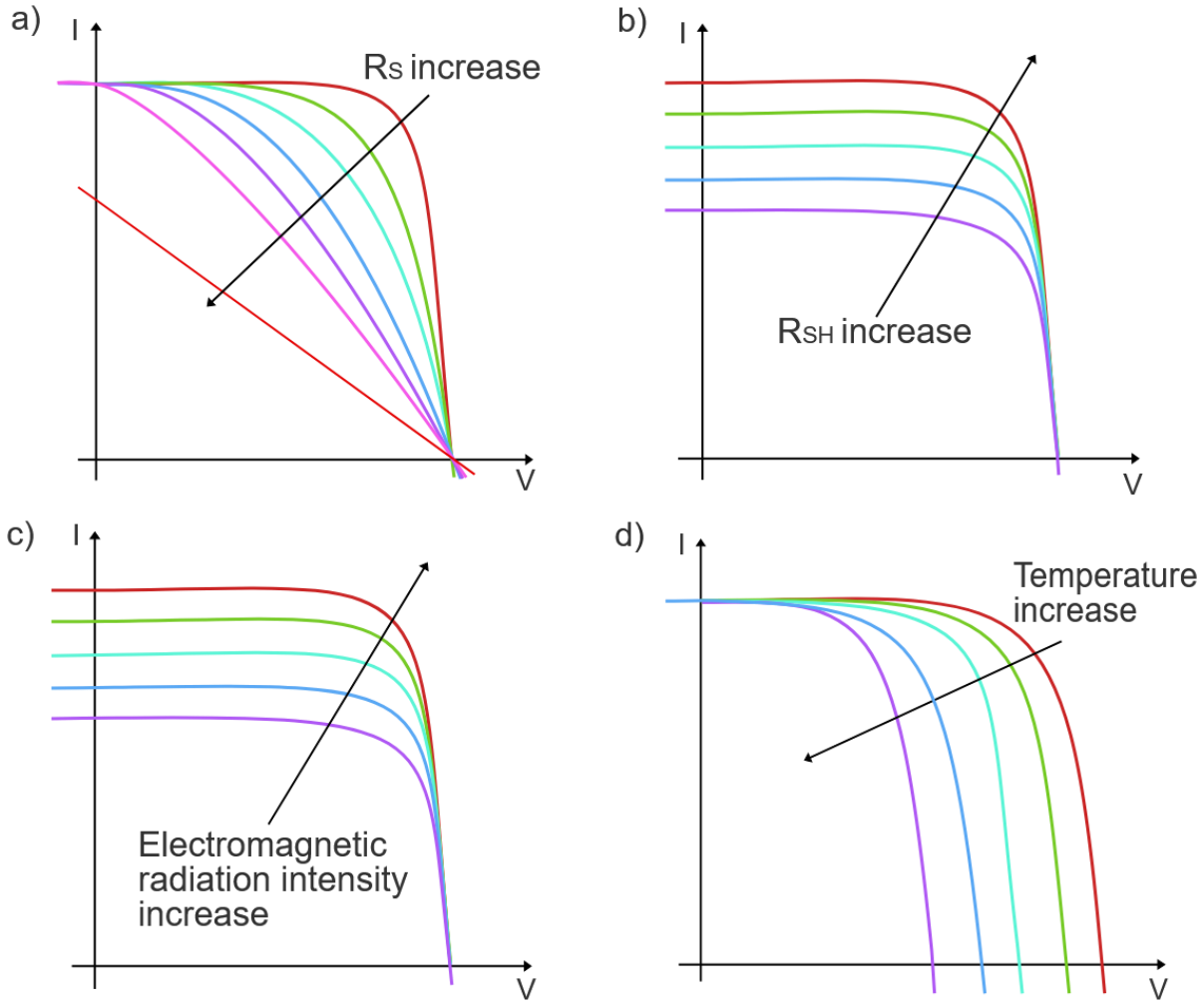

Figure 1.9. Effect of series resistance R_S (a), shunt resistance R_{SH} at constant R_S (b), electromagnetic irradiance (c), and temperature T (d) on the I-V characteristics of the photovoltaic cell.

1.4. Classification of solar cells

Photovoltaic cells can be divided into groups depending on the materials used, structure, and applied technologies. Photovoltaic cells can be split based on the materials used into inorganic, organic, and hybrid types [15-17]. Among inorganic cells, the most popular are silicon cells - monocrystalline, polycrystalline, and amorphous. The organic photovoltaic group includes cells made of organic materials, most often polymers and fullerenes. Hybrid cells are cells that combine the characteristics of inorganic and organic cells. Perovskite photovoltaic cells belong to this group.

One division of photovoltaic cells is based on the technologies used. This division illustrates the cross-section of available photovoltaic cells in a good way. There are three generations of solar cells:

- 1st generation – thick film crystalline silicon cells - have a *p-n* junction, and their efficiency is 15-27%,
- 2nd generation – thin film amorphous silicon or CdTe, CIGS cells – have a *p-n* junction, and their efficiency is 6-19%,
- 3rd generation - cells in the form of multi-junction semiconductor structures, organic cells, hybrid cells, dye sensitized cells, and perovskite cells - the efficiencies they achieve are 6-34% [18-20].

1st generation cells are the most stable cells, but also expensive. The technology to produce such cells has taken the longest to develop compared to the other two generations. 2nd generation solar cells are less efficient, but material consumption and production costs are much lower. The 3rd generation of cells includes cells based on new materials and innovative solutions. They have great potential - especially perovskite cells, whose efficiencies under laboratory conditions exceed the 30% threshold [19,21,22].

1.5. Perovskite solar cells

Perovskite cells are among the 3rd generation of solar cells. Although their technology has been in development for a relatively short time, perovskites have the potential to revolutionize the world of photovoltaics thanks to their high efficiency and low production costs. The first mention of the use of perovskites as active materials in photovoltaics came in 2009 when the research team of Miyasaka *et al.* developed a perovskite solar cell [23]. At the time, the cell achieved an efficiency of about 3.8% and operated for only a few minutes. In the following years, perovskite technology developed – different types of perovskites and other materials were tested to form the cell, and the efficiencies achieved increased yearly. Significant progress was observed between 2014 and 2020, when efficiencies increased annually by up to several percent, and photovoltaic perovskite tandem structures with flexible and transparent cells appeared [24-26]. Today, perovskite cell technology is still being developed, with efficiencies of perovskite cells reaching up to 26% under laboratory conditions, while the efficiency of perovskite tandem cells has exceeded the 30% threshold [19]. Commercialization of this type of photovoltaic cell has also begun. Particularly noteworthy is the fact that the rate of development of perovskite technology is the fastest in the history of photovoltaics, making it one of the most promising avenues for developing this field.

Perovskite cells are thin film structures in which the active layer is a compound with the crystal structure of perovskite. The thickness of a perovskite cell is approximately $1\ \mu m$. The most common perovskite is $MAPbI_3$ (methylammonium lead iodide) perovskite [27,28]. Apart from the active layer, perovskite cells are constructed according to the principles shown in Figure 1.7. Among other solar cells, they stand out for their high efficiency, low production costs, lightweight and flexible structure, and excellent light absorption. Perovskite cell technology has been under development for several years and requires further research, especially into perovskite materials, which are still poorly understood.

1.6. Solar cell testing

Standard Test Conditions (STC) were introduced to correctly compare photovoltaic cells, i.e., standardized laboratory conditions when testing photovoltaic cells [29]. These relate to irradiance, cell temperature, and the spectrum of light illuminating the cell. The STC defines the Air Mass (AM) parameter, with which the receiver's latitude on the Earth's surface is determined. Each latitude is assigned a slightly different spectrum of sunlight. The AM parameter takes values from 1 (corresponding to a position at the equator) to infinity (corresponding to a position at the poles). A special case has been defined for outer space, for which $AM = 0$. According to the STC, measurements should be carried out at a temperature of $25\,℃$ and an irradiance of $1000\,\frac{W}{m^2}$ for the quantities characterizing the cells to be comparable.

1.7. Solar cell parameters

The parameters characterizing the photovoltaic cell are determined from the I-V characteristics (Figure 1.5b). Critical is the first or fourth quadrant of this characteristic (depending on the measurement technique), from which most parameters are defined (Figure 1.10). These include:

- I_{SC} – short circuit current – the maximum current that a solar cell can generate when its terminals are short-circuited,
- J_{SC} – short circuit current density – an additional parameter used interchangeably with I_{SC} to facilitate the comparison of cells, usually expressed in $\frac{mA}{cm^2}$,
- V_{OC} – open circuit voltage – the maximum voltage that appears at the terminals of the cell when no current is flowing through it (open circuit),
- P_M – maximum power point - the operating point of the cell where the power is highest,
- FF – Fill Factor – describes the quality of the cell and is expressed by the equation:

$$FF = \frac{I_M V_M}{I_{SC} V_{OC}} \cdot 100\% \qquad \text{(Eq. 1.3)}$$

where:

- I_M, V_M – current and voltage at the maximum power point,
- η – energy efficiency, which can be calculated using the equation:

$$\eta = \frac{P_M}{P_{light}} \cdot 100\% \qquad \text{(Eq. 1.4)}$$

where:

P_{light} – the radiation power reaching the cell.

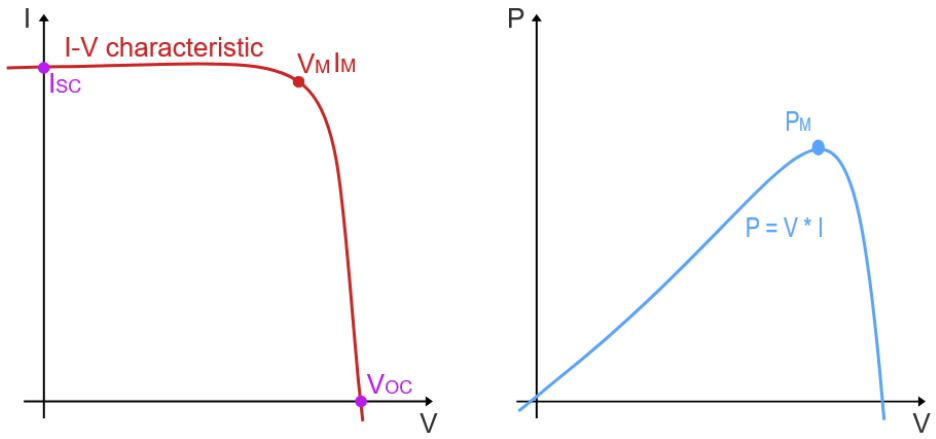

Figure 1.10. First quadrant of the I-V characteristics of an illuminated photovoltaic cell with the parameters describing the photovoltaic cell highlighted.

The above quantities are the basic ones that define photovoltaic cells [30]. In addition, it is also helpful to know the temperature power factor (which determines how the efficiency of the cell changes with temperature), the rate of efficiency decrease over time, and the Shockley-Queisser limitation, which determines the maximum theoretical energy efficiency of a photovoltaic cell composed of a single semiconductor layer, should be taken into account when designing photovoltaic cells [31].

1.8. Current advances

Renewable energy consumption is growing yearly, with global energy consumption increased by 2.2% in 2024 compared to 2023. Renewable energy sources accounted for more than 40% of global electricity production, of which solar energy exceeded the 10% threshold. The most popular solar cells have been silicon cells for years, accounting for around 90% of all photovoltaic cells. Other photovoltaic technologies account for less than 10% [32]. Perovskite cells, which are still developing, are very promising due to the high efficiencies they can achieve under laboratory conditions. Unfortunately, they are not widely used due to emerging stability and durability issues. The first commercial prototypes of perovskite photovoltaic cells have been developed, and research into them and the properties of perovskite materials continues to this day [33]. Table 1.1 summarizes the most essential information related to the different photovoltaic technologies regarding the efficiencies, flexibility, and durability achieved.

Table 1.1. Comparative table of the basic characteristics of photovoltaic cells.

PV technology	Material type	Lab efficiency [%]	Flexibility	Durability [year]
1st generation	Monocrystalline silicon	~27	Low	25-30
	Polycrystalline silicon	~23	Low	20-25
2nd generation	CdTe	~19	Medium	20-25
	CIGS	~19	High	15 <
3rd generation	Perovskite only	~26	High	< 10 (In progress)
	Tandem solar cells (Si + perovskite)	~34	Medium	(In progress)
Organic solar cells	Polymers/Small molecules	~19	High	5-10

References

1. E.K. Solak and E. Irmak, Advances in organic photovoltaic cells: a comprehensive review of materials, technologies, and performance. *RSC Adv.* (2023) 13, 12244-12269, https://doi.org/10.1039/D3RA01454A
2. H. Soonmin, A Review of Metal Oxide Thin Films in Solar Cell Applications. *IJTFST* (2022) 11, 1, PP-, available at: https://digitalcommons.aaru.edu.jo/ijtfst/vol11/iss1/5, access: April 2025
3. S. Morab *et al.* Review on Charge Carrier Transport in Inorganic and Organic Semiconductors. *Coatings* (2023) 13(9):1657, DOI: 10.3390/coatings13091657
4. C. Kittel, Introduction to Solid State Physics. *John Wiley* (1996) 7th ed.
5. L. Luh *et al.* A Zener-diode-activated ESD protection circuit for sub-micron CMOS processes. *IEEE Xplore* (2000) Conference: Circuits and Systems, Proceedings. ISCAS 2000 Geneva, The 2000 IEEE International Symposium, 5
6. C. Tablero-Crespo, Influence of the energy dependence of the absorption coefficient on the solar energy conversion efficiency. *AIP Advances* (2018) 8, 095326, https://doi.org/10.1063/1.5048984
7. F. Saeed and A. Zohaib, Quantification of Losses in a Photovoltaic System: A Review. *Engineering Proceedings* (2021) 11(1):35, DOI: 10.3390/ASEC2021-11200
8. L. Shen *et al.* Analysis of the power loss and quantification of the energy distribution in PV module. *Appl. Energy* (2020) 260, 15, 114333, DOI:10.1016/j.apenergy.2019.114333
9. M. Palewicz *et al.* Organic photovoltaic devices based on polyazomethine and fullerene. *Energy Procedia* (2011) 3, 84-91, https://doi.org/10.1016/j.egypro.2011.01.014
10. S. Yuan *et al.* Progress in research on organic photovoltaic acceptor materials. *RSC Adv.* (2025) 15, 2470-2489, DOI: 10.1039/D4RA08370A
11. C.Z. Li *et al.* Functional fullerenes for organic photovoltaics. *J. Mater. Chem.* (2012) 22(10):4161-4177, DOI: 10.1039/C2JM15126J
12. N. Guerra *et al.* Operation and physics of photovoltaic solar cells: an overview. *I+D Tecnológico* (2018) 14(2):84-95, DOI: 10.33412/idt.v14.2.2077

13. A.S. Al-Ezzi and M.N.M. Ansari, Photovoltaic Solar Cells: A Review. *Appl. Syst. Innov.* (2022) 5(4), 67, https://doi.org/10.3390/asi5040067
14. A.Pedroza-Diaz *et al.* Review of explicit models for photovoltaic cell electrical characterization. *Renew. Sust. Energ. Rev.* (2025) 207, 114979, https://doi.org/10.1016/j.rser.2024.114979
15. A.M. Oni *et al.* A comprehensive evaluation of solar cell technologies, associated loss mechanisms, and efficiency enhancement strategies for photovoltaic cells. *Energy Rep*. (2024) 11, s345-3366, https://doi.org/10.1016/j.egyr.2024.03.007
16. K. Lu, Comparison and Evaluation of Different Types of Solar Cells. *ACE* (2023) 23(1):263-270, DOI:10.54254/2755-2721/23/20230664
17. M. Dambhare *et al.* Solar photovoltaic technology: A review of different types of solar cells and its future trends. *J. Phys.: Conf. Ser.* (2021) 1913(1):012053, DOI:10.1088/1742-6596/1913/1/012053
18. X. Ru *et al.* Silicon heterojunction solar cells achieving 26.6% efficiency on commercial-size p-type silicon wafer. *Joule* (2024) 8, 4, 1092-1104, https://doi.org/10.1016/j.joule.2024.01.015
19. W. Shen *et al.* Highlights of mainstream solar cell efficiencies in 2024. *Front. Energy* (2025) 19, 8–17, https://doi.org/10.1007/s11708-025-0985-5
20. R.K. Ratnesh *et al.* Recent advances in solar cell technology: addressing technological challenges, scenarios, and environmental implications in the development of sustainable energy solutions. *New J. Chem.* (2025) 49, 6861-6887, https://doi.org/10.1039/D5NJ00719D
21. A.A. Verma *et al.* Achieving 31.16 % efficiency in perovskite solar cells via synergistic Dion-Jacobson 2D-3D layer design. *J. Alloy. Compd.* (2025) 1010, 177882, https://doi.org/10.1016/j.jallcom.2024.177882
22. M.A. Hachimi *et al.* DFT and device simulation of $KGeCl_3$ perovskite: A dual-function material for solar energy and hydrogen storage. *Int. J. Hydrogen Energy* (2025) 169, 151106, https://doi.org/10.1016/j.ijhydene.2025.151106
23. A. Kojima *et al.* Organometal Halide Perovskites as Visible-Light Sensitizers for Photovoltaic Cells. *J. Am. Chem. Soc.* (2009) 131, 17, 6050–6051, https://doi.org/10.1021/ja809598r

24. N. Lal *et al.* Perovskite Tandem Solar Cells. *Adv. Energy Mater.* (2017) 7(18):1602761, DOI:10.1002/aenm.201602761
25. H.S. Jung *et al.* Flexible Perovskite Solar Cells. *Joule* (2019) 3, 8, 1850-1880, DOI: 10.1016/j.joule.2019.07.023
26. J.W. Jung *et al.* Low-temperature processed high-performance flexible perovskite solar cells via rationally optimized solvent washing treatments. *RSC Adv.* (2014) 4, 62971-62977, https://doi.org/10.1039/C4RA13212B
27. P. Basumatary and P. Agarwal, A short review on progress in perovskite solar cells, *Mater. Res. Bull.* (2022) 149, 111700, https://doi.org/10.1016/j.materresbull.2021.111700
28. B. Dahal and W. Li, Configuration of Methylammonium Lead Iodide Perovskite Solar Cell and its Effect on the Device's Performance: A Review. *Adv. Mater. Interfaces* (2022) 9, 19, 2200042, https://doi.org/10.1002/admi.202200042
29. F. Dia *et al.* Comparison of the Methods of Calculation of Measurements Standardization on the Outdoor Photovoltaic Modules. *Am. J. Mod. Phys.* (2020) 9(3), 41-47, https://doi.org/10.11648/j.ajmp.20200903.11
30. G. Cibira, Relations among photovoltaic cell electrical parameters. *Appl. Surf. Sci.* (2018) 461, 102-107, https://doi.org/10.1016/j.apsusc.2018.05.194
31. Y. Xu *et al.* The generalized Shockley-Queisser limit for nanostructured solar cells. *Sci. Rep.* (2015) 5, 13536, https://doi.org/10.1038/srep13536
32. Global Energy Review 2025, *IEA* (2025), Licence: CC BY 4.0, https://www.iea.org/reports/global-energy-review-2025, access: April 2025
33. M.A. Hachimi *et al.* Structural, Electronic, Mechanical, and Optical Properties of X3OCl (X = Li, Na, K) Antiperovskites: An Ab-Initio Study for Energy Applications. *Physica B: Condensed Matter* (2025) S0921-4526(25)00869-5, https://doi.org/10.1016/j.physb.2025.417752

CHAPTER 2: NONLINEAR OPTICS

Nonlinear optics (NLO) is a rapidly developing optical subject that describes how light interacts with matter in a nonlinear manner. Such nonlinear interactions generate optical effects that are not proportional to the intensity of light interacting with matter. This chapter focuses attention on second- and third-order nonlinear generation and interaction mechanisms. These include the phenomena of Second and Third Harmonic Generation, nonlinear absorption, and nonlinear refractive index. The issues of symmetry and phase matching and the applicability of optical nonlinear effects in optoelectronic devices are also considered.

2.1. Wave description

Light is an electromagnetic wave whose propagation is fully described by Maxwell's equations (Eq. 2.1 - 2.4) [1,2]. Maxwell's equations are the foundation of the theory of electromagnetism. They are the starting point for describing all electromagnetic phenomena, thus also phenomena related to linear and nonlinear optics. The electric field $\overline{E}$ and magnetic induction $\overline{B}$ appearing in Maxwell's equations are the macroscopic counterparts of the microscopic fields present in a given medium.

$$\nabla \cdot \overline{D} = \rho \qquad \text{(Eq. 2.1)}$$

$$\nabla \cdot \overline{B} = 0 \qquad \text{(Eq. 2.2)}$$

$$\nabla \times \overline{E} = -\frac{\partial \overline{B}}{\partial t} \qquad \text{(Eq. 2.3)}$$

$$\nabla \times \overline{H} = \frac{\partial \overline{D}}{\partial t} + \overline{j} \qquad \text{(Eq. 2.4)}$$

$\overline{E}$ – electric field intensity vector

$\overline{H}$ – magnetic field intensity vector

$\overline{D}$ – electrical induction vector

$\overline{B}$ – magnetic induction vector

ρ – volumetric charge density

$\overline{j}$ – total current density vector

Complementing Maxwell's equations are the material equations (Eq. 2.5, Eq. 2.6), which describe how matter reacts to the electromagnetic field acting on it and depend on the material's properties. By means of the material equations, the $\overline{D}$ and $\overline{H}$ fields are related to the $\overline{E}$ and $\overline{B}$ fields.

$$\overline{D} = \varepsilon\overline{E} + \overline{P} \quad \text{(Eq. 2.5)}$$

$$\overline{B} = \mu\overline{H} + \overline{M} \quad \text{(Eq. 2.6)}$$

ε – electrical permeability of the medium

μ – magnetic permeability of the medium

The $\overline{P}$ and $\overline{M}$ vectors in the above equations denote electric and magnetic polarization, respectively. The $\overline{P}$ vector describes the macroscopic average of the dipole moments induced in the medium by the external electromagnetic field, and the $\overline{M}$ vector describes the average density of microscopic magnetic moments in the medium. Both vectors are expressed as follows:

$$\overline{P} = \varepsilon\chi_e\,\overline{E} \quad \text{(Eq. 2.7)}$$

$$\overline{M} = \chi_m\,\overline{H} \quad \text{(Eq. 2.8)}$$

where:

χ_e – electrical susceptibility,

χ_m – magnetic susceptibility.

Electrical and magnetic susceptibility are parameters specific to a medium. They determine how strongly a material reacts to an external electric field $\overline{E}$ and magnetic field $\overline{H}$, i.e., how much it can be polarized or magnetized. The solutions to Maxwell's equations are particularly interesting in a vacuum, a non-magnetic medium, with no free charge or conduction [3]. Then $\overline{M} = 0$, $\rho = 0$, $\bar{j} = 0$, $\varepsilon = \varepsilon_0 = 8.85 \cdot 10^{-12} \frac{C^2}{Nm^2}$, $\mu = \mu_0 = 1.26 \cdot 10^{-6} \frac{N}{A^2}$ and:

$$\overline{B} = \mu_0 \overline{H} \qquad \text{(Eq. 2.9)}$$

In considering Maxwell's equations for a vacuum, the electrical polarization $\overline{P}$ cannot be neglected, which in strong electric fields includes, in addition to the linear response $\overline{P}_L$, the nonlinear response $\overline{P}_{NL}$. This means that the total polarization vector $\overline{P}$ can be written as the sum of a linear and a nonlinear term:

$$\overline{P} = \overline{P}_L + \overline{P}_{NL} \qquad \text{(Eq. 2.10)}$$

By substituting Eq. 2.7 to Eq. 2.10 the electrical polarization $\overline{P}$ is written as a power series:

$$\overline{P} = \varepsilon_0 \left[\chi_e^{(1)} \overline{E} + \chi_e^{(2)} \overline{E}^2 + \chi_e^{(3)} \overline{E}^3 + \cdots + \chi_e^{(n)} \overline{E}^n \right] \qquad \text{(Eq. 2.11)}$$

The first term of Eq. 2.11 describes the linear dependence of the electric polarization $\overline{P}$ on the electric field $\overline{E}$ (Eq. 2.12), and the other members of this equation are related to the nonlinear dependence (Eq. 2.13).

$$\overline{P}_L = \varepsilon_0 \chi_e^{(1)} \overline{E} \quad \text{(Eq. 2.12)}$$

$$\overline{P}_{NL} = \varepsilon_0 \left[\chi_e^{(2)} \overline{E}^2 + \chi_e^{(3)} \overline{E}^3 + \cdots + \chi_e^{(n)} \overline{E}^n \right] \quad \text{(Eq. 2.13)}$$

$\chi_e^{(1)}$ – linear electrical susceptibility

$\chi_e^{(2)}$, $\chi_e^{(3)}$, …, $\chi_e^{(n)}$ – nonlinear electrical susceptibility, successively second-order nonlinear electrical susceptibility, third-order nonlinear electrical susceptibility, ..., nth - order nonlinear electrical susceptibility

The electrical susceptibility χ_e takes on different dimensions depending on its order of magnitude. The magnitude of $\chi_e^{(1)}$ is dimensionless and its order of magnitude is about 1, while the dimension of $\chi_e^{(2)}$ is $\frac{m}{V}$ and $\chi_e^{(3)}$ has a dimension of $\frac{m^2}{V^2}$. Finally, the electrical polarization of the medium based on the above considerations can be written as the sum of linear and nonlinear polarization:

$$\overline{P} = \overline{P}^{(1)} + \overline{P}^{(2)} + \overline{P}^{(3)} + \ldots + \overline{P}^{(n)} \quad \text{(Eq. 2.14)}$$

where:

$\overline{P}^{(n)}$ – electrical polarization of the nth order, n = 1, 2, 3, ...

Furthermore, at the molecular level, Eq. 2.13 can be expressed by the sum of the local electric fields acting on each molecule of the medium (Eq. 2.15).

$$\overline{P} = N\left(\alpha \overline{E}_{loc} + \beta \overline{E}_{loc}^2 + \gamma \overline{E}_{loc}^3 + \ldots\right) \quad \text{(Eq. 2.15)}$$

N – volume density of particles

α – linear polarizability tensor

β – quadratic hyperpolarizability tensor

γ – cubic hyperpolarizability tensor

Having already known what the polarization $\overline{P}$ is in the material equations, one can return to Maxwell's equations and consider the rotation of the electric field vector $\overline{E}$ with Eq. 2.3. Because of the continuity of the function, one can reorder the derivatives with respect to time and space on the right-hand side of the resulting equation. Using Eq. 2.4, Eq. 2.9 and $\bar{j} = 0$ one obtains Eq. 2.16:

$$\nabla \times \nabla \times \overline{E} + \mu_0 \frac{\partial^2}{\partial t^2} \overline{D} = 0 \qquad \text{(Eq. 2.16)}$$

which can be simplified by using a relationship:

$$\nabla \times \nabla \times \overline{E} = \nabla\left(\nabla \cdot \overline{E}\right) - \nabla^2 \overline{E} \qquad \text{(Eq. 2.17)}$$

With respect to nonlinear optics, it cannot be assumed that $\nabla \cdot \overline{E} = 0$ based on $\nabla \cdot \overline{D} = 0$, but it can be assumed that $\nabla\left(\nabla \cdot \overline{E}\right)$ is negligible in Eq. 2.17. Consequently, Eq. 2.16 can be written in the form:

$$\nabla^2 \overline{E} - \mu_0 \frac{\partial^2}{\partial t^2} \overline{D} = 0 \qquad \text{(Eq. 2.18)}$$

The vector $\overline{D}$ can be replaced according to Eq. 2.5, and μ_0 can be written as $\frac{1}{\varepsilon_0 c^2}$, where c is the speed of light in vacuum. These substitutions yield the most general wave equation in nonlinear optics [4]:

$$\nabla^2 \overline{E} - \frac{1}{c^2} \frac{\partial^2}{\partial t^2} \overline{E} = \frac{1}{\varepsilon_0 c^2} \frac{\partial^2}{\partial t^2} \overline{P} \qquad \text{(Eq. 2.19)}$$

Equation 2.19 is an extension of the standard wave equation in optics. It considers the nonlinear response of the medium to the electric field, leading to new components in the equation responsible for nonlinear effects. The wave equation for nonlinear optics describes how the electric field can generate new wave components in a nonlinear medium, such as the second and third harmonics, in response to a strong electric field. Removing the right-hand side of the equation gives the Helmholtz equation, which predicts the existence of electromagnetic waves in a vacuum [3].

2.2. Interaction of light with matter

The interaction of light, i.e., an electromagnetic wave, with matter, is one of the fundamental issues in optics. It involves many mechanisms and depends on the type of medium in which the wave propagates and the characteristics of the incident wave. Maxwell's equations greatly help in describing the interaction of light with matter. They show us how the electromagnetic field propagates in space and interacts with materials. When considering this interaction, the weak and strong electromagnetic fields with matter must be considered, as this makes a huge difference from an optical point of view.

The electromagnetic field of an electromagnetic wave with frequency ω and amplitude E passing through a transparent medium interacts with the positively charged atoms and molecules that compose it and with the negatively charged electrons. Thus, the field exerts forces on the atoms' weakly bound outer or valence electrons. As a result of the electric field, the electrons begin to vibrate and move, forming small electric dipoles. The positive charges forming the medium move towards the external electric field, and the negative charges move in the opposite direction. All this leads to the electrical polarization of the medium, i.e., the ordering of the vibrating electric dipoles and the formation of induced dipole moments μ. The effect of the magnetic field of an electromagnetic wave acting on the medium in this context is negligible. Each vibrating dipole of the medium emits a microscopic electromagnetic field, which takes on features from the external electric field interacting with the medium. If the external field is harmonic, at a given frequency, the electric dipoles will emit an electromagnetic field with the same characteristics. The situation described in this paragraph is schematically illustrated in Figure 2.1.

When the forces induced by the external electromagnetic field acting on the electrons are small compared to the internal forces generated by the interaction of charges in the medium, in a linear isotropic medium, the resulting electric polarization P is parallel and directly proportional to the applied electric field E. This means that the intensity of the radiation emitted by the vibrating electric dipoles is directly proportional to the intensity of the external excitation radiation. This approach is described by traditional optics, so-called linear optics, where the behaviour of a material can be described by constants such as the refractive index or absorption coefficient.

In nonlinear optics, the opposite behaviour is observed - the response of the medium to the external electromagnetic field is nonlinear. Such mechanisms are observed when the external electromagnetic field interacting with the medium is strong. Such strong electromagnetic fields are generated using laser beams. The nonlinear response of the system means that the displacement of electrons in the medium is not proportional to the incident electric field $\overline{E}$ - new radiation frequencies and optical effects classified as nonlinear phenomena are generated. Among these are the generation of higher harmonics and wave mixing.

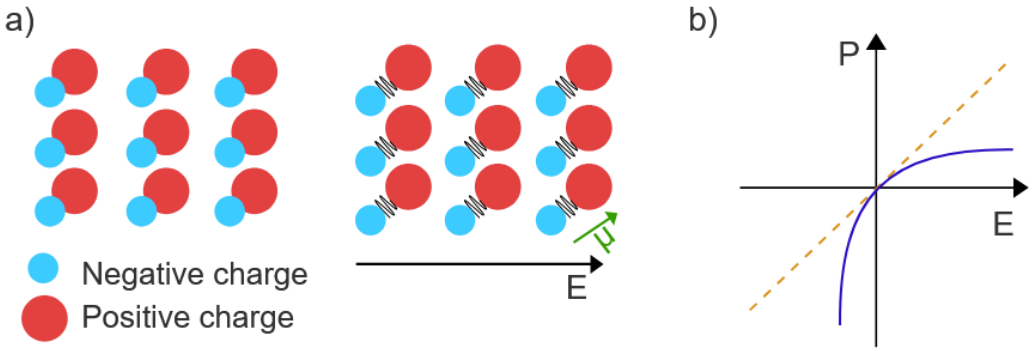

Figure 2.1. The response of a dielectric medium to an external electromagnetic field: polarization of the medium and induction of dipole moments (a), as well as linear and nonlinear dependence of the polarization P on the applied electric field E (b).

The nonlinear optics branch emerged in 1961, when Franken's research team discovered the second harmonic generation [5]. In their experiment, using a quartz crystal and a 694.3 nm pulsed ruby laser, a 347.2 nm wavelength corresponding to the second harmonic was generated.

With reference to perovskite materials, the study of nonlinear effects has mainly been ongoing for the last 10 years. In the previous decade, two-photon absorption effects have been discovered in nanowire lasers made of perovskite, but the generation of second and third harmonics (SHG, THG) and reverse saturable absorption (RSA) in perovskite 2D structures have also been demonstrated [6-8]. Perovskites are interesting materials in the context of nonlinear optics due to physical properties such as high nonlinear dielectric susceptibility coefficient, strong absorption and emission in the UV-VIS-NIR range, low effective mass of carriers, and strong exciton coupling. Due to these properties, perovskites have been extensively studied in the field of nonlinear optics, and it is still a rapidly developing topic.

2.3. Second Harmonic Generation

Second Harmonic Generation (SHG) is one of the most important phenomena in second-order nonlinear optics. In the simplest explanation of this phenomenon, it is said that two photons with the same frequency ω, amplitude E, and the same propagation direction interact in a nonlinear medium and combine to form a single photon with a doubled frequency 2ω. The frequency doubling is simultaneously associated with a doubling of energy and a shortening of the electromagnetic wavelength incident on the medium from outside. The SHG phenomenon is shown in a simplified manner in Figure 2.2. Second-order optical nonlinear phenomena, in addition to SHG, include other phenomena such as Sum-Frequency Generation (SFG), Difference-Frequency Generation (DFG), Pockels Effect, and parametric amplification.

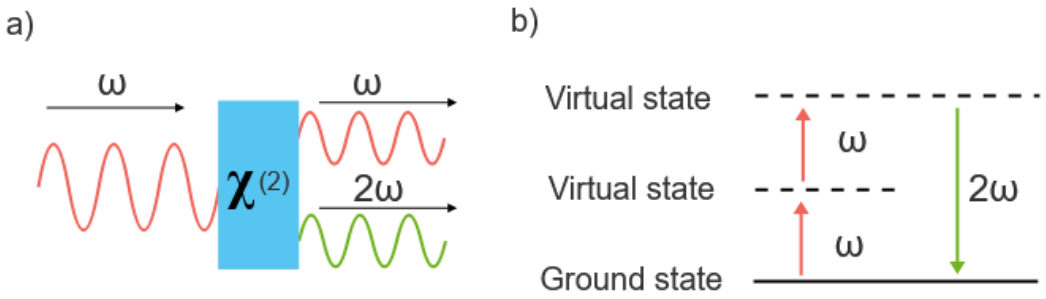

Figure 2.2. Generation of the second harmonic by a nonlinear medium (a) and the energy model of this phenomenon (b).

For second-order nonlinear optical effects to take place in a given medium, certain requirements related to the crystal structure must be fulfilled - specifically, the medium must lack inversion symmetry [9,10]. This means that the crystal structure of the medium changes when all spatial coordinates are inverted with respect to the centre of symmetry. Such materials are said to be non-centrosymmetric. Based on Eq. 2.12, the second-order nonlinear polarization for a material without inversion symmetry can be written as:

$$-\overline{P}^{(2)} = \varepsilon_0 \chi_e^{(2)} \left(-\overline{E}\right)^2 \qquad -\overline{P}^{(2)} = \varepsilon_0 \chi_e^{(2)} \overline{E}^2 \qquad \text{(Eq. 2.20)}$$

It follows that:

$$\overline{P}^{(2)} = -\overline{P}^{(2)} \qquad \text{(Eq. 2.21)}$$

Equation 2.21 can only be true when $\chi_e^{(2)} = 0$. This means that second-order optical nonlinear effects occur only in materials devoid of inversion symmetry.

The performance of the SHG process depends primarily on the properties of the nonlinear medium, but also on phase matching and optimization of the output signal intensity. As highlighted earlier, nonlinear optical effects can be generated by the interaction of matter with a strong electromagnetic field. Such a strong electromagnetic field is generated by a laser beam. The electric field of a laser beam propagating in the direction of vector $\overline{k}$ depends on time t, spatial coordinate r, and can be described by Eq. 2.22 [1,2].

$$\overline{E}(r, t) = E \cdot \cos\left(\omega t - \overline{k} \cdot r\right) \qquad \text{(Eq. 2.22)}$$

For second-order nonlinear effects, $\chi_e^{(2)}$ differs from zero, and $\overline{P}^{(2)}$ describes Eq. 2.23.

$$\overline{P}^{(2)}(r, t) = \varepsilon_0 \chi_e^{(2)} \cdot \overline{E}^2 \qquad \text{(Eq. 2.23)}$$

Considering Eq. 2.22 in the above equation, we obtain Eq. 2.24, which describes the second-order polarization. It consists of a time-independent, time-dependent, and a frequency-varying part 2ω . Clearly, from here, it can be seen that the first term describes the static field and the second term describes the new wave created with a doubled frequency with respect to the original wave.

$$\overline{P}^{(2)}(r,\,t) \;=\; \frac{1}{2}\varepsilon_0\,\chi_e^{(2)}\,E^2\left[1+\cos 2\left(\omega t\;-\;\overline{k}\cdot r\right)\right] \qquad \text{(Eq. 2.24)}$$

The intensity of a frequency-doubled electromagnetic wave generated in a nonlinear medium of thickness d is described by the equation:

$$I(2\omega,d)\;\approx\;I_\omega^2\left(\chi_e^{(2)}\right)^2\left[\frac{\sin\left(\frac{1}{2}d\Delta k\right)}{\frac{1}{2}d\Delta k}\right]^2 \qquad \text{(Eq. 2.25)}$$

where:

I_ω – the intensity of the electromagnetic wave incident on the medium,

Δk – phase matching.

$$|\Delta k|\;=\;\left|\overline{k}_2\;-\;2\overline{k}_1\right|\;=\;\frac{2\omega}{c}(n_{2\omega}\;-\;n_\omega) \qquad \text{(Eq. 2.26)}$$

$\overline{k}_1$ – wave vector corresponding to the fundamental wavelength

$\overline{k}_2$ – wave vector corresponding to the second harmonic generated

The phase matching condition is very important for performing nonlinear optical processes. In a nonlinear medium, the fundamental and the generated harmonic waves propagate. For the energy conversion from ω to 2ω to be as efficient as possible, the waves must oscillate in phase [11,12]. Such oscillations occur when the phase matching condition is met:

$$\Delta k = 0 \qquad \text{(Eq. 2.27)}$$

which can be written as:

$$n_{2\omega} = n_{\omega} \qquad \text{(Eq. 2.28)}$$

where:

n_{ω}, $n_{2\omega}$ – refractive indices for the fundamental and second harmonic waves.

If the phase matching condition Eq. 2.27 is not met, the waves in the medium will not be in phase, and a periodic variation of the SHG intensity as a function of the thickness d of the medium will be observed. The so-called coherence length L_C is used in such a situation. This parameter describes the maximum distance the second harmonic wave can interfere with the fundamental wave before phase coherence is lost [13]. The coherence length L_C defines the distance at which the phase difference between the two waves is π. It can be expressed using Eq. 2.29 and Eq. 2.30.

$$L_C = \frac{\pi}{|\Delta k|} \qquad \text{(Eq. 2.29)}$$

$$L_C = \frac{\lambda}{4(n_{2\omega} - n_{\omega})} \qquad \text{(Eq. 2.30)}$$

Phase matching in the SHG process is crucial - the better the wave phases are matched, the greater the coherence length and the efficiency of the process. The SHG signal intensity is also influenced by the surface morphology of the medium and by the optical system used for the measurements, which should be precisely designed.

2.4. Second-order nonlinear susceptibility

Second-order nonlinear susceptibility $\chi^{(2)}$ is a very important parameter in nonlinear optics. This parameter describes the response of a material to a strong electromagnetic field. In other words, it determines how much the medium responds by generating new electromagnetic waves at frequencies other than the fundamental wave. The parameter $\chi^{(2)}$ can therefore be seen as an indicator of the performance of a second-order nonlinear process - the larger it is, the stronger the SHG signal. The nonlinear susceptibility is a third-order tensor, consisting of 27 components, which relates the electric field of the electromagnetic wave to the second-order polarization generated. It is represented as a matrix of coefficients $\chi_{ijk}^{(2)}$ along the axes of the x , y , z coordinate system. If a plane electromagnetic wave with circular frequency ω propagates in the z -axis direction, then it can be written in the form:

$$E(z,\, t) \,=\, E(z)\, e^{-i\omega t} \,+\, c.c. \qquad \text{(Eq. 2.31)}$$

where:

$c.c.$ - complex conjugation.

By substituting the above wave equation into Eq. 2.23, describing second-order nonlinear polarization, one obtains the expression:

$$P^{(2)}\,(t) \,=\, 2\varepsilon_0\, \chi_e^{(2)} \,\cdot\, EE^* \,+\, \varepsilon_0\, \chi_e^{(2)} \left[E^2\, e^{-2i\omega t} \,+\, c.c.\right] \qquad \text{(Eq. 2.32)}$$

In the above equation, the component containing 2ω is responsible for the formation of the SHG signal and thus for the phenomenon of the second-order nonlinear susceptibility $\chi_e^{(2)}$. The $\chi_e^{(2)}$ tensor consists of 27 elements. In contrast, given that the elements of the $\chi_{ijk}^{(2)}$ tensor are invariant to changes in the indices j and k, one can reduce the number of independent components to 18 and write the polarization as follows:

$$\begin{bmatrix} P_x^{NL} \\ P_y^{NL} \\ P_z^{NL} \end{bmatrix} = \varepsilon_0 \begin{bmatrix} \chi_{111} & \chi_{122} & \chi_{133} & \chi_{123} & \chi_{113} & \chi_{112} \\ \chi_{211} & \chi_{222} & \chi_{233} & \chi_{223} & \chi_{213} & \chi_{212} \\ \chi_{311} & \chi_{322} & \chi_{333} & \chi_{323} & \chi_{313} & \chi_{312} \end{bmatrix} \begin{bmatrix} E_x^2(\omega) \\ E_y^2(\omega) \\ E_z^2(\omega) \\ 2E_y(\omega)E_z(\omega) \\ 2E_x(\omega)E_z(\omega) \\ 2E_x(\omega)E_y(\omega) \end{bmatrix} \quad \text{(Eq. 2.33)}$$

In 1962, Kleinman showed that the tensor $\chi^{(2)}$ is symmetric with respect to the permutation of the three indices ijk [14,15]:

$$\chi_{ijk} = \chi_{ikj} = \chi_{jik} = \chi_{jki} = \chi_{kij} = \chi_{kji} \quad \text{(Eq. 2.34)}$$

Due to this symmetry, 10 independent elements remain in the tensor $\chi_{ijk}^{(2)}$.

$$\begin{bmatrix} P_x^{NL} \\ P_y^{NL} \\ P_z^{NL} \end{bmatrix} = \varepsilon_0 \begin{bmatrix} \chi_{111} & \chi_{122} & \chi_{133} & \chi_{123} & \chi_{113} & \chi_{112} \\ \chi_{112} & \chi_{222} & \chi_{233} & \chi_{223} & \chi_{123} & \chi_{122} \\ \chi_{113} & \chi_{223} & \chi_{333} & \chi_{233} & \chi_{133} & \chi_{123} \end{bmatrix} \begin{bmatrix} E_x^2(\omega) \\ E_y^2(\omega) \\ E_z^2(\omega) \\ 2E_y(\omega)E_z(\omega) \\ 2E_x(\omega)E_z(\omega) \\ 2E_x(\omega)E_y(\omega) \end{bmatrix} \quad \text{(Eq. 2.35)}$$

Very often the components of the $\chi_{ijk}^{(2)}$ tensor are denoted by the d_{il} tensor, which are related to each other by a relation:

$$2d_{il} = \chi_{ijk} \quad \text{(Eq. 2.36)}$$

where:

$$[\,jk\,] = \begin{bmatrix} 11 & 12 & 13 \\ 21 & 22 & 23 \\ 31 & 32 & 33 \end{bmatrix} = [\,l\,] = \begin{bmatrix} 1 & 6 & 5 \\ 6 & 2 & 4 \\ 5 & 4 & 3 \end{bmatrix} \quad \text{(Eq. 2.37)}$$

Based on the above considerations, the second-order nonlinear susceptibility tensor $\chi_{ijk}^{(2)}$ can be presented in a new form:

$$\begin{bmatrix} P_x^{NL} \\ P_y^{NL} \\ P_z^{NL} \end{bmatrix} = 2\varepsilon_0 \begin{bmatrix} d_{11} & d_{12} & d_{13} & d_{14} & d_{15} & d_{16} \\ d_{16} & d_{22} & d_{23} & d_{24} & d_{14} & d_{12} \\ d_{15} & d_{24} & d_{33} & d_{23} & d_{13} & d_{14} \end{bmatrix} \begin{bmatrix} E_x^2(\omega) \\ E_y^2(\omega) \\ E_z^2(\omega) \\ 2E_y(\omega)E_z(\omega) \\ 2E_x(\omega)E_z(\omega) \\ 2E_x(\omega)E_y(\omega) \end{bmatrix} \quad \text{(Eq. 2.38)}$$

2.5. Third Harmonic Generation

Third Harmonic Generation (THG) is one of the fundamental phenomena of third-order nonlinear optics. The mechanism of the phenomenon is similar to that of SHG. In the simplest explanation of the phenomenon, it is said that three photons of the same frequency ω interact in a nonlinear medium and combine to form one photon of tripled frequency 3ω. This change in frequency is simultaneously associated with a tripling of energy and the generation of a new wave with a wavelength three times shorter than the electromagnetic fundamental wave. The THG phenomenon is shown in a simplified manner in Figure 2.3. In contrast to SHG, during the THG process, the molecules of the medium are temporarily excited to so-called virtual energy levels. These levels are unstable states. As a result, the molecule quickly emits a photon without absorbing energy. Among third-order optical nonlinear phenomena, in addition to THG, the Kerr effect, two-photon absorption (TPA), phase self-modulation (SPM), and four-wave mixing (FWM) are prominent.

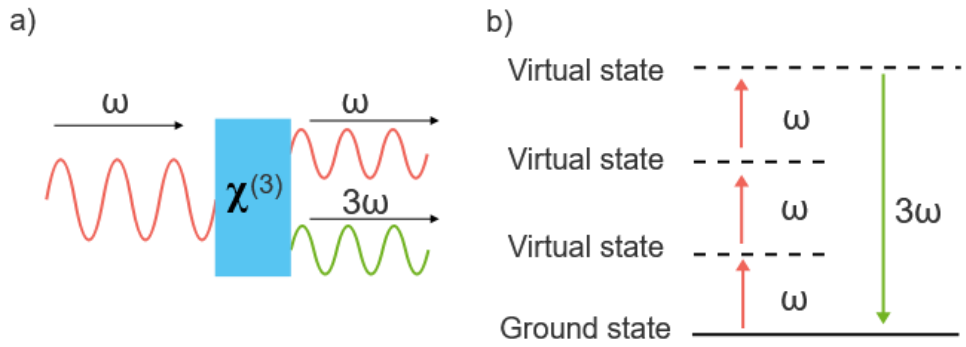

Figure 2.3. Generation of the third harmonic by a nonlinear medium (a) and the energy model of this phenomenon (b).

Like SHG, the generation of third-order nonlinear effects is related to the third-order nonlinear polarization of the medium:

$$\overline{P}^{(3)}(r,\,t) \;=\; \varepsilon_0\,\chi_e^{(3)}\cdot\overline{E}^3 \qquad \text{(Eq. 2.39)}$$

By substituting into the above equation Eq. 2.22 describing the electric field of the laser beam, the third-order nonlinear polarization takes the form:

$$\begin{aligned}\overline{P}^{(3)}(r,\,t) \;=\; & \frac{1}{4}\varepsilon_0\,\chi_e^{(3)}\,E^3\,\cos 3\left(\omega t-\overline{k}\cdot r\right)\\ & +\;\frac{3}{4}\varepsilon_0\,\chi_e^{(3)}\,E^3\,\cos\left(\omega t-\overline{k}\cdot r\right)\end{aligned} \qquad \text{(Eq. 2.40)}$$

The first element of Eq. 1.40 describes the third-order nonlinear response of the medium, as evidenced by the occurrence of a 3ω frequency triplet.

Analogous to SHG, the intensity of the generated third harmonic signal in a medium of thickness d is expressed by the formula:

$$I(3\omega,\,d) \;\approx\; I_\omega^3\left(\chi_e^{(3)}\right)^2\left[\frac{\sin\left(\frac{1}{2}d\Delta k\right)}{\frac{1}{2}d\Delta k}\right]^2 \qquad \text{(Eq. 2.41)}$$

where:

Δk – phase matching.

The efficiency of the THG process depends on the phase matching conditions. For the energy conversion to be as efficient as possible, the fundamental wave and the generated third harmonic wave should remain in a well-defined phase relationship when propagating in a nonlinear medium. The phase matching condition in this case is as follows:

$$|\Delta k| = \left|\overline{k}_3 - 3\overline{k}_1\right| = \frac{3\omega}{c}\left(n_{3\omega} - n_{\omega}\right) \qquad \text{(Eq. 2.42)}$$

where:

$\overline{k}_1$ - the wave vector corresponding to the fundamental wavelength,

$\overline{k}_3$ - the wave vector corresponding to the generated third harmonic,

n_{ω}, $n_{3\omega}$ – refractive indices for the fundamental and third harmonic wave.

Phase matching plays just as important a role in the THG process as in SHG. A significant difference between these processes is that there are no structural requirements for the THG process - Third Harmonic Generation is obtained in non-centrosymmetric and centrosymmetric materials.

2.6. Third-order nonlinear susceptibility

The third-order nonlinear susceptibility $\chi^{(3)}$ is an important parameter in nonlinear optics. It describes the response of a material to a strong electromagnetic field, which is proportional to the third power of the field. The parameter $\chi^{(3)}$, like the parameter $\chi^{(2)}$, can be regarded as an indicator of the performance of a third-order nonlinear process. The third-order nonlinear susceptibility $\chi^{(3)}$ is a fourth-order tensor with 81 elements. It can consist of components that respond to different directions of interactions in space and can contain real and imaginary elements. Considering the situation where three monochromatic plane waves,

each with its frequency ω, propagate in a nonlinear medium, their electric field can be expressed by the formula:

$$\overline{E}(t) = \overline{E}_1 e^{-i\omega_1 t} + \overline{E}_2 e^{-i\omega_2 t} + \overline{E}_3 e^{-i\omega_3 t} + c.c. \quad \text{(Eq. 2.43)}$$

where:

$c.c.$ - complex conjugation.

In the case under consideration, the third-order nonlinear polarization is expressed as follows:

$$P^{(3)} = \varepsilon_0 \chi^{(3)}_{ijkl} E_j E_k E_l \quad \text{(Eq. 2.44)}$$

The third-order nonlinear susceptibility tensor $\chi^{(3)}_{ijkl}$, like the second-order nonlinear susceptibility tensor $\chi^{(2)}_{ijk}$, is simplified according to the crystal structure of the material [16,17]. This reduces the number of tensor elements to non-zero and independent values. For isotropic media, the following symmetry features can be written down:

$$\chi^{(3)}_{xxxx} = \chi^{(3)}_{yyyy} = \chi^{(3)}_{zzzz} = \chi^{(3)}_{xxyy} + \chi^{(3)}_{xyxy} + \chi^{(3)}_{xyyx}$$

$$\chi^{(3)}_{yyzz} = \chi^{(3)}_{zzyy} = \chi^{(3)}_{zzxx} = \chi^{(3)}_{xxzz} = \chi^{(3)}_{xxyy} = \chi^{(3)}_{yyxx} \quad \text{(Eq. 2.45)}$$

$$\chi^{(3)}_{yzyz} = \chi^{(3)}_{zyzy} = \chi^{(3)}_{zxzx} = \chi^{(3)}_{xzxz} = \chi^{(3)}_{xyxy} = \chi^{(3)}_{yxyx}$$

From the above, it can be seen that the tensor $\chi^{(3)}_{ijkl}$ consists of three independent elements: $\chi^{(3)}_{xxxx}$, $\chi^{(3)}_{xxyy}$, and $\chi^{(3)}_{xyxy}$.

The elements of the third-order nonlinear optical susceptibility tensor $\chi^{(3)}$ are complex:

$$\chi^{(3)} = \chi'^{(3)} + \chi''^{(3)} \quad \text{(Eq. 2.46)}$$

where:

$\chi'^{(3)}$ – real part,

$\chi''^{(3)}$ – imaginary part.

The real part of the tensor is responsible for nonlinear changes in the refractive index. In contrast, the complex part is related to the phenomenon of nonlinear light absorption and stimulated scattering [18].

2.7. Nonlinear absorption

Spectroscopic measurements of materials are used to characterize them. The simplest such measurements involve measuring the absorption spectra (absorbance A) or transmission spectra (transmittance T) of a given material. The measurement results provide information on the amount of energy the sample absorbs from the radiation passing through it.

Mathematically, absorbance A and transmittance T are expressed by the formulas:

$$T = \frac{I}{I_0} \quad \text{(Eq. 2.47)}$$

$$A = \log \frac{1}{T} = \log \frac{I_0}{I} \quad \text{(Eq. 2.48)}$$

where:

I – the intensity of radiation passing through the sample,

I_0 – intensity of radiation incident on the sample.

Transmittance takes values from 0 to 1, where 0 means the radiation has been completely absorbed by the medium and 1 means that the radiation has completely passed through the medium. In the case of absorbance, when the radiation has completely passed through the medium, then $A = 0$, and when it is completely absorbed, the absorbance value tends to infinity. Transmittance and absorbance are usually given in percentages. The intensity of radiation I of a beam that passes through an absorbing medium decreases exponentially with the medium's thickness d, which can be described by Eq. 2.49.

$$I = I_0 \, e^{-k_\alpha \, d} \qquad \text{(Eq. 2.49)}$$

I – the intensity of radiation of the beam passing through the medium

I_0 – intensity of radiation incident on the sample

k_α – attenuation coefficient

d – the thickness of the medium through which the radiation beam passes

Inserting Eq. 2.49 into Eq. 2.48 we get the relationship:

$$A = 0.4343 \cdot k_\alpha \, d \qquad \text{(Eq. 2.50)}$$

Assuming no scattering exists in the medium, the attenuation coefficient k_α can be replaced by the linear absorption coefficient α_0. In that case, the above equation can be written in the form:

$$A = 0.4343 \cdot \alpha_0 \, d \qquad \text{(Eq. 2.51)}$$

where:

α_0 – linear absorption coefficient of radiation with dimensions $\frac{1}{cm}$.

Equation 2.51 is called the Lambert–Beer law, and the absorption coefficient α_0 is a characteristic parameter for each medium.

When a medium is exposed to very intense electromagnetic radiation, the medium can absorb more than one photon. In such a situation, we speak of multiphoton absorption, and hence we distinguish between single-photon, two-photon, three-photon absorption, and so on. In the presented work, two-photon absorption (TPA) is the most important, and it is given more attention below.

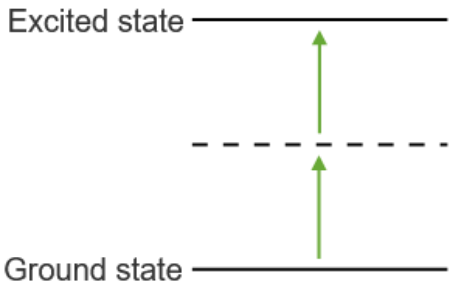

Figure 2.4. TPA process.

TPA is a third-order nonlinear absorption optical process whose characteristic quantity is the nonlinear absorption coefficient β :

$$\alpha = \alpha_0 + \beta I \qquad \text{(Eq. 2.52)}$$

α_0 – linear absorption coefficient.

As mentioned in *Section 2.6*, the imaginary part of the third-order nonlinear susceptibility tensor is related to the nonlinear absorption of radiation. The formula that expresses this relationship is:

$$\chi''^{(3)} = \frac{n_0^2\, \varepsilon_0\, c\lambda}{3\pi} \beta \left[\frac{m}{W}\right] \qquad \text{(Eq. 2.53)}$$

where:

n_0 – linear refractive index,

c – speed of light,

λ – wavelength of radiation.

Nonlinear absorption can occur in two varieties – as saturating absorption (SA) and reverse saturating absorption (RSA) [19]. In a situation where SA occurs, a decrease in absorption is observed with an increase in the intensity of radiation incident on the medium. This results from the intensive excitation process, which means the carriers do not have enough time to return to the ground state. In this way, the ability of the medium to absorb radiation is limited. In the case of RSA, absorption increases with an increase in radiation intensity. The higher the radiation intensity, the more particles pass into the excited state. Such absorption occurs in media with a long lifetime of excited states.

2.8. Nonlinear refractive index

The nonlinear refractive index n_2 is a quantity that describes how the refractive index of a medium changes depending on the intensity of the electromagnetic radiation incident on it. In linear optics, the refractive index is constant and does not depend on radiation intensity. In nonlinear optics, when the medium is exposed to radiation of very high intensity, the nonlinear refractive index n_2 depends on the intensity of the electromagnetic wave I :

$$n = n_0 + n_2 I \qquad \text{(Eq. 2.54)}$$

where:

n_0 – linear refractive index,

n_2 – nonlinear refractive index,

I – intensity of electromagnetic wave.

The dimension of n_2 is $\frac{m^2}{W}$. If n_2 is positive, the self-focusing phenomenon is observed. In the opposite case, when n_2 is negative, the self-defocusing phenomenon occurs. The nonlinear refractive index is related to the real part of the third-order nonlinear susceptibility as follows:

$$\chi'^{(3)} = \frac{4n_0^2\,\varepsilon_0\,c}{3}n_2 \qquad \text{(Eq. 2.55)}$$

2.9. Applications

Nonlinear optics is a field of science with a wide range of applications. It has a great impact on modern technology and science. It finds application in advanced photonics, medicine, telecommunications, and new quantum technologies [20,21].

One of the basic goals of nonlinear optics is frequency conversion, i.e., generating new electromagnetic wavelengths. Frequency conversion allows light with colors that are not directly available from lasers. An example of an application is, for example, a green pointer from an infrared laser [22]. In such a device, a solid-state laser with a wavelength of 1064 nm is used. Thanks to the generation of the second harmonic on the nonlinear crystal, the fundamental frequency of the laser beam is converted, and a beam with a wavelength of 532 nm is generated, corresponding to green light. By using appropriate filters at the output of the system, pure green light is obtained. The most popular nonlinear crystals used for frequency conversion are BBO, KTP, LBO crystals, and perovskites [23-25]. Frequency conversion is generally achieved by nonlinear optics processes, for example, we obtain it thanks to the SHG, THG, SFG (Sum Frequency Generation), DFG (Difference Frequency Generation), OPG (Parametric Light Generation), or OPA (Parametric Light Amplification) processes.

Nonlinear optics is used in nonlinear spectroscopy and imaging [26,27]. First, SHG, THG, and two-photon absorption processes are used in label-free imaging of biological structures such as cells and biological tissues, and in materials science, among others, to analyze defects and structures in semiconductors [28-30]. Thanks to modern technologies, obtaining

information on the structural, molecular, and functional properties of the tested materials is possible. Nonlinear spectroscopy and imaging are fast, high-resolution measurement methods. When using these methods in medical imaging, there is no need to use dyes, which allows the recording of "raw" tissue structures. The lack of the need to use dyes increases the reliability of the obtained results, because staining can change the biological functions of tissues and can also be toxic. In addition, the SHG process detects non-centrosymmetric structures such as collagen, and the THG process detects phase boundaries, for example, cell membranes [31,32]. Wound healing, tumor development, and extracellular matrix remodeling are observed based on such measurements. TPA effects are also used in medical imaging and are useful for imaging deep structures. The use of SHG and THG for imaging in materials science enables, among many applications, the detection of crystallographic defects, the study of grain boundaries, and the quality control of thin films.

Another example of the application of optical nonlinear effects, this time THG effects, are optical switches and modulators, used in ultrafast optical routers, optical fiber telecommunications, or photon computers [33,34]. Their operation is based primarily on the Kerr effect, which is classified as a third-order nonlinear phenomenon. The purpose of optical switches is to control the transmission of light using another or the same optical signal. When the light intensity reaches a certain threshold, the refractive index changes. This change in the refractive index simultaneously changes the optical path and interference conditions. In this way, optical signals can be turned on or off. The operation of modulators is also based on the change in the refractive index, which allows for dynamic modulation of the signal in the optical domain. This avoids converting energy into an electrical signal, which positively affects the efficiency and speed of information transfer. Delays and energy losses are reduced, which is important from the point of view of practical and modern technical solutions. It is also worth mentioning the phenomenon of phase self-modulation, which serves to broaden the spectrum of a light pulse and is used in optical tomography and spectroscopy [35]. Another noteworthy phenomenon is the photorefractive effect, which uses the Kerr effect and can be used for dynamic holography [36].

Nonlinear optical effects are also used in optical limiter technology [37,38]. In such devices, the RSA effect is usually used, but also the Kerr effect. The purpose of optical limiters is to protect detectors and eyes from intense radiation.

An interesting application of NLO is its use in optical memories, where the mechanisms of changing the refractive index, multiphoton absorption, e.g., TPA, and optical bistability are used [39,40]. The advantages of optical memories include multi-layer recording (3D), fast data access, high recording density, and resistance to electromagnetic interference.

Potential areas of application of nonlinear optical effects include quantum photonics, secure quantum communication (QKD), and neurophotonics [41]. Quantum photonics aims to use single photons and their quantum states to process information, communicate, and perform calculations. Ensuring completely secure data transmission is also possible through the principles of quantum mechanics. Neurophotonics, on the other hand, is to be used to treat neurological diseases, study brain plasticity, and design neurointerfaces, e.g., brain-computer.

The applications of nonlinear optics are extensive and have a great chance of success. The possibilities of this branch of physics are so far unlimited. The achievements in this field of science have contributed to the development of technology in medicine, materials science, and broadly understood optoelectronics. On the other hand, searching for new materials with better nonlinear optical properties is very important. Materials that stand out from others are still sought with a fast response time, high nonlinear response, the lowest possible optical losses, or low production costs.

References

1. S. Kielich, Molekularna optyka nieliniowa. *Polish Scientific Publishers PWN* (1997) Warsaw, Poznan
2. Y.R. Shen, The Principles of Nonlinear Optics. *John Wiley & Sons* (1984) New York
3. D.A. Pérez-Carlos *et al.* Free Maxwell equations in vacum in orthogonal curvilinear coordinates and some applications: Helmholtz equation, poynting vector, and energy density. *Eur. Phys. J. Plus* (2024) 139, 792, https://doi.org/10.1140/epjp/s13360-024-05608-y
4. N. Bloembergen, Nonlinear Optics. *W.A. Benjamin Inc.* (1965)
5. P.A. Franken *et al.* Generation of optical harmonics. *Phys. Rev. Lett.* (1961) 7, 4, 118-119, https://doi.org/10.1103/PhysRevLett.7.118
6. Z. Gu *et al.* Two-photon pumped lead halide perovskite nanowire lasers. arXiv:1510.03987v1, access: May 2025
7. Y. He *et al.* Ultrafast All-Optical Modulation and Efficient Third-Harmonic Generation in Two-Dimensional Perovskite Heterostructures. *ACS Photonics* (2024) 11, 2, 604–612, https://doi.org/10.1021/acsphotonics.3c01485
8. J.H. Lin *et al.* Nonlinear Absorption in 2D Ruddlesden–Popper Perovskites: Pathways to Ultrafast Optical Applications. *J. Phys. Chem. Lett.* (2024) 15, 38, 9644–9651, https://doi.org/10.1021/acs.jpclett.4c01673
9. Y. Xie *et al.* Artificial Second-Order Nonlinear Optics in a Centrosymmetric Optical Material BiVO4: Breaking the Prerequisite for Nonlinear Optical Materials. *ACS Omega* (2019) 4, 1, 1045–1052, https://doi.org/10.1021/acsomega.8b02453
10. J. Shi *et al.* Nonlinear Optical Properties from Engineered 2D Materials. *Molecules* (2023) 28, 6737, https://doi.org/10.3390/molecules28186737
11. J. Lin *et al.* Phase-Matched Second-Harmonic Generation in an On-Chip LiNbO3 Microresonator. *Phys. Rev. Appl.* (2016) 6, 014002, https://doi.org/10.1103/PhysRevApplied.6.014002
12. H.J. Liu *et al.* Phase matching analysis of noncollinear optical parametric process in nonlinear anisotropic crystals. *Opt. Commun.* (2001) 197, 4–6, 507-514, https://doi.org/10.1016/S0030-4018(01)01475-4

13. J.F. Reintjes, Nonlinear optical parametric processes in liquids and gases. *Academic Press* (1984)
14. D. A. Kleinman, Theory of Second Harmonic Generation of Light. Phys. Rev. 128 (1761, 1962)
15. D. A. Kleinman, Nonlinear Dielectric Polarization in Optical Media, *Phys. Rev.* (1997, 1962) 126
16. X.L. Yang and S.W. Xie, Expression of third-order effective nonlinear susceptibility for third-harmonic generation in crystals. *Appl. Opt.* (1995) 34, 6130-6135, https://doi.org/10.1364/AO.34.006130
17. R.I. Woodward *et al.* Characterization of the second- and third-order nonlinear optical susceptibilities of monolayer MoS2 using multiphoton microscopy. *2D Mater.* (2017) 4 011006, 10.1088/2053-1583/4/1/011006
18. R.W. Boyd, Nonlinear Optics. *Academic Press* (2008)
19. P. Khan *et al.* Pulse-duration dependence of saturable and reverse saturable absorption in ZnCo2O4 microflowers. arXiv:2009.13226v2, access: May 2025
20. Y. Zhao *et al.* Nonlinear meta-optics towards applications. *PhotoniX* (2021) 2, 3, https://doi.org/10.1186/s43074-021-00025-1
21. G. Liu *et al.* Nonlinear optics and photonics applications of two-dimensional materials. *Nanophotonics* (2024) 393-440, https://doi.org/10.1016/B978-0-323-90614-2.00007-9
22. P.Q. Liu *et al.* High-power (1.1W) green (532nm) laser source based on single-pass second harmonic generation on a compact micro-optical bench. *Nonlinear Frequency Generation and Conversion: Materials, Devices, and Applications X Proceedings* (2011) 7917, 791704, https://doi.org/10.1117/12.878013
23. R.A. Kumar, Borate Crystals for Nonlinear Optical and Laser Applications: A Review. *J. Chem.* (2013) 1, https://doi.org/10.1155/2013/154862
24. P. Gong *et al.* Inorganic planar π-conjugated groups in nonlinear optical crystals: review and outlook. *Inorg. Chem. Front.* (2020) 7, 839-852, 10.1039/C9QI01589B
25. J.L.H. Clabel *et al.* Structural, linear and nonlinear optical properties of perovskite BaTiO3 tri-doped Er/Yb/Zn embedded in tellurium-zinc glass. *Ceramics International* (2024) 50, 4, 5948-5954, https://doi.org/10.1016/j.ceramint.2023.11.085

26. S. Yue *et al.* Multimodal nonlinear optical microscopy. *Laser & Photonics Reviews* (2011) 5, 4, A19-A22, 465-606, https://doi.org/10.1002/lpor.201000027
27. F.J. Avila, A Review of Non-Linear Optical Imaging Techniques for Cancer Detection. *Optics* (2024) 5, 416-433, https://doi.org/10.3390/opt5040031
28. E.J. Lee *et al.* n-vivo and label-free imaging of cellular and tissue structures in mouse ear skin by using second- and third-harmonic generation microscopy. *JKPS* (2015) 66, 597–601, https://doi.org/10.3938/jkps.66.597
29. A. Zoumi *et al.* Imaging Cells and Extracellular Matrix In Vivo by using Second-Harmonic Generation and Two-Photon Excited Fluorescence. *Proceedings of the National Academy of Sciences* (2002) 99(17):11014-9, DOI:10.1073/pnas.172368799
30. K. Yao *et al.* Nanoscale Optical Imaging of 2D Semiconductor Stacking Orders by Exciton-Enhanced Second Harmonic Generation. *Adv. Opt. Mater.* (2022) 10, 12, 2200085, https://doi.org/10.1002/adom.202200085
31. R.M. Williams *et al.* Interpreting Second-Harmonic Generation Images of Collagen I Fibrils. Biophys. J. (2005) 88, 2, 1377 – 1386, doi: 10.1529/biophysj.104.047308
32. B. Weigelin *et al.* Third harmonic generation microscopy of cells and tissue organization. *J Cell Sci* (2016) 129 (2): 245–255, https://doi.org/10.1242/jcs.152272
33. Y. Liu *et al.* High-Efficiency Third-Harmonic Generation Enabled by Merging Bound States in the Continuum. *SSRN* (2025), https://dx.doi.org/10.2139/ssrn.5182881
34. G. Soavi *et al.* Broadband, electrically tunable third-harmonic generation in graphene. *Nat. Nanotech* (2018) 13, 583–588, https://doi.org/10.1038/s41565-018-0145-8
35. D. Garg and A. Kumar, Highly coherent on-chip mid-infrared supercontinuum generation from 1.5 to 25 μm in CdTe-based Rib waveguide. *OQE* (2025) 57(1), DOI:10.1007/s11082-024-08007-w
36. D.J. McGee and M.D. Matlin, Photorefractive polymers: Materials science, thin-film fabrication, and experiments in volume holography. *Am. J. Phys.* (2001) 69, 10,1055-1063, doi: 10.1119/1.1387042
37. Z. Fatima *et al.* A review: An overview on third-order nonlinear optical and optical limiting properties of Schiff bases. *J. Mol. Struct.* (2023) 1292, 15, 136062, https://doi.org/10.1016/j.molstruc.2023.136062

38. J.W. You *et al.* Nonlinear optical properties and applications of 2D materials: theoretical and experimental aspects. *Nanophotonics* (2019) 8(1): 63–97, https://doi.org/10.1515/nanoph-2018-0106
39. S. Chen *et al.* Bistability and self-pulsation phenomena in silicon microring resonators based on nonlinear optical effects, *Opt. Express* (2012) 20, 7454-7468, https://doi.org/10.1364/OE.20.007454
40. A.A. Nikitin *et al.* Optical bistable SOI micro-ring resonators for memory applications, *Opt. Commun.* (2022) 511, 127929, https://doi.org/10.1016/j.optcom.2022.127929
41. F. Xia *et al.* Neurophotonics beyond the surface: unmasking the brain's complexity exploiting optical scattering. *Neurophotonics* (2024) Vol. 11, Issue S1, S11510, https://doi.org/10.1117/1.NPh.11.S1.S11510

CHAPTER 3: EXPERIMENTAL TECHNIQUES FOR THE PREPARATION AND CHARACTERIZATION OF THIN FILMS

This chapter discusses the experimental techniques used to prepare and characterize the optoelectric properties of thin film samples. The information presented below is the result of the experiments and literature searches. The technique used to produce low-dimensional structures was the classical Physical Vapor Deposition (PVD) technique supported by the material co-deposition process, called Physical Vapor co-Deposition (PVco-D). The PVco-D technique allowed the production of samples with different compositions. The characterization of the obtained structures focused on morphological properties, which were studied using Atomic Force Microscopy (AFM), linear optical properties such as UV-VIS-NIR spectroscopy, and photoluminescence (PL), nonlinear optical properties such as Second and Third Harmonic Generation, Corona Poling, and Z-scan, as well as electrical and photovoltaic properties. The linear optical properties were studied over a wide temperature range to detect phase transitions in the studied materials. Additionally, the thin film samples' aging tests were carried out by performing UV-VIS-NIR spectroscopic and AFM morphological measurements.

3.1. Physical Vapor co-Deposition

PVD and PVco-D are techniques that allow the creation of low-dimensional 2D and 3D structures, reaching thicknesses of several to thousands of nanometers in high vacuum conditions. The PVD technique is a classic technique of physically obtaining thin layers from the gas phase, and the PVco-D technique is its modification [1,2]. Historically, the PVD method was developed in the 1850s by Michael Faraday, who experimented with metal deposition [3]. Modern forms of PVD have been intensively developed since the 1930s, and their commercialization took place after World War II [4-6].

In the process of obtaining thin film structures using PVD, three successive stages can be distinguished:

- sublimation of the material and obtaining a stream of its vapors,
- free passage of vaporized particles from the source to the substrate,
- condensation of the material particles on the substrate and gradual growth of the layer.

The modification of this process to the PVco-D form consists of the simultaneous sublimation of at least two different materials. This is possible thanks to vacuum sputters equipped with more than one independent thermal source. The PVco-D process is schematically illustrated in Figure 3.1. It takes place in a tightly closed vacuum chamber under high vacuum conditions at pressures of the order of $10^{-5}\,Tr$. Previously prepared substrates are placed in the upper part of the vacuum chamber, and the materials to be evaporated are placed in the lower part. As mentioned above, the traditional PVD method consists of the sublimation of only one material, which results in obtaining a thin layer of this material. In the PVco-D method, more than one material is sublimated at the same time. The obtained vapor streams of all materials mix in the vacuum chamber and are deposited on the substrates. In this way, the molecules of different materials create new bonds on the surface of the substrates, creating new thin film structures with physicochemical properties different from those of the sublimed materials. The introduction of co-deposition to the classical PVD technique enables the creation of various new materials with selected compositions, including hybrid perovskites. The 2D structures obtained by this method can be monocrystalline, polycrystalline, or amorphous.

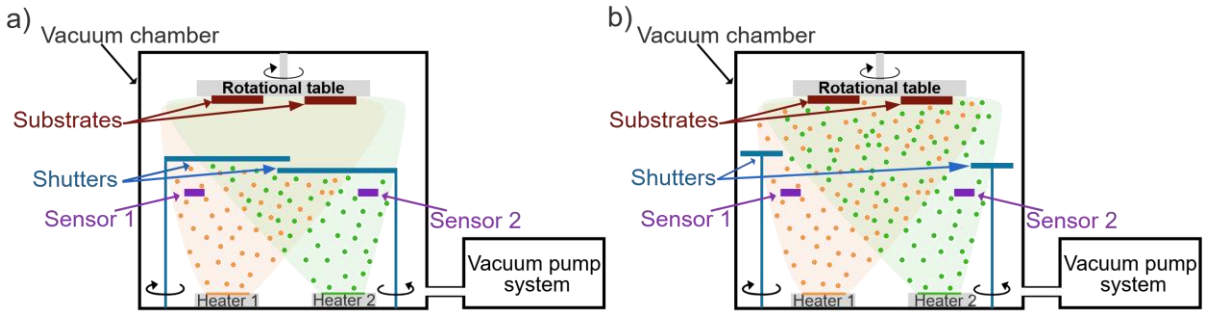

Figure 3.1. The idea of the vacuum evaporation process in co-Deposition mode: shutters open (a), shutters close (b).

As shown in Figure 3.1, the vacuum chamber also contains shutters and thickness sensors. The shutters facilitate co-deposition in addition to the vapor sources and substrates. They can rotate around a vertical axis. After all sublimated materials have reached the expected deposition rate, the shutters are opened, and only then do the particles have the opportunity to reach the substrates and form a thin layer on them. Information about the thickness of the thin layer is provided by piezoelectric thickness sensors. The thickness sensors and shutters play important roles in the deposition of structures, especially structures with a strictly defined percentage composition.

The PVco-D technique is an extremely useful tool compared to other thin film techniques. This technique enables the fabrication of structures with a defined chemical composition and a controlled percentage of individual components. It also allows the formation of both single-layer and multilayer structures. Usually, the sublimation temperatures of individual components are different, and it is impossible to obtain such complex structures using other known deposition techniques. Another great advantage is the ability to control the conditions of pressure, temperature, and evaporation rate of materials during the deposition of thin layers. Thanks to this, the structures obtained have precisely the same composition as intended. The ability to control these parameters also affects the repeatability of the layers obtained. In addition, the high vacuum conditions during the entire deposition process guarantee the purity of the obtained structures, and consequently their high-quality and uniformity. High vacuum also provides appropriate conditions for sublimation and thermally isolates the sources of vapors. The PVD method is used for coating complex 2D shapes and is considered environmentally friendly. The disadvantages of this deposition technique include the need to use high vacuum, which may be a limitation for large productions [7].

The Thin Film Deposition System - NANO 36™ (Kurt J. Lesker Company, Figure 3.2) was used to produce thin film structures studied in this work, with thicknesses ranging from several dozen to a thousand nanometers. The apparatus is equipped with two independently working thermal sources, which enable the PVco-D process to be carried out. All thin film and multilayer structures described in the following chapters were obtained using this apparatus.

Figure 3.2. Thin Film Deposition System - NANO 36™ (Kurt J. Lesker Company) for producing low-dimensional structures.

3.2. Atomic Force Microscopy

The AFM imaging technique was developed in 1986 by G. Binning, C. Quate, and C. Gerber as an extension of another, already known technique, Scanning Tunneling Microscopy (STM) [8]. In the 1990s, it was significantly developed, and today it is one of the most important imaging techniques in nanotechnology, solid state physics, and materials engineering. AFM is a surface topography imaging technique that uses physical interactions between the tip of the measuring probe and the surface of the tested sample. Based on these interactions, a three-dimensional map of the topography of this surface is created on a nanometric scale. AFM allows for imaging a wide range of materials, regardless of their transparency, conductivity, and hardness, and for carrying out measurements in air or liquid. This technique also allows for simultaneous examination of topographic, mechanical, and adhesive properties.

The AFM system consists of three basic elements: a measuring probe placed on a flexible cantilever, a laser system, and a detection system – most often a photodiode. A standard AFM system is shown in Figure 3.3. The measuring probe of an atomic force microscope is a needle, usually in the shape of the letter *V*, placed on a flexible arm. The probe, approaching the tested

surface at several hundred nanometers, interacts with it. As a result, the flexible cantilever bends – it is attracted or repelled, and its movement is continuously recorded by the detection system. The data obtained from the measurement are not a direct image of the sample, as in optical microscopy, but create a map of the probe height measurement. Based on such mapping, an image is computer processed that reflects the 3D topography of the surface of the tested material.

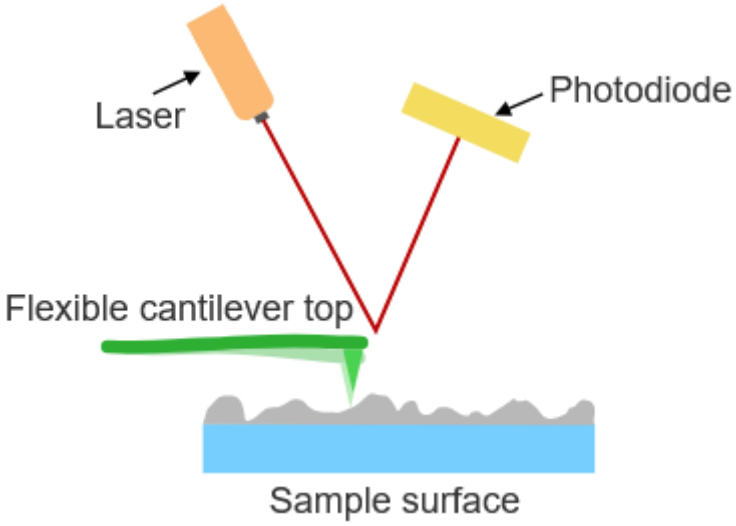

Figure 3.3. Diagram showing the basic components of an atomic force microscope – the measuring probe placed on a flexible cantilever, the laser system, and the detection system.

The interaction between the measuring probe and the tested surface is theoretically described by the Lennard-Jones potential. Based on the type of interaction, different operating modes are distinguished: contact, non-contact, and intermittent contact (Figure 3.4) [9,10].

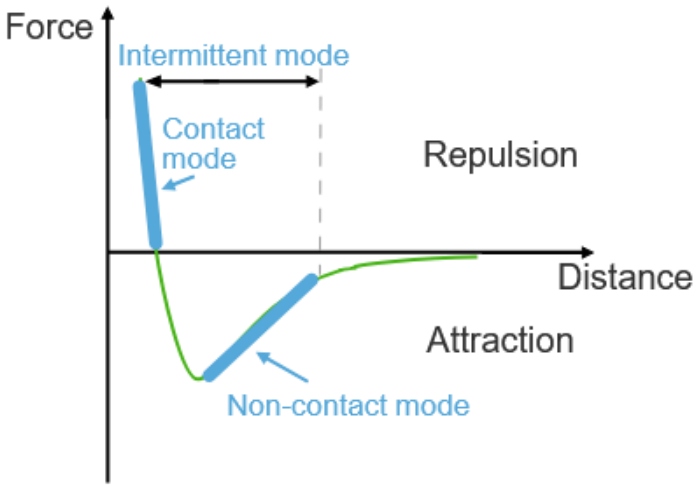

Figure 3.4. Lennard-Jones potential describing the interaction of the AFM measuring probe with the tested surface, with the three AFM microscope operating modes marked.

The contact mode of measurement uses short-range interatomic forces, and the measuring tip directly touches the surface of the tested sample. Repulsive forces appear between the atoms of the tip and the sample's atoms, the source of which is the interaction between the electron orbitals of the atoms of the sample and the measuring tip. This mode of operation allows for very accurate images of the surface, but in the case of soft materials, the measuring tip moving over the tested surface can damage it. The non-contact mode of measurement uses long-range interatomic forces, and the measuring tip does not touch the surface of the tested sample.

The lever with the tip vibrates close to the resonance frequency. These vibrations have an amplitude from several to several dozen nanometers. As the distance between the tip and the sample decreases, the frequency and period of the lever vibrations change. Based on these changes, a topographic image of the surface is created. This mode of operation works well for materials sensitive to deformation.

The intermittent contact mode uses both short-range and long-range forces in the measurement. The lever with the measuring tip placed close to the tested surface (closer than in the non-contact mode) is set in vibrations close to the resonance frequency. The measuring tip briefly and cyclically comes into contact with the tested surface, which reduces its vibration

amplitude. This mode of operation is characterized by higher scanning sensitivity than the contact mode and allows for avoiding damage to the surface of the tested sample.

The AFM technique provides information on topography, structure, roughness, crystallite size, or type of the examined surface. A more detailed analysis is performed using the Minkowski Functionals Method (MFM). This method determines the spatial distribution of holes or crystallites on the examined surface and how the structure grows. Among the Minkowski Functional Methods, there are three distinguished – Minkowski Volume $V(h)$, Minkowski Boundary $S(h)$, Minkowski Connectivity $\chi(h)$, which are defined as follows [11,12]:

$$V(h) = \frac{N_B}{N_B + N_W} \quad \text{(Eq. 3.1)}$$

$$S(h) = \frac{N_{bounded}}{N_B + N_W} \quad \text{(Eq. 3.2)}$$

$$\chi(h) = \frac{n_B - n_W}{N_B + N_W} \quad \text{(Eq. 3.3)}$$

where:

h – height relative to the ground at which the topography of the layer is analyzed,

N_B – material points,

N_W – empty points (air),

$N_{bounded}$ – limited pixels,

n_B – number of isolated areas at height h ,

n_W – number of isolated islands at height h .

To determine the structural properties of the thin films studied in the work, AFM studies and FMs analysis were performed. AFM imaging was performed in the contact mode using

the NanoSurf EasyScan 2 instrument with a Sicon-A cantilever (Figure 3.5). The results obtained were analyzed using the Gwyddion 2.67 software.

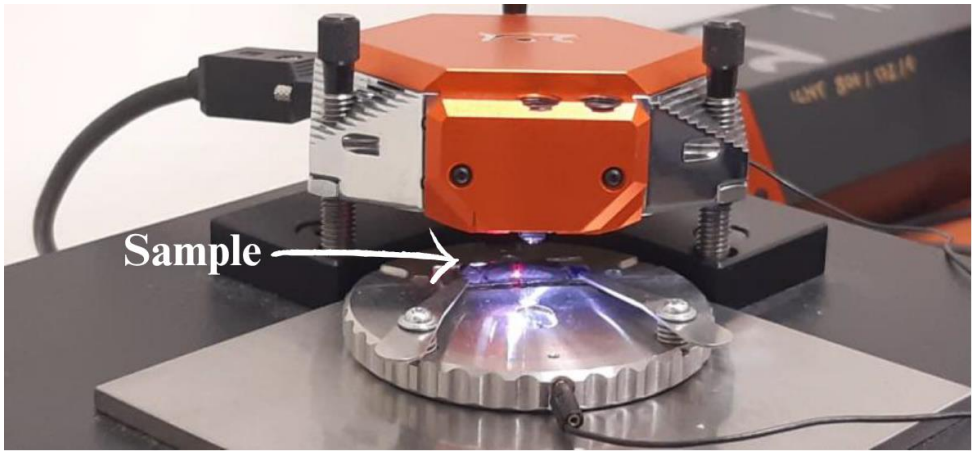

Figure 3.5. Photograph of the NanoSurf EasyScan 2 Atomic Force Microscope used for measurements.

3.3. Spectroscopy characterization

3.3.1. UV-VIS-NIR spectroscopy

To characterize the thin film samples spectroscopically, measurements of transmission spectra were performed in the UV-VIS-NIR range at room temperature. An Analytik Jena UV-VIS-NIR spectrometer was used, which performed measurements in the wavelength range of 250 – 1100 nm with a resolution of 1 nm. Based on the obtained measurement results, the absorption bands of the tested materials were identified, and the spectroscopic quality of the thin films obtained by the PVD technique was checked.

The classic measurement of transmission spectra was extended to include measurements of transmission spectra as a function of temperature. The introduction of such an idea was aimed at detecting phase transitions occurring in the tested hybrid perovskite samples under the influence of temperature changes. The measurement system shown schematically in Figure 3.6 was used. In addition to the spectrometer and computer, it included a Janis SuperTran-VP cryostat, a Lake Shore Cryotronics temperature controller, and a vacuum pump with a pressure sensor. The cooling medium was liquid nitrogen, the temperature

of which at atmospheric pressure is 77 K. The measurements were carried out for the temperature range of 80 - 310 K with a step of 10 K, starting from the lowest temperature. Thanks to the vacuum system, they were carried out in a vacuum under a pressure in the order of $10^{-3}\ Tr$.

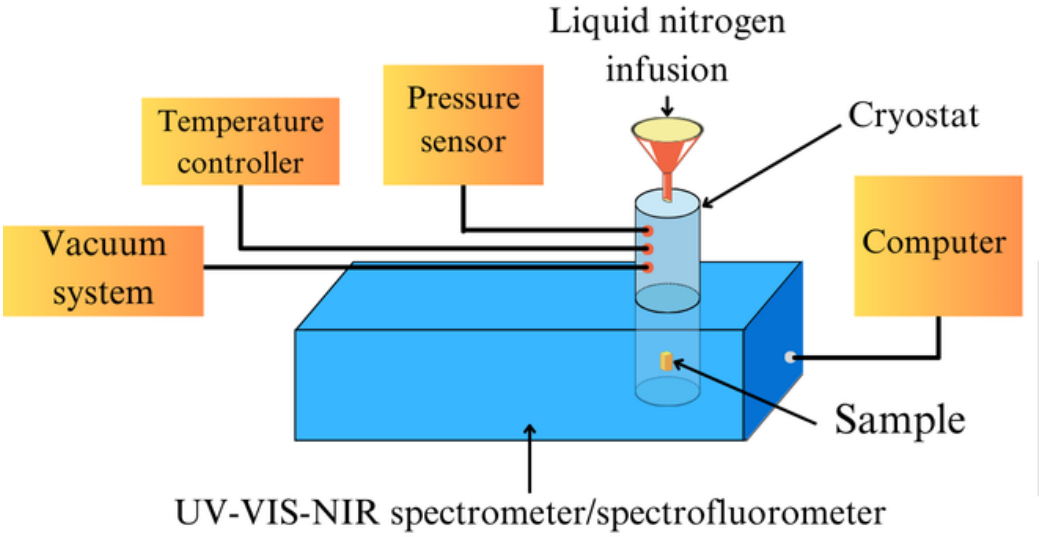

Figure 3.6. Schematic diagram of the measuring system for measuring transmission and photoluminescence spectra as a function of temperature.

3.3.2. Photoluminescence

Material luminescence is a phenomenon of radiation emission by a material due to its previous excitation, i.e., transfer of electrons to higher energy levels. Luminescence occurs when excited electrons return to the ground state, which is accompanied by the emission of excess energy in the form of electromagnetic radiation. It can be caused by various factors, for example, electric current or chemical reaction, while luminescence induced by light was studied in this dissertation [13]. Such material luminescence is called photoluminescence (PL).

Photoluminescence is divided into fluorescence and phosphorescence based on the lifetime of the excited state. In the case of fluorescence, the lifetime of the excited state is in the order of nanoseconds, and light emission occurs very quickly after excitation. However, it is the opposite for phosphorescence – light emission lasts longer because electrons giving off energy pass through an intermediate triplet state. The processes related to photoluminescence

are well illustrated by the Jablonski diagram (Figure 3.7) [14]. It describes how molecules give off energy after excitation. The main elements of the diagram are the energy levels S and T. S_0 represents the ground state, and S_1, S_2 the subsequent excited states. The energy levels S are singlet levels, while the level T_1 is the lowest excited triplet state. Each state can contain numerous vibrational levels designated as 0, 1, and 2, respectively. When a photon initially excites the material, an electron passes from the ground to the excited state. The Jablonski diagram is indicated by a vertical arrow pointing upwards. Then, several processes can occur associated with the transition of the electron from the excited state to lower energy levels. This can be an internal conversion process involving a non-radiative transition between electronic levels, and the excess energy can be given off as heat. Another process can be fluorescence, or the transition from the excited singlet state S_1 to the ground state S_0. Another possible transition can be the transition from the excited singlet state S_1 to the excited triplet state T_1. Such a transition is called an intersystem transition. If another transition from the T_1 to the ground state S_0 occurs, the phenomenon is called phosphorescence.

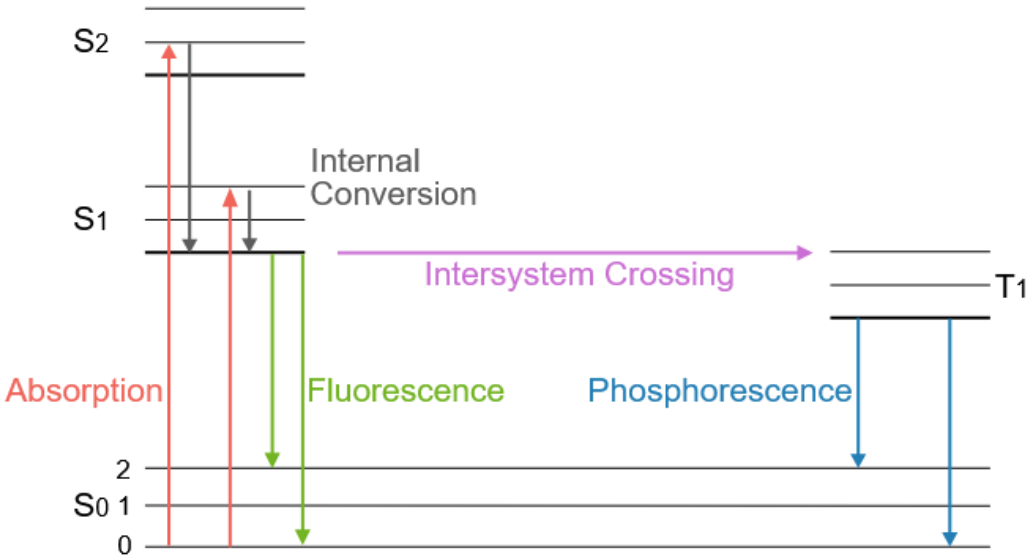

Figure 3.7. Jablonski diagram.

To distinguish between different types of luminescence, a parameter known as the decay time was introduced. This is the time an electron is in an excited state before returning to the ground state. Knowledge of the decay time of a given material helps to determine the presence of energy traps, quantum efficiency, or the dynamics of electron-hole pair recombination

processes. It is measured as the decay of the emission intensity over time, which is described by an exponential function:

$$I(t) = I_0 \, e^{-\frac{t}{\tau}} \qquad \text{(Eq. 3.4)}$$

where:

$I(t)$ – photoluminescence intensity at time t ,

I_0 – initial intensity immediately after arousal,

τ – time of decay.

PL measurements were made using a HORIBA FluoroMax-4P spectrofluorometer. The HORIBA FluoroMax-4P spectrofluorometer is a device used to measure photoluminescence of samples in the solid state (e.g., thin layers) and in the liquid state. This device enables recording of excitation and emission spectra by measuring the intensity of photoluminescence and its change in time, polarization, and temperature. The HORIBA FluoroMax-4P spectrofluorometer has a 150 W CW Ozone-free xenon arc excitation source. It is a continuous-wave light source with a broad emission spectrum ranging from UV to NIR. The lamp uses ozone-free glass, which blocks deep UV radiation (<240 nm). Light from the source is collected by an elliptical mirror collects light from the source and then focused onto the narrow slits of the monochromator. The housing of the xenon source is separated from the monochromator by a quartz window, which dissipates heat. The spectroscopic spectrum is obtained by rotating the slits of the monochromator and recording the intensity by the detector for each wavelength. The diffraction grating used for the spectrofluorometer measurements contains 1200 slits per millimeter.

Similarly to UV-VIS-NIR spectroscopic measurements, PL measurements were also performed as a function of temperature, in the temperature range of 80 – 310 K with 10 K steps, starting from the lowest temperature. The measurement setup was used, which is schematically shown in Figure 3.6. It consisted of a spectrofluorometer, a computer, a Janis SuperTran-VP

cryostat, a Lake Shore Cryotronics temperature controller, and a vacuum pump with a pressure sensor. Liquid nitrogen was used as a cooling medium, and the measurements were performed at a pressure of $10^{-3}\,Tr$. As before, PL spectra were measured as a function of temperature to identify phase transitions occurring in the studied hybrid perovskite thin films.

3.4. Aging tests

The aging tests were conducted to determine how the environment affects the structural properties and transmission of the tested thin hybrid perovskite films made using the PVD technique. Perovskites are unstable materials, and their proper storage is vital during their studies [15-17].

Immediately after the thin film structures were made using the PVD method, structural measurements were made using the AFM method and UV-VIS-NIR transmission measurements. The measurements were carried out at room temperature, in normal ambient conditions. The tested samples were placed in containers filled with argon, which were tightly closed. The boxes with the samples were stored in a dark place, in normal ambient conditions. The structural and spectroscopic measurements were repeated systematically over half a year, and the results were compared.

The choice of argon as a medium for storing perovskite samples is not accidental. Argon is a colorless, odorless, chemically inert noble gas from the eighteenth group of the periodic table of elements. It is a protective gas against moisture and prevents oxidation [18]. Argon has a higher density than air and therefore covers samples well. Due to the chemical properties of argon and the fact that it does not enter into chemical reactions with samples, it is a good medium that can be a protective barrier during long-term sample storage.

3.5. Second and Third Harmonic Generation experiments

The second- and third-order nonlinear optical properties of materials were investigated using the Maker Fringes technique (Figure 3.8). The Maker Fringes technique involves rotating the test sample around an axis perpendicular to the laser beam and measuring the SHG or THG intensity as a function of the angle of incidence of the laser beam. The measurement produces Maker Fringes, i.e., a graph of the harmonic signal intensity as a function of the angle of incidence of the laser beam [19,20]. An intense light source (pulsed laser) and a photomultiplier that is very sensitive to low light signals are necessary to perform this experiment.

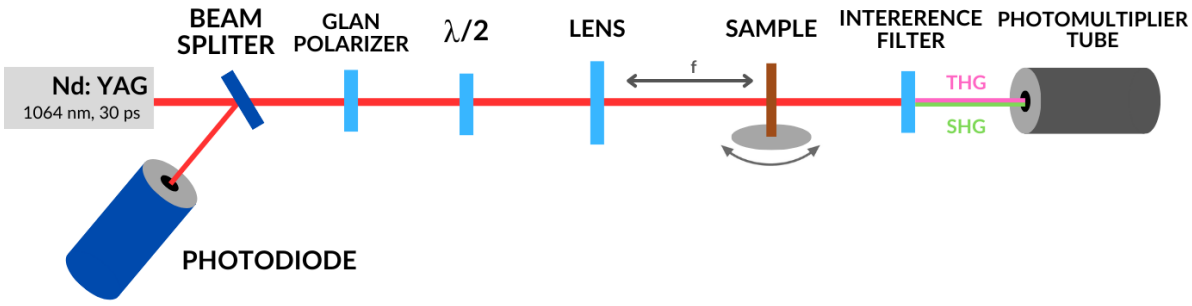

Figure 3.8. Experimental setup for SHG and THG measurements using the Maker Fringes method.

The excitation source in the SHG and THG measurement system is a laser beam from a mode-locked Nd:YAG laser (Ekspla, PL2250 series). This pulsed laser emits waves of 1064 nm, with a pulse duration of 30 ps and a processing frequency of 10 Hz. The light beam emerging from the laser initially falls on a splitter, which transmits part of the beam and directs part directly to the photodiode. The beam falling into the photodiode is responsible for acquisition synchronization. The beam passing through the splitter hits the Glan-Taylor polarizer, a half-wave plate ($\frac{\lambda}{2}$), and a focusing lens with a focal length of 250 mm. The lens focuses the laser beam precisely on the sample, which is placed on a rotating stage. By rotating the stage, the angle of incidence of the focused laser beam relative to the normal to the sample surface is changed. The stage can be rotated from -60° to +60° in 0.5° steps. The radiation beam passing through the sample contains the fundamental wavelength and the signal of the generated higher harmonic. To record the signal corresponding only

to the higher harmonics, a KG3 filter is placed behind the sample, which removes the fundamental wavelength. Then, an appropriate interference filter isolates the higher harmonics generated signal. Immediately afterwards, the signal is detected by the Hamamatsu R1828-01 photomultiplier and recorded on the computer. The difference between experiments for detecting SHG and THG lies in the interference filter and the reference material. In the case of SHG measurements, a 532 nm interference filter is used and a quartz plate cut in the y axis, 0.5 mm thick, as the reference material. In the case of THG measurements, a 355 nm interference filter is used, and a 1 mm thick silica (SiO_2) plate as the reference material. Quartz and silica are materials with well-known nonlinear optical properties and known SHG and THG signal intensity profiles. The SHG and THG signals of the reference materials are shown in Figure 3.9.

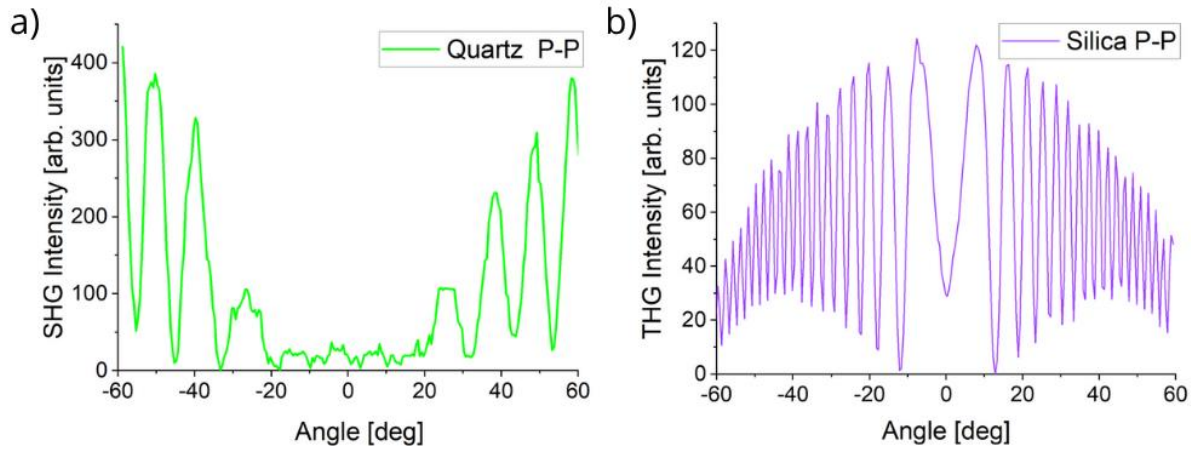

Figure 3.9. Experimentally obtained Maker Fringes obtained for quartz plate (a) and silica plate (b), being reference materials for SHG and THG signals, respectively.

3.6. Theoretical models for calculating second-order nonlinear susceptibility

In the context of SHG, several theoretical models have been developed to describe this phenomenon and to enable the calculation of parameters characterizing it, including $\chi^{(2)}$. Below, only the most important theoretical models are described, which are used in a wide range of sample types – in the form of powders, thin films, solutions, and bulk materials. Each model has its own characteristic features and limitations, so it is worth taking a closer look at them to select the optimal model for a given sample.

3.6.1. Lee Model

The Lee Model is a theoretical model developed by Lee *et al.* in 1978 [21]. It is an extension of the classical Maker Fringes technique. This Model directly compares the second-order nonlinear optical properties of a reference material, i.e., a quartz plate, with the material under study. It was developed to describe SHG in thin film materials more accurately and considers the layer thickness d, quartz coherence length $l_{C,quartz}$, and the absorption losses of the fundamental wave and the generated second harmonic. The disadvantages of the Lee Model include the fact that it requires precise knowledge of the layer thickness and optical coefficients, and that it does not dynamically account for dispersion in the layer but assumes constant values of the refractive index n and extinction coefficient κ. The second-order nonlinear optical susceptibility $\chi^{(2)}$ of a sample of thickness d is given by:

$$\chi^{(2)} = \chi^{(2)}_{quartz} \frac{2}{\pi} \frac{l_{C,quartz}}{d} \sqrt{\frac{I_{2\omega}}{I_{2\omega,quartz}}} \qquad \text{(Eq. 3.5)}$$

where:

$I_{2\omega}$ – SHG intensity of the sample,

$I_{2\omega,quartz}$ – SHG intensity of the reference sample – quartz plate,

$l_{C,quartz}$ – coherence length of the reference sample,

$\chi^{(2)}_{quartz} = 1.00 \frac{pm}{V}$ [22].

The coherence length of the reference sample is calculated using Eq. 3.6.

$$l_{C,quartz} = \frac{\lambda_\omega}{4\left(n_{quartz(2\omega)} - n_{quartz(\omega)}\right)} \qquad \text{(Eq. 3.6)}$$

λ_ω – fundamental beam wavelength

$n_{quartz(2\omega)} = 1.547$ – refractive index of the reference material for SHG [23]

$n_{quartz(\omega)} = 1.534$ – refractive index of the reference material for the fundamental beam [23]

In case the optical absorption of the material has to be taken into account in the modeling, $\chi^{(2)}$ also depends on the absorption coefficient α and is expressed by the equation:

$$\chi^{(2)} = \chi^{(2)}_{quartz} \frac{2}{\pi} \frac{\frac{1}{2}\alpha d}{1 - e^{-\frac{1}{2}\alpha d}} \frac{l_{C,quartz}}{d} \sqrt{\frac{I_{2\omega}}{I_{2\omega,quartz}}} \quad \text{(Eq. 3.7)}$$

3.6.2. Kurtz-Perry Model

The Kurtz-Perry Model is a classic technique for studying SHG in powder materials, especially microcrystalline ones. The Model was developed in 1968 to enable measurements of materials in powders or microcrystalline materials, when they are not available in the form of large crystals [24]. SHG modeling is performed by comparing the SHG intensity generated by the tested material with a reference powder, which is POM (3-methyl-4-nitropyridine-1-oxide). The advantages of the Kurtz-Perry Model are simplicity, speed, and the possibility of studying materials in powder form. However, in the case of a microcrystalline material, the size of the crystallites present in the sample affects the phase matching, and this affects the SHG intensity. This is the basic disadvantage of the described model, apart from not considering scattering and absorption in the tested material. The comparative formula for $\chi^{(2)}$ is expressed as follows:

$$\chi^{(2)} = \chi^{(2)}_{POM} \sqrt{\frac{I_{2\omega}}{I_{2\omega,POM}}} \quad \text{(Eq. 3.8)}$$

where:

$I_{2\omega}$ – relative maximum SHG intensity of the tested material,

$I_{2\omega,POM}$ – relative maximum SHG intensity of the POM reference material,

$\chi^{(2)}_{POM} = (21 \pm 3) \cdot 10^{-9}\, esu$ – second-order nonlinear optical susceptibility of the POM reference powder.

3.6.3. Herman-Hayden Model

The Herman-Hayden Model is a theoretical mathematical model used to study the bulk materials' and thin films' second-order nonlinear properties [25]. It is an extension of the Maker Fringes technique and considers phase matching, interference, and absorption effects in the tested material. The Model was developed in 1963 and was primarily intended to take into account realistic conditions of laser beam propagation in the tested sample. Its disadvantage is its mathematical complexity, which slows down the calculation process, as well as the assumption of the homogeneity of the medium, which makes the model ineffective in the analysis of non-crystalline materials. When the vertically polarized fundamental wave (S), passing through the sample, generates the horizontally polarized (P) second harmonic, the SHG intensity is expressed as follows:

$$I_{2\omega}^{(S\to P)} = \frac{128\pi^5}{\lambda_\omega^2\, c} \frac{\left[t_{af}^{(1S)}\right]^4 \left[t_{fS}^{(1S)}\right]^2 \left[t_{Sa}^{(2P)}\right]^2}{n_{2\omega}^2 \cos^2 \theta_{2\omega}} \left(\chi_{eff}^{(2)}\, I_\omega\, d\right)^2 e^{(-2\delta_1 + \delta_2)} \frac{\sin^2 \phi + \sinh^2 \Psi}{\phi^2 + \Psi^2} \quad \text{(Eq. 3.9)}$$

where:

λ_ω – fundamental wavelength,

I_ω – fundamental wave intensity,

$t_{af}^{(1S)}, t_{fS}^{(1S)}, t_{Sa}^{(2P)}$ – Fresnel transmission coefficients for air-layer, layer-substrate and substrate-air boundaries, respectively,

$\chi_{eff}^{(2)}$ – effective second-order nonlinear compliance,

$\theta_{2\omega}$ – angle of generated harmonic per sample,

ϕ, Ψ – phase angles,

δ_1, δ_2 – parameters related to absorption.

For a sample being a thin film whose transmission coefficient is close to 1, and for a substrate whose transmission coefficient is close to 1, the above equation is simplified to:

$$I_{2\omega}(\theta) = \frac{128\pi^5}{n_{2\omega}^2 \cos^2 \theta_{2\omega} \lambda_\omega^2 c}\left(\chi_{eff}^{(2)} I_\omega d\right)^2 \frac{\sin^2 \phi + \sinh^2 \Psi}{\phi^2 + \Psi^2} \quad \text{(Eq. 3.10)}$$

where the phase angles ϕ and Ψ:

$$\phi = \frac{2\pi d}{\lambda_\omega}(n_\omega \cos\theta_\omega - n_{2\omega} \cos\theta_{2\omega}) \quad \text{(Eq. 3.11)}$$

$$\Psi = \frac{2\pi d}{\lambda_\omega}\left(\frac{n_\omega \kappa_\omega}{\cos\theta_\omega} - \frac{n_{2\omega} \kappa_{2\omega}}{\cos\theta_{2\omega}}\right) \quad \text{(Eq. 3.12)}$$

and:

θ_ω – the angle of incidence of the fundamental wave on the sample,

κ_ω, $\kappa_{2\omega}$ – extinction coefficients of nonlinear material at frequencies ω and 2ω.

3.7. Theoretical models for calculating third-order nonlinear susceptibility

Several theoretical models have been developed to describe the THG phenomenon, based on the Maker Fringes technique. They allow understanding the mechanism of THG generation in the material and the calculation of $\chi^{(3)}$. Only selected theoretical models are described below.

3.7.1. Kubodera-Kobayashi Model

The Kubodera-Kobayashi Model is a classical empirical-theoretical model used to determine $\chi^{(3)}$ of thin film materials. It was developed in the 1970s [26]. It is characterized by simplicity and quick application in the experiment. Its disadvantage is that it does not consider complex multilayer effects and is highly sensitive to inaccuracy in thickness measurement. The Kubodera-Kobayashi Model is a comparative model that directly compares the maximum THG intensity of the tested sample with the reference material. The reference material

is a 1 mm thick SiO_2 plate. According to the described model, at low absorption of the material, $\chi^{(3)}$ is expressed as follows:

$$\chi^{(3)} = \chi^{(3)}_{silica} \frac{2}{\pi} \frac{l_{C,silica}}{d} \sqrt{\frac{I_{3\omega}}{I_{3\omega,silica}}} \qquad \text{(Eq. 3.13)}$$

where:

d – sample thickness,

$l_{C,silica}$ – coherence length of the reference sample,

$I_{3\omega}$ – THG intensity of the tested sample,

$I_{3\omega,silica}$ – THG intensity of the reference sample,

$\chi^{(3)}_{silica} = 2 \cdot 10^{-22} \frac{m^2}{V^2}$ – third-order nonlinear susceptibility of the reference material [22].

In a situation where optical absorption cannot be neglected, the absorption coefficient α must be included in Eq. 3.13, and then the expression describing $\chi^{(3)}$ looks as follows:

$$\chi^{(3)} = \chi^{(3)}_{silica} \frac{2}{\pi} \frac{l_{C,silica}}{d} \frac{\frac{1}{2}\alpha d}{1 - e^{-\frac{1}{2}\alpha d}} \sqrt{\frac{I_{3\omega}}{I_{3\omega,silica}}} \qquad \text{(Eq. 3.14)}$$

3.7.2. Reintjes Model

The Reintjes Model was introduced in the 1970s and used for THG analysis and modeling [27]. The Reintjes Model explains the origin of Maker Fringes and helps to calculate $\chi^{(3)}$ of dielectric materials. It is a model based on the fundamental principles of electromagnetism and is universal - it can be used for both solids and liquids. The Reintjes Model assumes no absorption of the tested material, requires precise measurement of the sample thickness, and is not accurate for very thin layers due to the slowly varying amplitude approximation (SVEA) used in the model. These features are mentioned as its limitations.

To determine $\chi^{(3)}$, the Rentiejs Model refers to Maxwell's equations, which describe wave propagation in a nonlinear, homogeneous, nonmagnetic, and nonconducting medium:

$$\nabla \times \nabla \times \overline{E} + \frac{n^2(3\omega)}{c^2}\frac{\partial^2 \overline{E}}{\partial t^2} = -\frac{4\pi}{c^2}\frac{\partial^2 \overline{P}_{NL}}{\partial t^2} \quad \text{(Eq. 3.15)}$$

The solutions to the above equation are:

$$\overline{E} = \frac{1}{2}\left[E_1 e^{-i(\omega_1 t)\overline{e}_1} + E_3 e^{-i(\omega_3 t)\overline{e}_3} + c.c.\right] \quad \text{(Eq. 3.16)}$$

$$\overline{P}^{NL} = \frac{1}{2}\left[P_1^{NL} e^{i(k_1 z - \omega_1 t)\overline{e}_1} + P_3^{NL} e^{i(k_3 z - \omega_3 t)\overline{e}_3} + c.c.\right] \quad \text{(Eq. 3.17)}$$

By making the substitution $E_i = A_{i\omega} e^{ik_{i\omega} z}$, Eq. 3.16 looks as follows:

$$\overline{E} = \frac{1}{2}\left[A_\omega e^{i(k_1 z - \omega_1 t)\overline{e}_1} + A_{3\omega} e^{i(k_3 z - \omega_3 t)\overline{e}_3} + c.c.\right] \quad \text{(Eq. 3.18)}$$

where:

A_ω , $A_{3\omega}$ – field amplitude of the fundamental wave and THG, respectively.

If the fields under consideration propagate along the *z*-direction, then:

$$\frac{\partial^2 \overline{E}}{\partial z^2} = \frac{1}{2}\frac{\partial^2}{\partial z^2}\left[A_\omega e^{i(k_1 z - \omega_1 t)\overline{e}_1} + A_{3\omega} e^{i(k_3 z - \omega_3 t)\overline{e}_3} + c.c.\right] \quad \text{(Eq. 3.19)}$$

$$\begin{aligned}\frac{\partial^2 \overline{E}}{\partial z^2} = {} & \nabla^2 A_\omega + ik_\omega \frac{\partial A_\omega}{\partial z} e^{i(k_1 z - \omega_1 t)} - \frac{1}{2} A_\omega k_\omega^2 e^{i(k_1 z - \omega_1 t)} \\ & + \nabla^2 A_{3\omega} + ik_\omega \frac{\partial A_{3\omega}}{\partial z} e^{i(k_3 z - \omega_3 t)} \\ & - \frac{1}{2} A_{3\omega} k_{3\omega}^2 e^{i(k_3 z - \omega_3 t)} + c.c.\end{aligned} \quad \text{(Eq. 3.20)}$$

and:

$$\frac{n^2\,(3\omega)}{c^2}\frac{\partial^2\,\overline{E}}{\partial z^2} = \frac{1}{2}\frac{n^2\,(3\omega)}{c^2}\frac{\partial^2}{\partial t^2}\Big[A_\omega\, e^{i(k_1\,z\,-\,\omega_1\,t)\overline{e}_1} + A_{3\omega}\, e^{i(k_3\,z\,-\,\omega_3\,t)\overline{e}_3} + c.c.\Big] = \frac{1}{2}\frac{n^2\,(3\omega)}{c^2}\Big[A_\omega\,\omega_1^2\, e^{i(k_\omega\,z\,-\omega_1\,t)} + A_{3\omega}\,\omega_3^2\, e^{i(k_3\,z-\,\omega_3\,t)}\Big] \quad \text{(Eq. 3.21)}$$

Since $k = \frac{n\omega}{c}$, Eq. 3.21 can be written in the form:

$$\frac{n^2\,(3\omega)}{c^2}\,\frac{\partial^2\,\overline{E}}{\partial z^2} = \frac{1}{2}A_\omega\,k_\omega^2\,e^{i(k_1\,z\,-\,\omega_1\,t)} + \frac{1}{2}A_{3\omega}\,k_{3\omega}^2\,e^{i(k_{3\omega}\,z\,-\,\omega_3\,t)} + c.c. \quad \text{(Eq. 3.22)}$$

Due to SVEA, the left-hand side of Eq. 3.15 can be expressed in terms of Eq. 3.20 and Eq. 3.22 as follows:

$$\frac{\partial^2\,\overline{E}}{\partial z^2} + \frac{n^2\,(3\omega)}{c^2}\,\frac{\partial^2\,\overline{E}}{\partial z^2} = ik_\omega\,\frac{\partial A_{3\omega}}{\partial z}e^{i(k_1\,z\,-\,\omega_1\,t)\overline{e}_1} + ik_{3\omega}\,\frac{\partial A_\omega}{\partial z}e^{i(k_3\,z\,-\,\omega_3\,t)\overline{e}_3} + c.c. \quad \text{(Eq. 3.23)}$$

and also:

$$-\frac{4\pi}{c^2}\frac{\partial^2\,\overline{P}^{NL}}{\partial t^2} = -\frac{1}{2}\frac{4\pi}{c^2}\frac{\partial^2}{\partial t^2}\Big[P_{NL}^{(1)}\,e^{(-i\omega_1\,t)\overline{e}_1} + P_{NL}^{(3)}\,e^{(-i\omega_3\,t)\overline{e}_3} + c.c.\Big] \quad \text{(Eq. 3.24)}$$

By comparing Eq. 3.17 and Eq. 3.23, we can write:

$$\begin{cases} 2ik_{\omega}\dfrac{\partial A_{\omega}}{\partial z} = -\dfrac{4\pi}{c^2}\omega_1^2\dfrac{\partial^2 P_{NL}^{(1)}}{\partial t^2} \\ 2ik_{3\omega}\dfrac{\partial A_{3\omega}}{\partial z} = -\dfrac{4\pi}{c^2}\omega_3^2\dfrac{\partial^2 P_{NL}^{(3)}}{\partial t^2} \end{cases} \quad \text{(Eq. 3.25)}$$

The nonlinear polarization for THG takes the form:

$$P_{NL} = \frac{1}{4}\chi^{(3)} A_{\omega}^3 \left(e^{ik_{\omega} z}\right)^3 \quad \text{(Eq. 3.26)}$$

Based on Eq. 3.25 and Eq. 3.26, we can write:

$$\begin{aligned} 2ik_{3\omega}\frac{\partial A_{3\omega}}{\partial z} &= -\frac{4\pi}{c^2}\omega_3^2\frac{\partial^2}{\partial t^2}\left[\frac{1}{4}\chi^{(3)} A_{\omega}^3 e^{3ik_{\omega} z}\right] e^{-ik_{3\omega} z} \\ &= -\frac{\pi}{c^2}\omega_3^2\,\chi^{(3)} A_{\omega}^3 e^{-i(k_{3\omega}-3k_{\omega})z} \end{aligned} \quad \text{(Eq. 3.27)}$$

which leads to the expression:

$$\frac{\partial A_{3\omega}}{\partial z} = i\frac{\pi}{2c^2}\frac{\omega_3^2}{k_{3\omega}}\chi^{(3)} A_{\omega}^3 e^{-i\Delta k z} \quad \text{(Eq. 3.28)}$$

Knowing that $\frac{\omega^2}{k} = \frac{\omega^2 c}{n\omega} = \frac{2\pi c^2}{\lambda}$, Eq. 3.28 can be written in the form:

$$\frac{\partial A_{3\omega}}{\partial z} = i\frac{\pi^2}{\lambda_{3\omega} n_{3\omega}}\chi^{(3)} A_{\omega}^3 e^{-i\Delta k z} = i\frac{3\pi^2}{\lambda_{\omega} n_{3\omega}}\chi^{(3)} A_{\omega}^3 e^{-i\Delta k z} \quad \text{(Eq. 3.29)}$$

Δk – phase shift vector for THG.

The amplitude of the harmonic field is obtained by integrating Eq. 3.29 over the range 0 to L .

$$A_{3\omega} = \int_0^L i\frac{3\pi^2}{\lambda_\omega\, n_{3\omega}}\chi^{(3)}\, A_\omega^3 e^{-i\Delta kz}\, dz = \frac{3\pi^2}{\lambda_\omega\, n_{3\omega}}\chi^{(3)}\, A_\omega^3\left(\frac{1-e^{-i\Delta kL}}{\Delta k}\right) \quad \text{(Eq. 3.30)}$$

The relationship between the amplitude and optical intensity of the THG signal is as follows:

$$I_{i\omega} = \frac{n_{i\omega}\, c}{2\pi}|A_{i\omega}|^2 \quad \text{(Eq. 3.31)}$$

On this basis, Eq.3.30 can be written in the following form:

$$I_{3\omega} = \frac{n_{3\omega}\, c}{2\pi}\left(\frac{3\pi^2}{\lambda_\omega\, n_{3\omega}}\right)^2 \frac{2\pi}{n_\omega\, c} I_\omega^3 \left|\chi^{(3)}\right|^2 \left|\frac{1-e^{-i\Delta kL}}{\Delta k}\right|^2 \quad \text{(Eq. 3.32)}$$

$$I_{3\omega} = \frac{576\pi^6}{\lambda_{3\omega}\, n_\omega^3\, \lambda_\omega^2 c^2} I_\omega^3 \left|\chi^{(3)}\right|^2 L^2 \left|\frac{\sin\left(\frac{\Delta kL}{2}\right)}{\frac{\Delta kL}{2}}\right|^2 \quad \text{(Eq. 3.33)}$$

I_ω – optical intensity of the fundamental wave,

$I_{3\omega}$ – THG optical intensity,

$\left|\chi^{(3)}\right|$ – electronic input module for $\chi^{(3)}$ of the tested sample.

3.8. Corona Poling

Corona Poling (CP) is a technique by which centrosymmetric materials are made temporally, macroscopically non-centrosymmetric, which, as mentioned earlier, is a necessary condition for generating second-order nonlinear effects [28,29]. This is achieved by applying high voltage and temperature, which changes the orientation of molecules with a dipole moment, which align along the lines of an applied external field $\overline{E}$.

The CP method consists of heating the material to the glass transition temperature to enable the change of molecular orientation. Then, a high voltage of about 4-8 kV is applied. This way, the electric field accelerates free electrons, which ionize the surroundings. Thus, the ions formed create an internal electric field towards the material's surface. Then the sample is slowly cooled to room temperature, and the high voltage applied from the outside is turned off. After cooling and turning off the voltage, the molecular orientation remains preserved for some time. How long the material will maintain the molecular orientation depends on its chemical properties. The schematic of the CP technique is shown in Figure 3.10, while the dipole moments' orientation changes are illustrated in Figure 3.11.

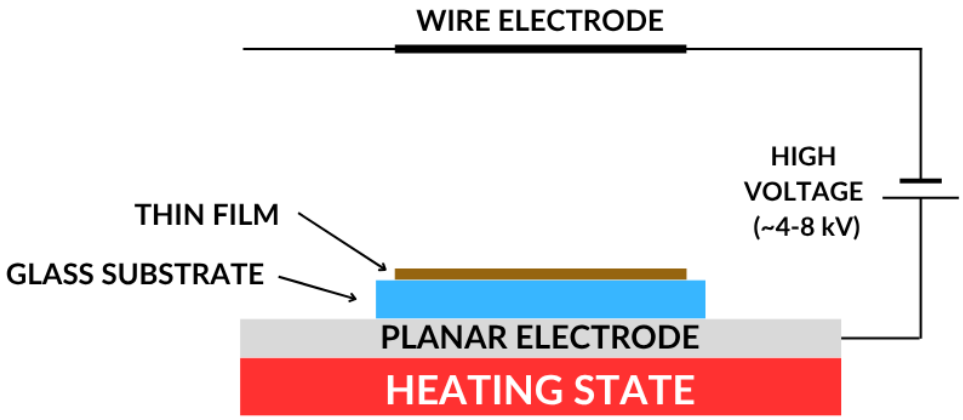

Figure 3.10. Experimental setup of the Corona Poling technique.

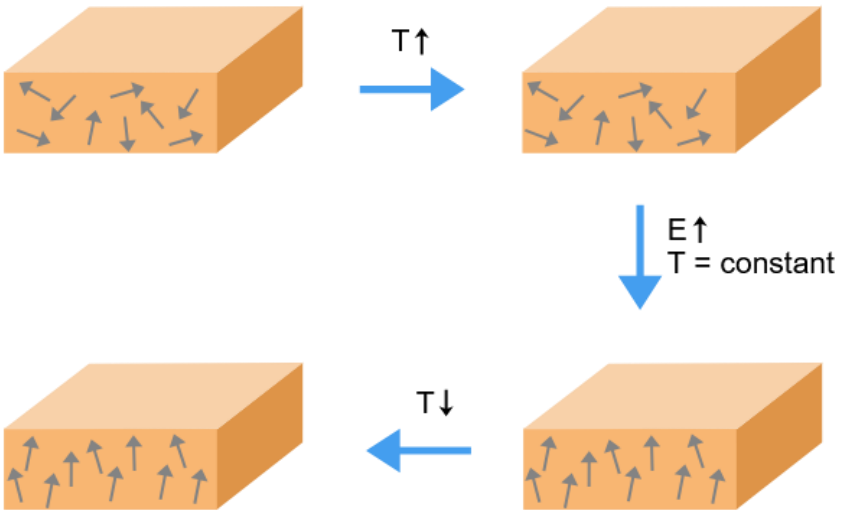

Figure 3.11. Changes in the orientation of dipole moments during Corona Poling; T - Temperature, E - Electric field.

The CP method allows for obtaining macroscopic non-centrosymmetry and is used for thin films and polymers. Its advantages include that it is easy to use, fast, and does not mechanically destroy the sample because there is no direct contact between the electrode and the sample. The disadvantage of the technique is that the forced orientation of the dipole moments lasts only for a specific time and requires monitoring of the absorption spectrum to determine the dipole relaxation time. Despite these disadvantages, CP is often used in optoelectronics and to generate second-order nonlinear effects.

3.9. Z-scan technique

The Z-scan measurement technique is an experimental technique for measuring the third-order nonlinear optical properties of materials, such as the nonlinear refractive index n_2, the nonlinear absorption coefficient β, and thus the real and imaginary parts of $\chi^{(3)}$. The most commonly studied materials are liquids, but thin films and crystals can also be studied with Z-scan. The method was described in 1989 by M. Sheik-Bahae and his research group [30,31]. It finds applications in the characterization of nonlinear photonics materials, third-order nonlinear optics, molecular structure studies, and diagnostics of biological and biomedical materials.

The measurement technique involves moving a thin material sample along the laser beam's propagation axis, i.e., the z-axis. Before the laser beam hits the sample, a converging lens focuses it, and the material sample is placed near the lens focal point and scanned both in front of the focus ($z < 0$), at the focus ($z = 0$), and behind the focus ($z > 0$). During the measurement, changes in the intensity of light transmitted by the sample and the subsequent slit located in the far field are recorded. Observation of these changes leads to the determination of nonlinear parameters of the tested material. The Z-scan setup is shown in Figure 3.12. In the presented system, the source of laser pulses is an Nd:YAG laser with a wavelength of 532 nm, a pulse duration of 30 ps, and a processing frequency of 10 Hz. The laser beam initially hits the beam splitter, which transmits part of the radiation towards the sample and directs part to the photodiode. In this configuration, the photodiode plays the role of synchronization and trigger. Laser radiation directed towards the sample passes through subsequent optical elements such as a polarizer, a half-wave plate, and a focusing lens, then hits the sample. Depending on the system's configuration, the light transmitted by the sample can hit one of two photomultipliers (PMT1 or PMT2). Depending on the system's configuration, we talk about a Z-scan system with an open shutter (PMT1) or a system with a closed shutter (PMT2). In the first version, a measurement is performed to determine the nonlinear absorption coefficient β. In the second version, a measurement is performed to determine the nonlinear refractive index n_2. To determine $\chi^{(3)}$, Z-scan measurements must be performed in both configurations, because the imaginary part of $\chi^{(3)}$ is related to the β coefficient and the real part to the n_2 coefficient.

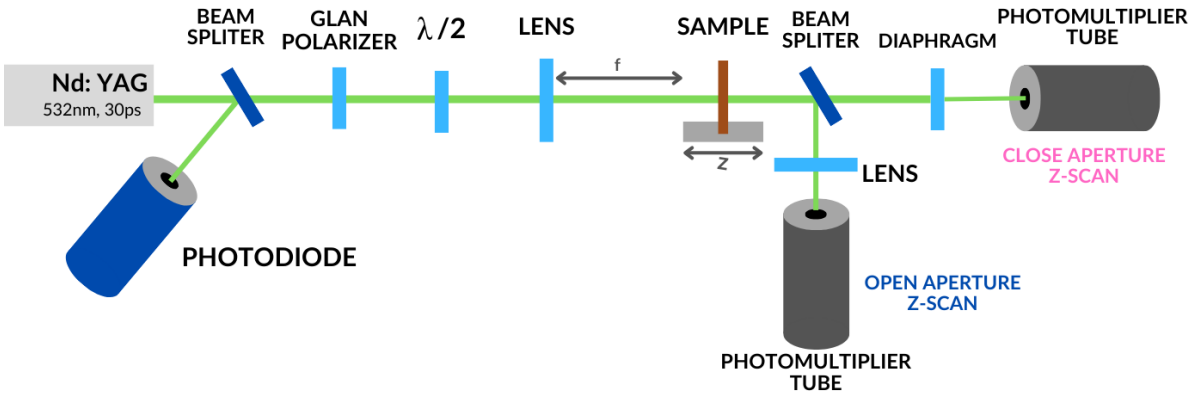

Figure 3.12. Diagram of the Z-scan measurement system.

The advantages of the Z-scan measurement technique include the possibility of simultaneous measurement of the β and n_2 coefficients, a simple experimental setup with one laser beam, and high measurement sensitivity that allows detection of even very weak nonlinear effects. This technique also has some limitations, such as the requirement for a high-quality Gaussian beam, accurate calibration and positioning of the sample, and the possibility of measurement interference due to thermal effects occurring during the measurement.

3.9.1. Open aperture Z-scan

Information related to the β coefficient is obtained in the open Z-scan configuration. In this case, the material used to calibrate the system is fullerene (C_{60}). The pulsed light source focuses many photons on the tested material, which supports nonlinear optical effects and enhances photon absorption. The measurement results in one of two possible transmission curves (Figure 3.13). Depending on the type of material behavior, RSA (Figure 3.13a) or SA (Figure 3.13b) is observed. In the first case, reduced transmission at the focal point is clearly visible, while in the second case, increased transmission is clearly visible.

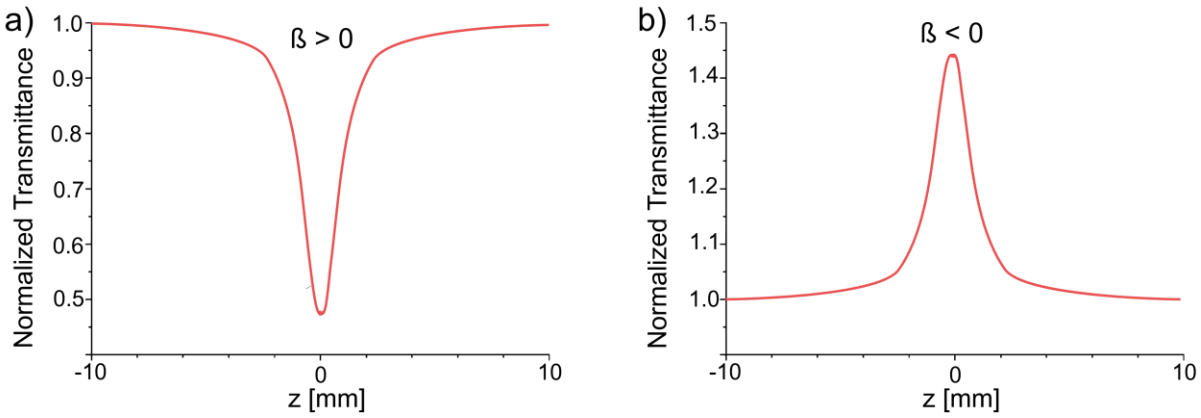

Figure 3.13. Normalized nonlinear transmission curves obtained using the Z-scan technique in an open configuration: $\beta > 0$ (a); $\beta < 0$ (b).

The normalized transmission of the system along the *z-axis* is described by Eq. 3.34:

$$T(z, S = 1) = \frac{1}{\sqrt{\pi} q_0 (z, 0)} \int_{-\infty}^{+\infty} \ln\left[1 + q_0 (z, 0) e^{-\mu^2}\right] d\mu \qquad \text{(Eq. 3.34)}$$

where:

$$q_0 = (z, 0) = \frac{\beta I_0 L_{eff}}{1 + \left(\frac{z}{z_0}\right)^2} \quad \text{(Eq. 3.35)}$$

I_0 – intensity at the center of the beam,

z_0 – Rayleigh range,

L_{eff} – effective sample thickness.

Based on the determined β coefficient, the imaginary part of $\chi^{(3)}$ can be calculated using the equation:

$$Im\left(\chi^{(3)}\right) = \frac{n_0^2 \varepsilon_0 c\lambda}{3\pi}\beta \quad \text{(Eq. 3.36)}$$

where:

n_0 – linear refractive index,

c – speed of light.

3.9.2. Close aperture Z-scan

In the closed Z-scan configuration, the radiation beam passing through the sample reaches the shutter and then goes to the PMT2 photomultiplier. The shutter's task is to limit the measurement to a specific part of the light. By measuring this Z-scan configuration, information related to the n_2 coefficient is obtained. The measurement result is one of two normalized transmission curves (Figure 3.14). Based on them, the sign of the n_2 coefficient is determined. When the normalized curve has a "valley-peak" shape, the tested material behaves like a converging lens, and then $n_2 > 0$ (self-focusing). When the situation is reversed and the shape of the curve can be described as "peak-valley", the medium behaves like a diverging lens and $n_2 < 0$ (negative self-focusing).

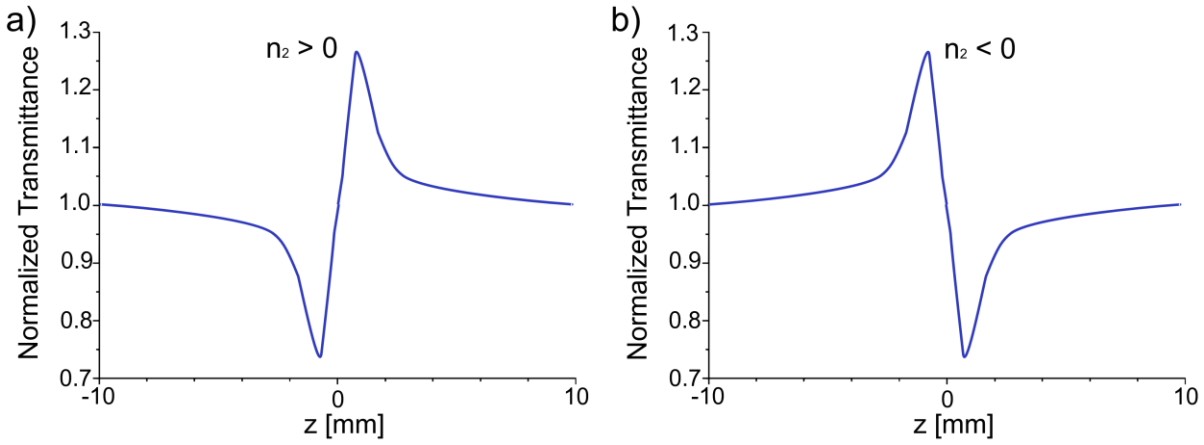

Figure 3.14. Normalized nonlinear transmission curves obtained using the Z-scan technique in a closed configuration: $n_2 > 0$ (a); $n_2 < 0$ (b).

From the normalized transmissions, the peak-to-valley difference (ΔT_{P-V}) is determined, which is proportional to the nonlinear phase shift $\Delta\phi_0$.

$$\Delta T_{P-V} = 0.406 \frac{\Delta\phi_0}{\sqrt{2}} (1 - S)^{0.25} \qquad \text{(Eq. 3.37)}$$

S – power transmission through the aperture

S for Gaussian beam:

$$S = 1 - \exp\left(-\frac{2r_a^2}{w_a^2}\right) \qquad \text{(Eq. 3.38)}$$

r_a – aperture radius,

w_a – radius of the beam intensity in the aperture plane.

The sensitivity of the Z-scan measurement in a closed configuration is indicated by the parameter S. When the aperture diameter is much smaller than the beam diameter ($S \ll 1$), the sensitivity is maximum and equal to 0.406. When the aperture diameter is larger than the beam diameter ($S = 1$), the Z-scan loses sensitivity to nonlinear refraction of light, corresponding to the Z-scan measurement in an open configuration.

The maximum value of the nonlinear phase shift can be expressed by the formula:

$$\Delta\phi_0 = k\Delta n_0 L_{eff} \quad \text{(Eq. 3.39)}$$

where:

k – wave vector of the radiation source,

Δn_0 – change in the refractive index along the optical axis, at the focus,

L_{eff} – effective sample thickness.

Δn_0 is expressed as:

$$\Delta n_0 = \gamma' I_0 \quad \text{(Eq. 3.40)}$$

where:

γ' – nonlinear refraction parameter.

$$\gamma' = \frac{n_2}{2}|E|^2 \quad \text{(Eq. 3.41)}$$

$$I_0 = \frac{2E}{\pi w_0^2 \tau} \quad \text{(Eq. 3.42)}$$

E – laser pulse energy

τ – pulse duration

Inserting Eq. 3.39 and Eq. 3.40 into Eq. 3.37 gives:

$$\Delta T_{P-V} = 0.406 \frac{\gamma' I_0 L_{eff}}{\sqrt{2}} (1 - S)^{0.25} \quad \text{(Eq. 3.43)}$$

Based on the above considerations, $Re(\chi^{(3)})$ can be determined:

$$Re(\chi^{(3)}) = \frac{4n_0^2\varepsilon_0 c}{3} n_2 \quad \text{(Eq. 3.44)}$$

3.9.3. Divided Z-scan

Due to the possibility of interaction between nonlinear refraction and nonlinear absorption, which can affect the results obtained in a closed configuration, the divided Z-scan method is used. At first glance, the divided Z-scan method is the same as the close Z-scan method. However, it should be emphasized that the divided Z-scan considers the effect of nonlinear absorption by dividing the data obtained for the closed configuration by the data obtained for the open configuration [32]. If nonlinear absorption occurs, part of the beam is absorbed, and the intensity of the transmitted beam decreases relative to the original beam. In the absence of nonlinear absorption, the intensity of the transmitted beam does not change, and therefore the result remains unchanged.

3.10. Electrical and photovoltaic properties measurements

Due to the potential application of the thin perovskite layers in optoelectronics, electrical properties were measured using the equipment, the diagram of which is presented in Figure 3.15 [33]. The measurement system includes the KEITHLEY 4200-scs system, which is equipped with three SMU (Source Measurement Unit) units. The SMU units enable the analysis of the electrical parameters of the structures studied. They can operate as voltage or current sources (depending on the selected function). The software allows for limiting the voltage or current to a preset value, providing voltage (V-limit) and current (I-limit) protection. During the tests, the SMU unit operates as a voltage source. It supplies power to the tested thin film structure, while simultaneously measuring the current flowing in the circuit. The KEITHLEY 4200-scs system has two pairs of wires – FORCE and SENSE. The FORCE pair of wires was used during the measurements, and the SENSE wires were shorted to ground. To collect the current-voltage characteristics I-V of the photovoltaic cells, two gold measuring probes were connected to the structure using micromanipulators. The parameters characterizing the perovskite thin films and photovoltaic

cells were determined based on the collected I-V characteristics. To research the effect of lighting on electrical parameters, the LCS-100 (Oriel) sunlight simulator is included in the system (Figure 3.15). The simulator is dedicated to research that requires the operation of a certified system in a small, well-lit area. It evenly illuminates surfaces measuring 38 mm x 38 mm and meets the requirements of the ABB class according to ASTM and IEC standards. Thin film samples were connected to the measurement system using gold contacts 150 nm thick, 1.5 mm wide, spaced 5 mm apart, and made using the PVD technique.

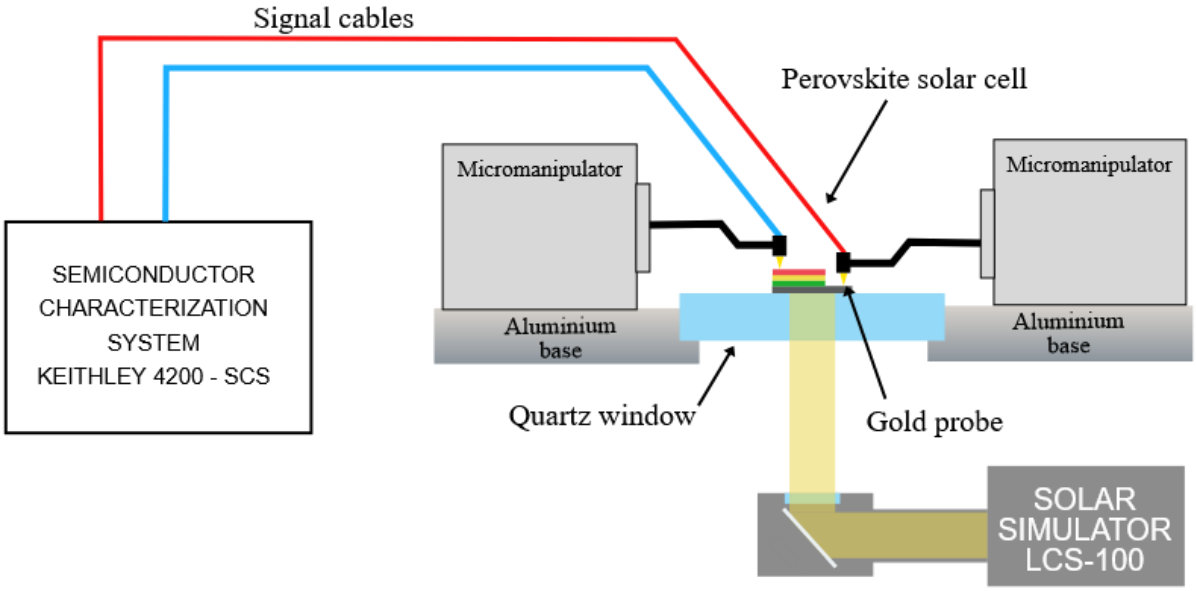

Figure 3.15. Schematic diagram of the measurement setup for testing the electrical properties of thin films and thin film solar cells under illuminated and dark conditions.

References

1. A. Laouid *et al.* Optical and morphological properties of DCM thin films co-doped of Znq2 by PVD: Theoretical and experimental investigations. *Vacuum* (2024) 222, 112997, https://doi.org/10.1016/j.vacuum.2024.112997
2. M. Vorobyova *et al.* PVD for Decorative Applications: A Review. *Materials* (2023) 16(14), 4919, https://doi.org/10.3390/ma16144919
3. A. Lakhtakia and R. Messier, Sculptured Thin Films: Nanoengineered Morphology and Optics, History of Thin-Film Morphology. *Optik* (2005) 117(12):580-580, SPIE Press, DOI: 10.1016/j.ijleo.2006.03.008
4. K. D. Bouzakis and N. Michailidis, Physical Vapor Deposition (PVD). *Springer* (2019) 1308-1316, CIRP Encyclopedia of Production Engineering, https://doi.org/10.1007/978-3-662-53120-4_6489
5. H. Ichou *et al.* Exploring the Advancements in Physical Vapor Deposition Coating: A Review. *JBTC* (2024) 10:3, https://doi.org/10.1007/s40735-023-00806-0
6. A. Baptista *et al.* On the Physical Vapour Deposition (PVD): Evolution of Magnetron Sputtering Processes for Industrial Applications. *Procedia Manufacturing* (2018) 17, 746-757, https://doi.org/10.1016/j.promfg.2018.10.125
7. A. Baptista *et al.* Sputtering Physical Vapour Deposition (PVD) Coatings: A Critical Review on Process Improvement and Market Trend Demands. *Coatings* 2018, 8, 402. https://doi.org/10.3390/coatings8110402
8. G. Binnig *et al.* Atomic Force Microscope. *Phys. Rev. Lett.* (1986) 56, 930. DOI: https://doi.org/10.1103/PhysRevLett.56.930
9. W.R. Bowen and N. Hilal, Atomic Force Microscopy in Process Engineering. *Elsevier* (2009)
10. K. Sumetpipat *et al.* Mathematical methods on atomic force microscope cantilever systems. *RSC Adv.* (2016) 6, 46658-46667, https://doi.org/10.1039/C6RA02126C
11. A. Marjanowska *et al.* Role of Composition and Temperature in Shaping the Structural and Optical Properties of Iodide-Based Hybrid Perovskite Thin Films Produced by PVco-D Technique. *Materials* (2025) 18(6), 1336, https://doi.org/10.3390/ma18061336

12. M. Salerno and M. Banzato, Minkowski Measures for Image Analysis in Scanning Probe Microscopy. *Microscopy and Analysis* (2005) 19(4): 13-15
13. K.N. Shinde *et al.* Basic Mechanisms of Photoluminescence. In: Phosphate Phosphors for Solid-State Lighting. *Springer Series in Materials Science* (2012) vol 174, https://doi.org/10.1007/978-3-642-34312-4_2
14. J.M.S. Lopes *et al.* An Introduction to Steady-State and Time-Resolved Photoluminescence. *Springer Handbook of Inorganic Photochemistry* (2022) https://doi.org/10.1007/978-3-030-63713-2_6
15. M. Nur-E-Alam *et al.* Current scenario and future trends on stability issues of perovskite solar cells: A mini review. *Current Opinion in Colloid & Interface Science* (2025) 76, 101895, https://doi.org/10.1016/j.cocis.2025.101895
16. S. Sandhu eand N.G. Park, Methodologies to Improve the Stability of High-Efficiency Perovskite Solar Cells. *Acc. Mater. Res.* (2024) 5, 12, 1544–1557, https://doi.org/10.1021/accountsmr.4c00237
17. A. Tarbi *et al.* Diagnostics of the stability of CsPbX3 (X = Cl, Br, and I) inorganic halide perovskites for photovoltaic applications: An in-depth review with an original contribution on impedance characterization. *Renew. Sust. Energ. Rev.* (2026) 226, 116234. https://doi.org/10.1016/j.rser.2025.116234
18. A. Marjanowska *et al.* Argon Environment Influence on Perovskite Thin Film Durability. *IEEE,* 24th International Conference on Transparent Optical Networks (ICTON) (2024) 10.1109/ICTON62926.2024.10647284
19. B. Kulyk *et al.* Optimization and diagnostic of nonlinear optical features of π-conjugated benzodifuran-based derivatives. *RSC Adv.* (2016) 6, 14439-14447, https://doi.org/10.1039/C5RA25889H
20. C. Razzetti *et al.* Maker fringes as a tool for the orientation of noncentrosymmetric specimens. *Mater. Chem. Phys.* (2000) 66, 2–3, 309-315, https://doi.org/10.1016/S0254-0584(00)00307-2
21. A. Aghigh *et al.* Second harmonic generation microscopy: a powerful tool for bio-imaging. *Biophys Rev* (2023) 15, 43–70, https://doi.org/10.1007/s12551-022-01041-6

22. F. Kajzar *et al.* Second- and third-order non-linear optical properties of multilayered structures and composites of C60 with electron donors. *Synthetic Metals* (2001) 117, (1), 189–193, https://doi.org/10.1016/S0379-6779(00)00498-7
23. P.A. Franken *et al.* Generation of Optical Harmonics. *Phys. Rev. Lett.* (1961) 7, (4), 118–119, https://doi.org/10.1103/PhysRevLett.7.118
24. S.K. Kurtz and T.T. Perry, A Powder Technique for the Evaluation of Nonlinear Optical Materials. *J. Appl. Phys.* (1968) 39, 3798–3813, https://doi.org/10.1063/1.1656857
25. W.N. Herman and L.M. Hayden, Maker fringes revisited: second-harmonic generation from birefringent or absorbing materials. *J. Opt. Soc. Am. B* (1995) 12, 3, 416-427, https://doi.org/10.1364/JOSAB.12.000416
26. K. Kubodera and H. Kobayashi, Determination of Third-Order Nonlinear Optical Susceptibilities for Organic Materials by Third-Harmonic Generation. *Mol. Cryst. Liq. Cryst. Incorporating Nonlinear Opt.* (1990) 182, (1), 103–113, https://doi.org/10.1080/00268949008047792
27. J. Reintjes, Nonlinear Optical Parametric Processes in Liquids and Gases. *Elsevier* (2012)
28. G. Sico *et al.* Corona Poling Enabling Gravure Printing of Electroactive Flexible PVDF-TrFE Devices. *Materials* (2025) 18(1), 22, https://doi.org/10.3390/ma18010022
29. A. Hill *et al.* Corona poling of nonlinear polymer thin films for electro-optic modulators. *Appl. Phys. Lett.* (1994) 65, 1733–1735, https://doi.org/10.1063/1.112899
30. A.A. Said *et al.* Z-scan: a simple sensitive technique for measuring refractive nonlinearities. *Conference on Lasers and Electro-Optics (CLEO)* (1989) https://doi.org/10.1364/OAM.1989.TUY3
31. M. Sheik-Bahae *et al.* Sensitive Measurement of Optical Nonlinearities Using a Single Beam. *IEEE J. Quantum Electron.* (1990) 26(4):760 – 769, DOI: 10.1109/3.53394
32. S. Zongo *et al.* Nonlinear optical properties of natural laccaic acid dye studied using Z-scan technique. *Opt. Mater.* (2015) 46, 270–275, https://doi.org/10.1016/j.optmat.2015.04.031
33. A. Zawadzka *et al.* Low-temperature influence on the properties and efficiency of thin-film perovskite solar cells fabricated by the PVco-D technique. *Sol. Energy Mater. Sol. Cells* (2024) 274, 112993, https://doi.org/10.1016/j.solmat.2024.112993

CHAPTER 4: CHARACTERIZATION OF PEROVSKITE THIN FILMS

The fourth chapter presents the investigated perovskite materials, the procedures used for sample preparation, and the results of structural, optical, and photovoltaic characterizations. The materials analyzed were thin films of hybrid perovskites. Their common denominator is their structure - each consists of an organic part - the methylammonium part, and an inorganic part - in the form of iodide, chloride, or bromide. The selection of specific perovskites was made based on optoelectronic potential, applicability, and scientific popularity. Many of the perovskites discovered to date are not sufficiently well understood to be successfully used in optoelectronic devices. Although perovskites have great optoelectronic potential and are among the most promising materials for producing the next-generation photovoltaic cells, the lack of knowledge of their fundamental physicochemical properties has slowed the commercialization of perovskite devices. The research aimed to develop a technique for obtaining perovskite thin film structures with different chemical compositions and variable percentages of their organic and inorganic components, to investigate how they affect the fundamental optical and structural properties, and to explore the applicability of perovskites in nonlinear optics and photovoltaics. At the same time, all the aforementioned research objectives deepen the knowledge of the fundamental properties of perovskites, which, in a broader perspective, is expected to help accelerate the pace associated with the development and commercialization of optoelectronic perovskite devices. In this chapter, the results of perovskite thin film research on:

- surface structure,
- transmission spectra,
- the influence of the environment on the surface structure and transmission spectra (aging tests),
- phase transitions,
- nonlinear optical effects THG, SHG and Z-scan,
- electrical properties on the basis of I-V characteristics,
- applications in the structure of a photovoltaic cell,

- the effect of perovskite composition on structural, optical and photovoltaic properties.

4.1. Perovskites

Perovskites were discovered in the second half of the 19th century, but it was not until the 1950s that they began to attract more interest from the scientific community [1]. This was due to scientists in New York, who then applied oxide perovskites for the first time in electrochemical converters and capacitors. In time, a method for the chemical synthesis of perovskites was developed, which opened up new research opportunities. In the 1970s, D. Weber discovered the first hybrid halide perovskite [2]. The unique physico-chemical properties of this type of material, such as its strong absorption of electromagnetic radiation, led to perovskites being used in optoelectronics. The result was the creation of the first light-emitting device by IBM. This discovery accelerated the development of research on hybrid perovskites and initiated the search for their new applications. Certainly, one of the most groundbreaking moments in perovskite technology was using a perovskite thin film as the active layer in a photovoltaic cell. This was done by a group of Japanese researchers in 2009 [3]. The photovoltaic cell they developed achieved an efficiency of 3.8%. Since then, research into thin film perovskite cells has increased their efficiency. They currently achieve efficiencies close to 34%, making them a serious competitor to, by far, the most popular silicon cells [4].

Using perovskite materials in photovoltaics is only the beginning of their application possibilities. A few years ago, they were shown to be used in the field of nonlinear optics [5]. They were investigated to manifest nonlinear optical responses such as saturated absorption, two- or multiphoton absorption, Third Harmonic Generation, or nonlinear refraction. In addition to nonlinear optics, perovskites have potential for lasers, light-emitting diodes, photodetectors, optical switches, and high-resolution imaging applications. Confirmation of the development of work on perovskites can be found in a steadily increasing number of scientific publications. Nevertheless, in-depth research into their fundamental photophysical properties is still needed.

The first classified perovskite was $CaTiO_3$. This mineral was discovered in the Ural Mountains by G. Rose and took its name from the Russian mineralogist L. Perovsky.

There turned out to be more materials having a similar crystal structure to $CaTiO_3$. Hence, perovskites came to refer to a group of materials with a specific crystal lattice - similar to that of $CaTiO_3$. Perovskites are described by the general formula ABX_3. The A atom is usually a cation of a metal from the first or second group of the periodic table of elements or a cation of a transition metal. The site of the B element may be a cation with a coordination number of 6, and an oxide, sulphide, or halide anion may occupy the X site. The ideal crystal lattice of a perovskite material is shown in Figure 4.1. It consists of evenly spaced octahedra with an A element in between, balancing the charge of the crystal lattice. The tops of the octahedra are X anions, and inside them is a B cation. The crystal structure of perovskite is unstable and can change with temperature changes. Hence, perovskite materials can exist in three crystallographic phases - tetragonal, orthorhombic, and cubic (Figure 4.2). Adopting a particular phase by a perovskite is primarily determined by its chemical composition and temperature. Whitfield *et al.* [6] assumed that perovskites adopt a tetragonal phase at room temperature, an orthorhombic phase at temperatures below room temperature, and a cubic phase at temperatures above room temperature. In fact, the phase transition temperature of a perovskite is greatly influenced by its chemical composition, and the transition temperatures can vary greatly.

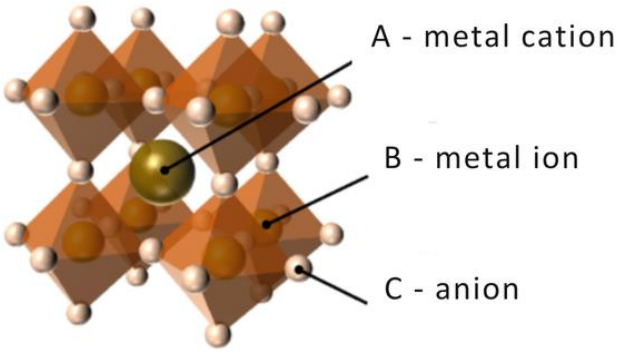

Figure 4.1. The ideal crystal structure of the perovskite material ABX_3.

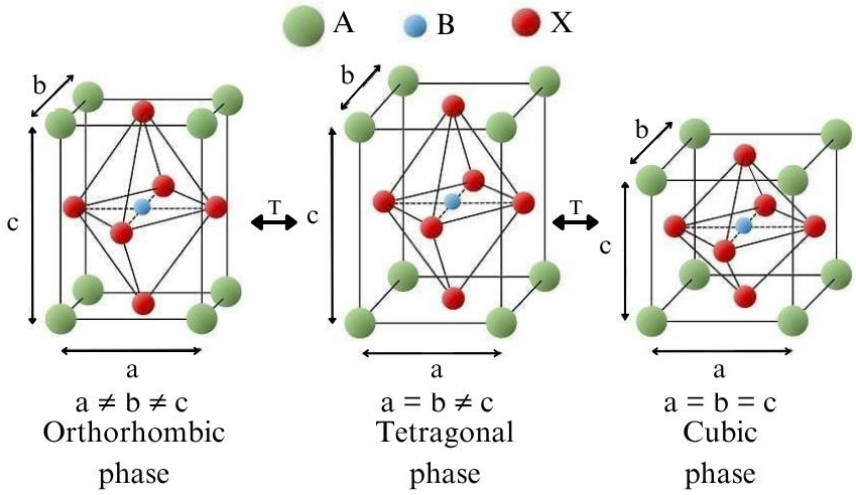

Figure 4.2. Crystalline structures that perovskite can adopt due to phase transitions; T - Temperature.

The stability of the perovskite crystal structure, i.e., the deviation from the ideal structure, is determined by the tolerance factor t_{tol}:

$$t_{tol} = \frac{r_A + r_X}{\sqrt{2}(r_B + r_X)} \qquad \text{(Eq. 4.1)}$$

r_A, r_B, r_X - ion radii A, B, X.

When perovskite occurs in the cubic phase, the condition $0.9 < t_{tol} < 1$ is met. In the situation of a distortion of the ideal structure $0.8 < t_{tol} < 0.9$ and for $t_{tol} < 0.8$ and $t_{tol} > 1$, one speaks of a non-perovskite structure [7]. Perovskites occur in the environment and can also be obtained by chemical synthesis. With chemical synthesis, it is possible to select the A, B, and X elements, by which the perovskite's structural, electrical, and optical properties can be influenced to some extent. The characteristic properties of perovskites that make them of great interest in the field of optoelectronics are the possibility of structural modification, strong light absorption, high hole and electron mobility, the possibility of light emission, nonlinear effects, low thermal conductivity, the possibility of ferromagnetism and superconductivity, and semiconductivity

used in photovoltaic applications [8,9]. One disadvantage of perovskite materials is surface reactivity, which involves degradation in the presence of moisture and oxygen.

This study investigates the structural, optical, electrical, and photovoltaic properties of thin films of selected halide hybrid perovskites. All samples studied consisted of an organic part - the methylammonium part $CH_3\,NH_3^+$ (otherwise MA), and an inorganic part - in the form of iodide (PbI_2), chloride ($PbCl_2$), or bromide ($PbBr_2$). Regarding the general formula describing perovskite ABX_3, the $CH_3\,NH_3^+$ part is the A element - a large organic cation, occupying the space between the octahedra. The Pb_2^+ ions are metallic cations that are B elements and are located in the centre of the octahedra, while I^-, Cl^-, and Br^- are halide anions occupying the X positions. In summary, this monograph presents the results of thin films of the following organic-inorganic halide perovskites:

- $MAPbI_3$,
- $MACdI_3$,
- $MAGeI_3$,
- $MASnI_3$,
- $MAZnI_3$,
- $MAPbCl_3$,
- $MAPbBr_3$,
- $MASnBr_3$.

The above materials were selected based on their application potential, optoelectronic capabilities, the possibility of obtaining them by the PVco-D technique and scientific popularity. $MAPbI_3$ is the most popular of the above perovskites, as evidenced by the number of scientific publications describing this material. The other perovskites are less frequently described in the literature, while their application potential is promising. Research into perovskite materials to date does not provide sufficient knowledge to apply them in everyday life successfully. Therefore, the aim is to learn more about their basic optoelectric and structural properties to successfully apply perovskite thin films in practical optoelectronic solutions.

4.2. Preparation of thin film perovskite samples

All thin film samples investigated in this study were prepared by the PVD technique or its modification, PVco-D, using the Thin Film Deposition System - NANO 36™ apparatus (Kurt J. Lesker Company). Thin films were deposited onto transparent BK7 borosilicate glass substrates with areas of approximately 4 cm^2 and a thickness of 0.5 mm.

Each sample preparation began with substrate preparation. BK7 glass substrates were carefully cleaned of dust, grease, and all other contaminants in three stages - in an acetone bath and an ethanol bath using an ultrasonic cleaner, followed by cleaning in isopropanol vapor. Thin layers of perovskites were applied to the substrates prepared using the PVco-D technique. Each perovskite was formed from two starting materials - an organic methylammonium moiety and an inorganic moiety, being iodide, chloride, or bromide.

$$MAI + PbI_2 \longrightarrow MAPbI_3 \quad \text{(Eq. 4.2)}$$

$$MAI + CdI_2 \longrightarrow MACdI_3 \quad \text{(Eq. 4.3)}$$

$$MAI + GeI_2 \longrightarrow MAGeI_3 \quad \text{(Eq. 4.4)}$$

$$MAI + SnI_2 \longrightarrow MASnI_3 \quad \text{(Eq. 4.5)}$$

$$MAI + ZnI_2 \longrightarrow MAZnI_3 \quad \text{(Eq. 4.6)}$$

$$MACl + PbCl_2 \longrightarrow MAPbCl_3 \quad \text{(Eq. 4.7)}$$

$$MABr + PbBr_2 \longrightarrow MAPbBr_3 \quad \text{(Eq. 4.8)}$$

$$MABr + SnBr_2 \longrightarrow MASnBr_3 \quad \text{(Eq. 4.9)}$$

Methylammonium iodide, chloride, and bromide (MAI, MACl, MABr) were obtained by chemical synthesis, while all other iodides, chlorides, and bromides were purchased from Sigma-Aldrich. MAI, MACl, and MABr took the form of fine flakes,

while the other materials were free-flowing. In this form, with no other modifications, they were used to fabricate thin film perovskite structures using PVco-D. The names of the materials used and their melting points are given in Table 4.1.

The tested thin films had different thicknesses, but not exceeding 500 nm (Table 4.2). Due to the ability to control the evaporation rate of the materials in the PVco-D process, the samples formed from the two components had a 50% : 50% composition. In the case of $MAPbI_3$, $MAPbCl_3$ and $MAPbBr_3$ perovskites, two other compositions were made and tested - 70% organic part : 30% inorganic part and 30% organic part : 70% inorganic part. The perovskite samples were tested as soon as possible after receipt and, if necessary, stored in sealed boxes filled with argon in a darkened area. To simplify the description of the samples in the following sections, the notation in Table 4.2, ID column, was applied.

Table 4.1. Materials used to produce perovskites by the PVco-D technique and their melting points.

Material	Melting point [°C]
MAI (own synthesis)	~280
MACl (own synthesis)	~200
MABr (own synthesis)	~230
PbI_2	~400
CdI_2	~350
GeI_2	~170
SnI_2	~320
ZnI_2	~445
$PbCl_2$	~170
$PbBr_2$	~370
$SnBr_2$	~215

Table 4.2. Summary of the hybrid perovskite thin films selected for study obtained by the PVco-D technique and their thicknesses indicated by the vacuum deposition system thickness sensors.

ID	Material	Composition	Thickness [nm]
I.1	$MAPbI_3$	50% MAI : 50% PbI_2	300
I.2	$MAPbI_3$	70% MAI : 30% PbI_2	300
I.3	$MAPbI_3$	30% MAI : 70% PbI_2	300
I.4	$MACdI_3$	50% MAI : 50% CdI_2	170
I.5	$MAGeI_3$	50% MAI : 50% GeI_2	70
I.6	$MASnI_3$	50% MAI : 50% SnI_2	400
I.7	$MAZnI_3$	50% MAI : 50% ZnI_2	260
Cl.1	$MAPbCl_3$	50% $MACl$: 50% $PbCl_2$	300
Cl.2	$MAPbCl_3$	70% $MACl$: 30% $PbCl_2$	300
Cl.3	$MAPbCl_3$	30% $MACl$: 70% $PbCl_2$	300
Br.1	$MAPbBr_3$	50% $MABr$: 50% $PbBr_2$	300
Br.2	$MAPbBr_3$	70% $MABr$: 30% $PbBr_2$	300
Br.3	$MAPbBr_3$	30% $MABr$: 70% $PbBr_2$	300
Br.4	$MASnBr_3$	50% $MABr$: 50% $SnBr_2$	400

4.3. Surface characterization

The surface topographies of all hybrid perovskite thin films have been investigated by contact-mode AFM, which is described in *Chapter 3*, *Section 3.2* Atomic Force Microscopy. The high-resolution AFM images show the topographies of the thin films on 20 μm x 20 μm surfaces in 2D and 3D representations. The results of the analysis of the obtained images describing the characteristic parameters of the thin films, such as the average height of the crystallites, the roughness, and the results of the analysis of the MFs, are provided in the following subsections of this paragraph. An important fact is that AFM studies were performed immediately after the thin films were obtained to minimize the influence of the environment on the film structure. To compare the perovskite films with thin films of their components, the following data set also includes AFM images of the organic (MAI, MACl, MABr) and inorganic (PbI_2, CdI_2, ZnI_2, $PbCl_2$, $PbBr_2$, $SnBr_2$) parts themselves.

4.3.1. Iodide perovskites

Figure 4.3 shows the results of surface topography measurements of perovskite thin films containing iodine I. AFM images of some of the components forming these films are included in Figure 4.4 for comparison with the results obtained for perovskites. Information on the average height of the crystallites and the roughness of the structures is provided in Table 4.3. The results presented here allow a comparison of the different perovskites with iodine - Figure 4.3a-f shows the same perovskite but with a different composition, while the perovskites involved in Figure 4.3g-j differ from the previous ones in their B cation (B = Pb, Cd, Zn). A more detailed analysis is provided by Figure 4.5, which compares layer profiles and Minkowski Functionals.

Analysing the data presented for perovskites with a composition of 50% : 50% (Figure 4.3adghij) due to the type of B cation, the differences in layer structure are evident. The surface of sample I.1 comprises numerous small crystallites, generally no larger than 1 μm in size, varying in height (MSR = 26.34 nm), with single higher and larger crystallites present. In the situation of sample I.4, the surface consists of low, evenly distributed crystallites of slightly larger size and a lower roughness of 12.56 nm. In the situation where Zn is the cation, the surface of the layer consists of high, larger, unevenly distributed crystallites, which increases the roughness of the layer to 35.56 nm. The above statements related to layer roughness are confirmed by the profiles in Figure 4.5a. In addition, analysis of the MFs (Figure 4.5b-d) provides information on the growth pattern and nature of the layers. All layers grew uniformly during the deposition process, as confirmed by the Minkowski Volume (V) function. However, the percolation threshold for the considered samples I.1, I.4, and I.7 is about 22 nm, 6 nm, and 12 nm, respectively, indicating that they have compact structures from the substrate side up to the height of this threshold. The symmetry of the Minkowski Connectivity (χ) diagrams confirms that the structures obtained have a uniform distribution of islands and valleys.

Figure 4.3a-f, which aims to compare the effect of thin film composition on structural properties, provides interesting information. The surface topographies of the samples I.1-I.3 investigated in this range differ considerably. The influence of the sample's composition on its structural properties is evident. Increasing the content of the MAI while decreasing

the content of PbI_2 in the $MAPbI_3$ perovskite thin film results in an increase in the size of the crystallites and a higher average height (Table 4.3 h_{ave}). The surface roughness is slightly lower. When the content of the methylammonium moiety is reduced, the crystallites take the form of pins. In all three cases, the thin films have a uniform distribution of islands and valleys, and the percolation threshold increases with methylammonium content. Comparing the thicknesses of samples I.1-I.3 indicated by the AFM with the values indicated by the vacuum sputtering sensors, there is a clear difference in the thickness of sample I.3. According to the AFM, the highest crystallites of layer I.3 reach a height of 49 nm, while according to the vacuum sputtering sensors, the thickness of this layer was 300 nm. Such a large discrepancy most likely results from the fact that the I.3 perovskite with composition 30% MAI : 70% PbI_2 initially deposited very well in a layer-by-layer manner on the substrate surface. After reaching a thickness of about 200 nm, the deposition mode changed to an island-like growth, leading to the formation of individual crystallites observed in the AFM image.

Comparing the perovskite thin films I.1-I.4 and I.7 with the thin films of the individual components forming them, some correlations can be seen between the nature of the layers, i.e., between the sizes, heights, and distributions of crystallites across the study area. Large crystallites with irregular shapes from the MAI thin layer, while PbI_2 is formed by single, small, unevenly distributed higher crystallites. This is reflected in the surface structure of I.1-I.3, where the composition changes. Higher MAI content results in a perovskite layer with larger structures, while an increase in PbI_2 content results in a perovskite layer composed of pin-shaped crystallites. Similar considerations apply to sample I.4.
In the case of sample I.7, it is difficult to observe similar behaviour, as the ZnI_2 thin layer formed a specific structure with a small thickness, and it can be inferred that ZnI_2 was a difficult material for PVD deposition.

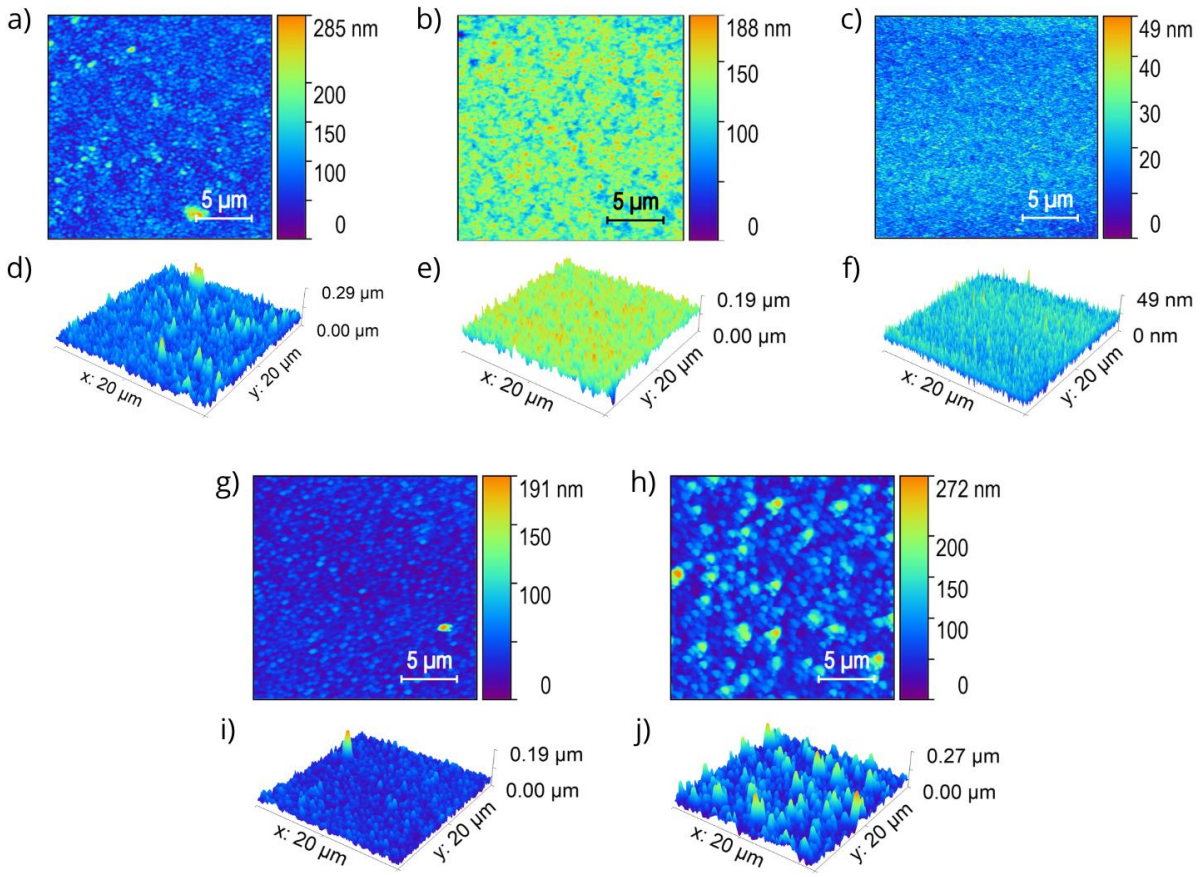

Figure 4.3. 2D and 3D AFM images (20 µm x 20 µm) of iodide perovskite thin films I.1-I.4, I.7 obtained using the PVco-D technique: I.1 (a, d), I.2 (b, e), I.3 (c, f), I.4 (g, i), I.7 (h, j).

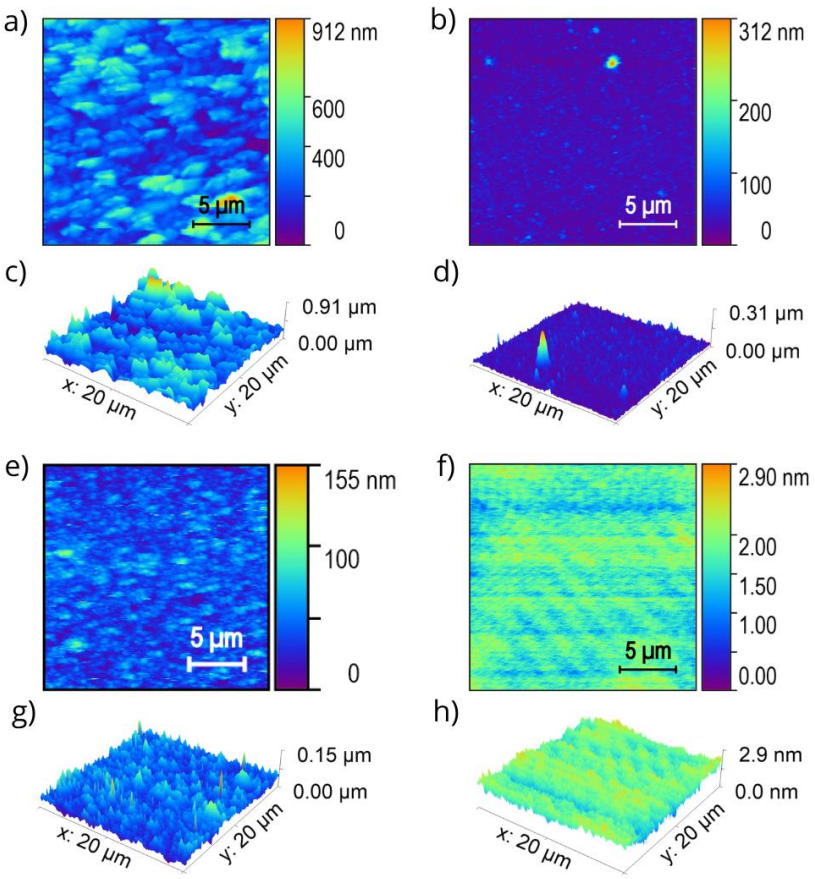

Figure 4.4. 2D and 3D AFM images (20 µm x 20 µm) of thin films of perovskite film-forming components I.1-I.4, I.7 obtained using the PVco-D technique: MAI (a, c), PbI_2 (b, d), CdI_2 (e, g), ZnI_2 (f, h).

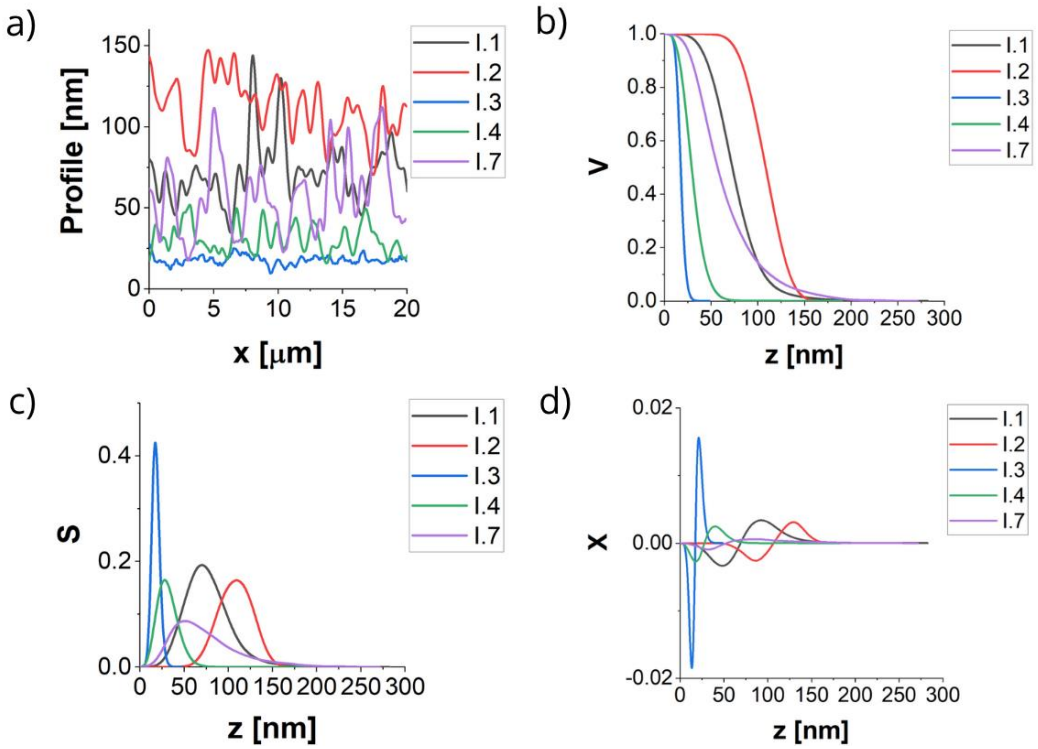

Figure 4.5. Profile (a) and Minkowski Functionals (V (b), S (c), χ (d)) of the studied perovskite thin films I.1-I.4, I.7.

Table 4.3. Mean crystallite height (h_{ave}) and Mean Square Roughness (MSR) of hybrid perovskite thin films I.1-I.4, I.7 and their constituent components MAI, PbI_2, CdI_2, ZnI_2 made by the PVco-D technique. The h_{ave} and MSR were calculated from AFM images, and the thicknesses of these films indicated by vacuum deposition system thickness sensors.

ID	h_{ave} [nm]	MSR [nm]	Thickness [nm]
I.1	76.60	26.34	300
I.2	108.96	20.04	300
I.3	17.81	4.46	300
I.4	31.40	12.56	170
I.7	66.67	35.56	260
MAI	300.02	110.48	300
PbI_2	30.42	13.63	300
CdI_2	40.32	14.26	150
ZnI_2	1.98	0.30	300

4.3.2. Chloride perovskites

Figure 4.6 shows the results of surface topography measurements of methylammonium chloride-containing (MACl) perovskite thin films. Figure 4.7 contains AFM images of the components forming them, i.e., MACl and $PbCl_2$, for comparison with images of the Cl.1-Cl.3 perovskites. The results of the AFM data analysis are included in Table 4.4 and Figure 4.8. The Cl.1-Cl.3 hybrid perovskite samples differ in the percentage composition of the individual components. Hence, the juxtaposition of the three samples provides interesting information on the effect of composition on the structure of the layers.

The $MAPbCl_3$ perovskite with a composition of 50% MACl : 50% $PbCl_2$ forms large crystallites of different heights, as evidenced by a sizable surface roughness of 105.41 nm. Note that the entire substrate surface is covered by the material - the percolation threshold is around 64 nm. However, a tendency for larger structures to form on the substrate surface can be seen here. The shape of the Minkowski Connectivity diagram shows a uniform distribution of islands and valleys in the study area. The surface topography clearly changes, increasing the MACl content (Figure 4.6be). In the AFM image, one notices areas with a very thin layer of material or no material at all. The tendency to form large crystallites reaching up to 4 μm is retained and is much more apparent. The inhomogeneity of the layer surface is a feature that hinders its successful application in optoelectronic devices. The roughness of the Cl.2 sample is almost 2.5 times that of the Cl.1 sample at 251.72 nm. The third composition Cl.3 is of poor quality, with areas of little or no structure thickness visible on the AFM image and single crystallites visible on the surface of the layer. The above statements are confirmed by MFs analysis. The best MFs characteristics were obtained for Cl.1, the worst for the Cl.3 layer.

From Figure 4.7, it can be deduced that MACl alone tends to form large, tall crystallites, whereas $PbCl_2$ deposition forms single tall pins, evenly distributed over the surface. As a result of the deposition of both materials in the codeposition, the larger crystallites are formed, the higher the MACl content and structures in the form of single pins when there is a higher $PbCl_2$ content.

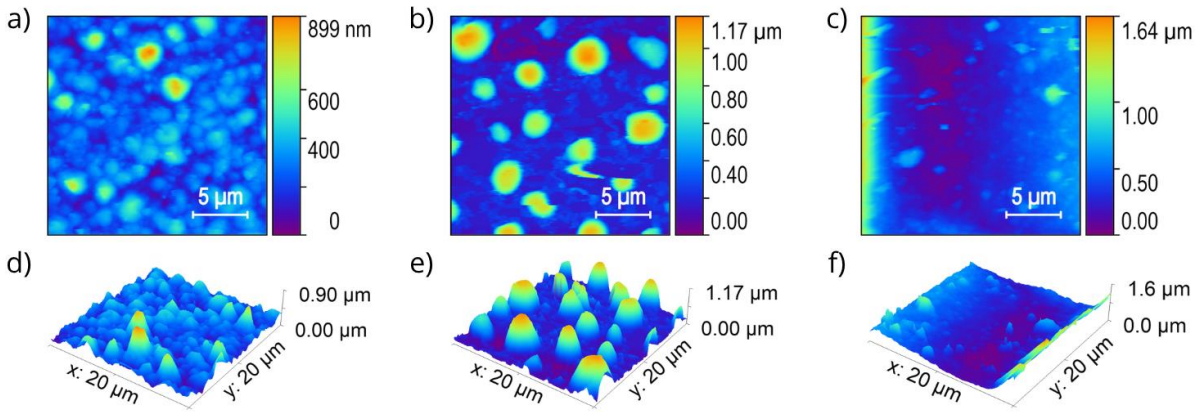

Figure 4.6. 2D and 3D AFM images (20 µm x 20 µm) of Cl.1-Cl.3 chloride perovskite thin films obtained using the PVco-D technique: Cl.1 (a, d), Cl.2 (b, e), Cl.3 (c, f).

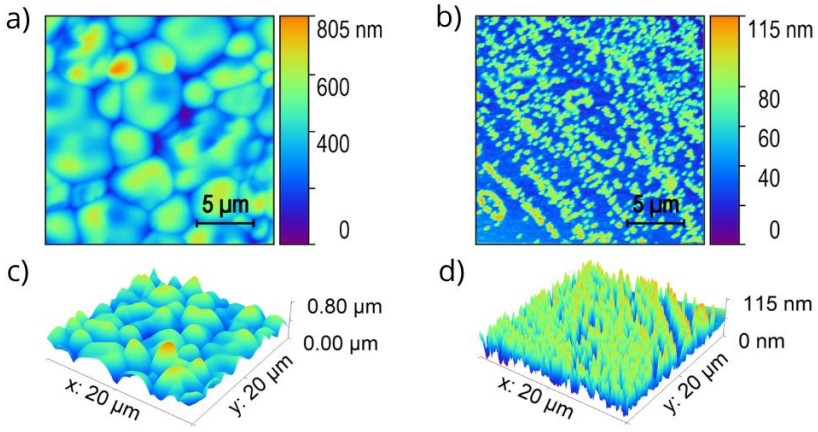

Figure 4.7. 2D and 3D AFM images (20 µm x 20 µm) of Cl.1-Cl.3 perovskite film-forming component thin films obtained using the PVco-D technique: MACl (a, c), $PbCl_2$ (b, d).

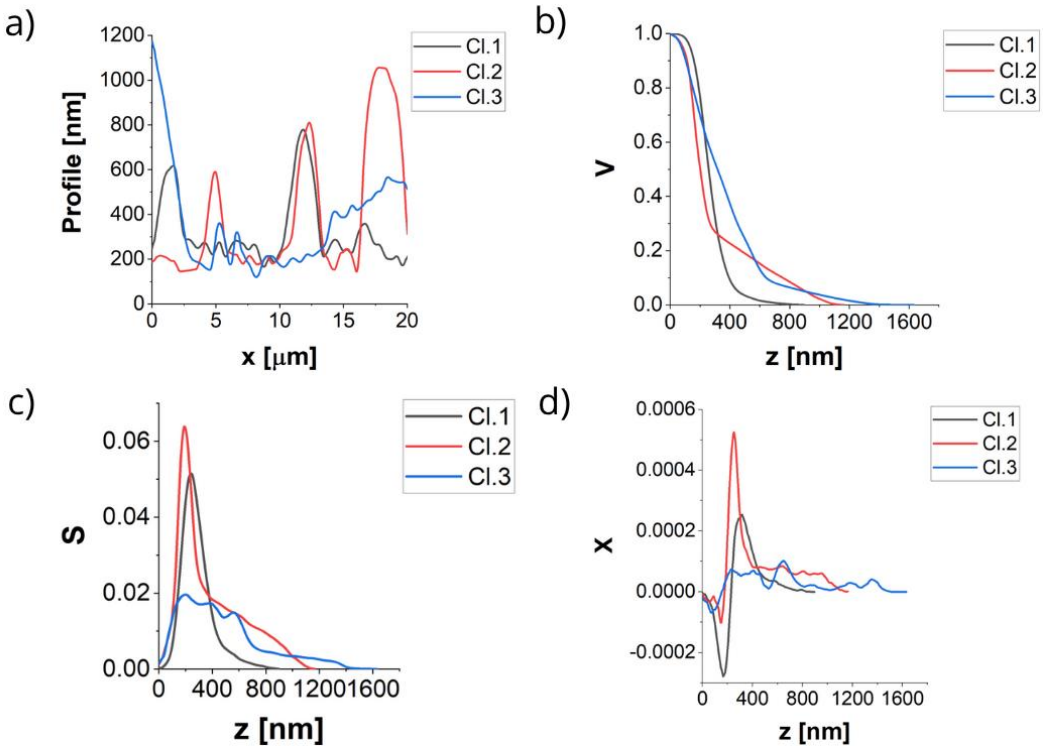

Figure 4.8. Profile (a) and Minkowski Functionals (V (b), S (c), χ (d)) of the investigated Cl.1-Cl.3 perovskite thin films.

Table 4.4. Mean crystallite height (h_{ave}) and Mean Square Roughness (MSR) of Cl.1-Cl.3 hybrid perovskite thin films and their constituent components MACl, $PbCl_2$ made by the PVco-D technique. The h_{ave} and MSR were calculated from AFM images, and the thicknesses of these films indicated by vacuum deposition system thickness sensors.

ID	h_{ave} [nm]	MSR [nm]	Thickness [nm]
Cl.1	276.20	105.41	300
Cl.2	309.01	251.72	300
Cl.3	373.00	253.50	300
MACl	409.53	108.50	160
$PbCl_2$	49.70	23.15	300

4.3.3. Bromide perovskites

Figure 4.9 shows the results of surface topography measurements of perovskite thin films containing methylammonium bromide MABr. AFM images of the components forming these films are included in Figure 4.10 for comparison with the results obtained for perovskites. The average height of the crystallites and the roughness of the structures are provided in Table 4.5. The results presented allow a comparison between two different perovskites with bromine - Figure 4.9a-eg shows the same perovskite but with a different composition, while Figure 4.9fh differs from the previous one by the B cation, which in this case is Sn. A more detailed analysis is provided by Figure 4.11, which compares layer profiles and Minkowski Functionals.

By introducing a Sn cation in place of the Pb cation, the $MASnBr_3$ perovskite thin film is more homogeneous, with a roughness of 3.71 nm. Individual high, narrow crystallites are seen on its surface. The percolation threshold is high at around 63 nm. The $MASnBr_3$ layer shown in Figure 4.9fh reaches a maximum height of 91.8 nm, more than 4 times less than the layer thickness indicated by the vacuum sputtering sensors. This results from a mixed type of thin film growth. Initially, the layer forms layer-by-layer on the substrate side, forming a compact structure. Later, after receiving a thickness of approximately 300 nm, the growth mode changes to island-type, and individual sharp crystallites appear on the structure's surface. Thin layers of $MAPbBr_3$ perovskite (Figure 4.9a-eg) form crystallites evenly distributed over the entire test surface. For Br.1 and Br.3, the crystallites are small, while larger structures appear on the surface of the Br.2 sample. Nevertheless, the roughness of all three Br.1-Br.3 compositions is very similar at 31.18 nm, 32.75 nm, and 33.02 nm, respectively. This is also confirmed by the layer profiles (Figure 4.11a). The percolation thresholds as seen in Figure 4.11b are satisfactory and are around 32 nm, 45 nm, and 65 nm, respectively. This means that the layer increases homogeneously from the substrate side during deposition up to the height of this threshold. At the same time, the χ -characteristics (Figure 4.11d) provide information about the uniform distribution of islands and valleys on the studied surfaces. The highest average crystallite height is 137.45 nm for sample Br.3, and the lowest is 96.66 nm for Br.1.

The nature of the surface topography of the Br.1-Br.3 structures can be explained by the data presented in Figure 4.10. The MABr thin films are composed of larger crystallites, no larger than 2 µm, while the $PbBr_2$ surface is generally formed by undersized, narrow, sharp crystallites. Therefore, when the content of the methylammonium moiety is increased in $MAPbBr_3$ perovskite, the topography of its surface reveals the occurrence of larger structures, and increasing the $PbBr_2$ content results in a decrease in the size of the crystallites forming the perovskite.

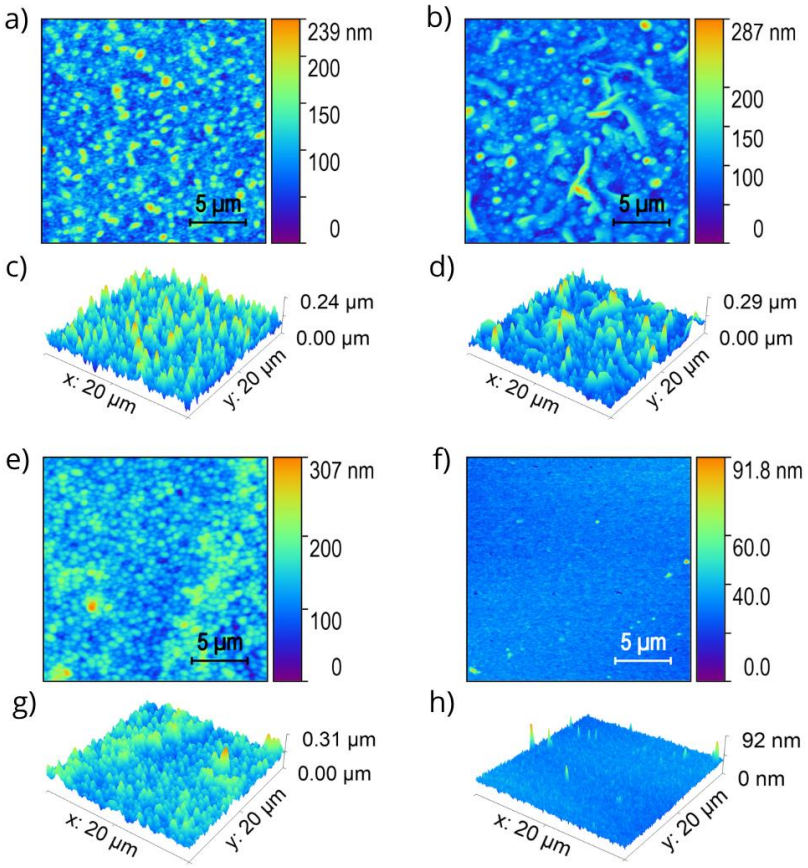

Figure 4.9. 2D and 3D AFM images (20 µm x 20 µm) of Br.1-Br.4 bromide perovskite thin films obtained using the PVco-D technique: Br.1 (a, c), Br.2 (b, d), Br.3 (e, g), Br.4 (f, h).

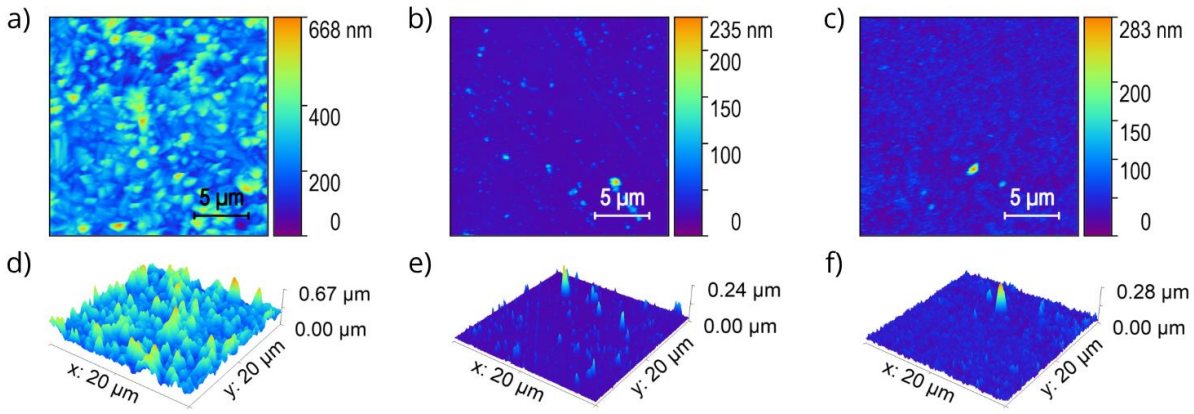

Figure 4.10. 2D and 3D AFM images (20 µm x 20 µm) of Br.1-Br.4 perovskite film-forming component thin films obtained using the PVco-D technique: MABr (a, d), $PbBr_2$ (b, e), $SnBr_2$ (c, f).

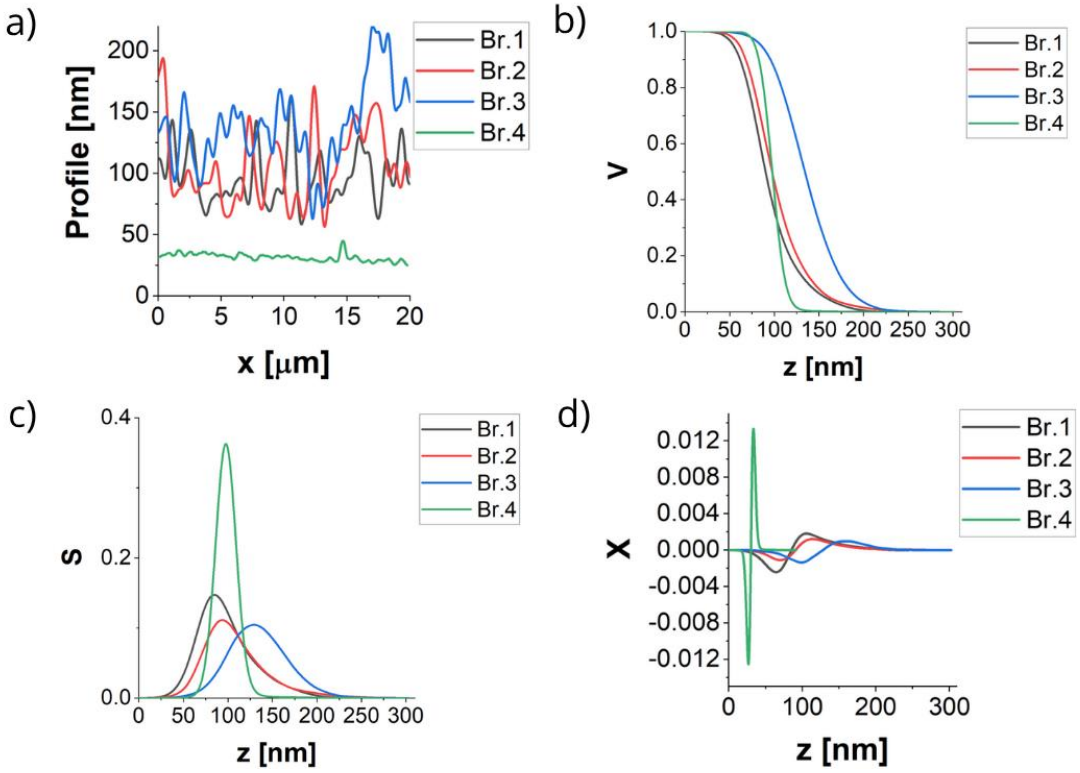

Figure 4.11. Profile (a) and Minkowski Functionals (V (b), S (c), χ (d)) of the investigated Br.1-Br.4 perovskite thin films.

Table 4.5. Mean crystallite height (h_{ave}) and Mean Square Roughness (MSR) of Br.1-Br.4 hybrid perovskite thin films and their constituent components MABr, $PbBr_2$, $SnBr_2$ made by the PVco-D technique. The h_{ave} and MSR were calculated from AFM images, and the thicknesses of these films indicated by vacuum deposition system thickness sensors.

ID	h_{ave} [nm]	MSR [nm]	Thickness [nm]
Br.1	96.66	31.18	300
Br.2	104.26	32.75	300
Br.3	137.45	33.02	300
Br.4	30.41	3.71	400
MABr	228.94	87.21	180
$PbBr_2$	10.00	9.58	180
$SnBr_2$	36.10	12.44	300

4.3.4. Conclusions

In the part of the work related to the description of structural properties, thin films of hybrid perovskites I.1-I.4, I.7, Cl.1-Cl.3, Br.1-Br.4 were obtained and described. These were structures composed of methylammonium and inorganic parts such as PbI_2, CdI_2, ZnI_2, $PbCl_2$, $PbBr_2$, and $SnBr_2$. The described data set allows comparison of the surface topography of perovskites differing in B cation and X anion (based on the general formula of perovskites ABX_3) and provides information on the influence of perovskite composition on its structure. Based on the above data, it is concluded that the perovskites forming the most homogeneous structures are the perovskites containing iodine and bromine. In the case of samples I.1-I.3 and Br.1-Br.4, the deposited material uniformly covers the entire study area. In the case of samples I.4 and I.7, some inhomogeneities are evident on the recorded surfaces, which may pose problems in potential optoelectronic applications. Samples of perovskites containing chloride Cl.1-Cl.3 are less homogeneous, and increasing the MACl content in the perovskite structure results in the formation of large single crystallites, significantly increasing the layer's roughness [10]. About methylammonium iodide hybrid perovskites ($MAPbI_3$), available sources provide information on film roughness from 10 nm to 20 nm [11]. However, these are studies of perovskite thin films obtained from solution by a different

deposition technique than the one used in the present work. Despite the discrepancies concerning the technique for obtaining the layers, the calculated roughnesses of samples I.1-I.4 and I.7 are similar to those presented in the work of Hidalgo *et al.* The compositions 50% MAX : 50% PbX_2 (X = I, Cl, Br) and the composition 70% MAI : 30% PbI_2 stand out in terms of layer quality compared to the others, and these could be the best candidates for further applications in optoelectronics. However, one should be aware that these materials contain toxic substances, which is a very serious limitation.

4.4. UV-VIS-NIR spectroscopic studies

Spectroscopic studies in the UV-VIS-NIR wavelength range were conducted as described in *Chapter 3*, S*ection 3.1*. All halide perovskite thin films with iodide (I.1-I.7), chloride (Cl.1-Cl.3), and bromide (Br.1-Br.4) anions analyzed in this work were examined and the results compared. The resulting transmission spectra are presented in the following subsections. Two vertical dashed lines (SHG, THG) are plotted in Figures 4.12-14, which are related to second- and third-order nonlinear optical effects. The lines cross the horizontal axis perpendicularly at specific locations. The SHG line intersects the "Wavelength" axis at λ = 532 nm and the THG line at λ = 355 nm. The absorption coefficients α were determined for both wavelengths, and the data are collected in Table 4.6-8.

4.4.1. Iodide perovskites

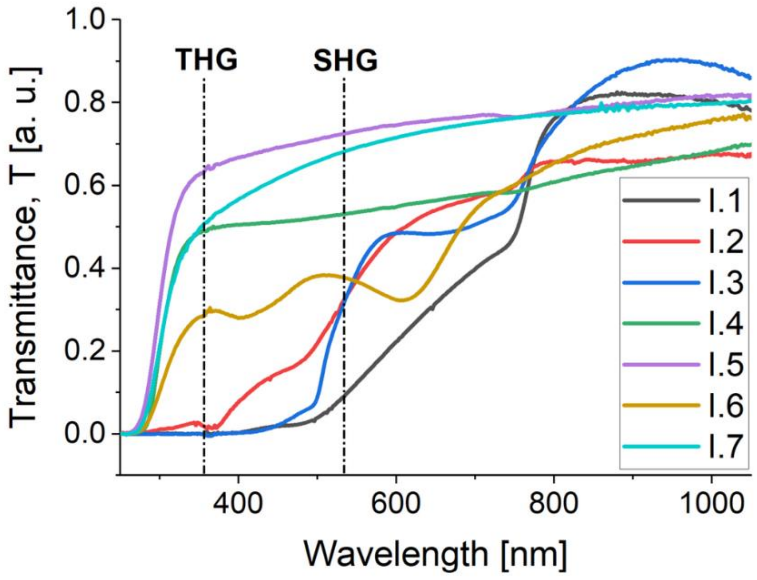

Figure 4.12. UV-VIS-NIR transmission spectra of hybrid perovskite thin films with methylammonium iodide MAI.

From the data in Figure 4.12, it can be seen that the studied iodide perovskite thin film samples absorb electromagnetic radiation in almost the entire spectral range studied. This absorption varies in character from sample to sample. The most absorbing perovskites are I.1-I.3 and I.6. Their strongest radiation absorption region falls in the region from about 300 nm to 800 nm. The transmission spectra of these samples are characterized by several maxima. In the case of I.1, these are blurred maxima at 729 nm and 880 nm, for I.2, maxima are observed at about 344 nm, 450 nm, 720 nm, and 796 nm, and for I.3, at 483 nm, 591 nm, and 940 nm. Sample I.6 has maxima at 365 nm, 513 nm, 716 nm, and 858 nm. Regarding the effect of the composition on the spectra obtained (samples I.1-I.3), it is clear that the strongest absorption is observed for the 50% : 50% composition (I.1).

Table 4.6. Absorption coefficients α of thin films I.1-I.7 and wavelengths of maxima λ_{trans} observed in transmission spectra.

ID	α [10^4 cm^{-1}]		λ_{trans} [nm]
	355 nm	532 nm	
I.1	27.31	8.17	729, 880
I.2	13.22	3.86	344, 450, 720, 796
I.3	31.00	3.97	483, 591, 940
I.4	4.24	3.77	-
I.5	6.69	4.65	-
I.6	3.19	2.45	365, 513, 716, 858
I.7	2.68	1.50	-

4.4.2. Chloride perovskites

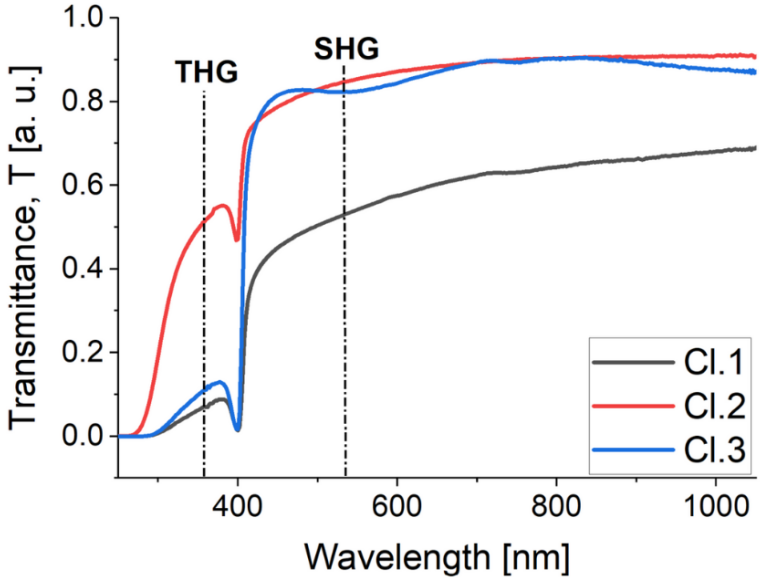

Figure 4.13. UV-VIS-NIR transmission spectra of hybrid perovskite thin films with methylammonium chloride MACl.

The data in Figure 4.13 indicate that chloride hybrid perovskites absorb radiation most strongly in the wavelength range from about 300 nm to 410 nm. For longer wavelengths in the investigated range, relatively negligible absorption is observed, and the shape

of the transmission spectra is flattened, without clear maxima. The obtained transmission spectra of the Cl.1-Cl.3 materials have a similar character. For all three samples, a transmission maximum is observed at 380 nm. The strongest absorption is shown by Cl.1. Changing the composition of the perovskite with chlorine results in an increase of more than 6 times in the intensity of the observed transmission spectrum maximum.

Table 4.7. Absorption coefficients α of thin films Cl.1-Cl.3 and wavelengths of maxima λ_{trans} observed in transmission spectra.

ID	α [10^4 cm^{-1}]		λ_{trans} [nm]
	355 nm	532 nm	
Cl.1	9.11	2.15	380
Cl.2	2.30	0.56	380
Cl.3	7.59	0.66	380

4.4.3. Bromide perovskites

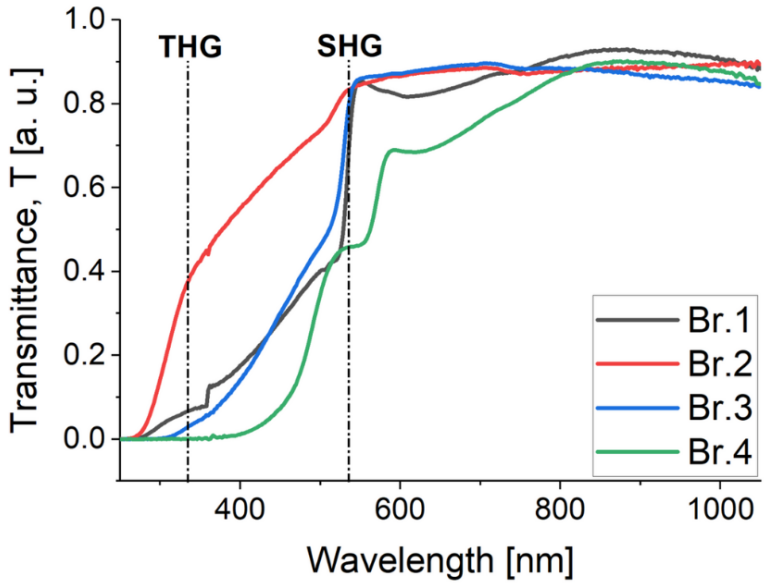

Figure 4.14. UV-VIS-NIR transmission spectra of hybrid perovskite thin films with methylammonium bromide MABr.

It can be seen from Figure 4.14 that bromide hybrid perovskites absorb radiation most strongly in the region from about 300 nm to almost 590 nm. For the longer wavelengths of the spectral range studied, relatively negligible absorption is observed. Samples Br.1, Br.3, and Br.4 have similar shaped spectra, while a flatter shape characterizes Br.2. Transmission maxima are observed for all samples, which are indicated in Table 4.8. The strongest absorption is shown by Br.4. About the effect of composition on the transmission spectra (samples Br.1-Br.3), it is clear from the data presented that increasing the content of the methylammonium moiety reduces the material's absorption.

Table 4.8. Absorption coefficients α of thin films Br.1-Br.4 and wavelengths of maxima λ_{trans} observed in transmission spectra.

ID	α [10^4 cm^{-1}]		λ_{trans} [nm]
	355 nm	532 nm	
Br.1	8.62	1.86	514, 550, 865
Br.2	2.76	0.63	490, 712
Br.3	10.07	1.02	496, 708
Br.4	15.57	1.98	522, 592, 862

4.4.4. Conclusions

The strongest absorption properties and the widest absorption range are exhibited by thin films of perovskites with iodine I.1-I.3 and I.6. The absorption range in this case is in the wavelength range 300 - 800 nm. The weakest absorption is shown by perovskites with chlorine, for which the absorption range is between 300 nm and 410 nm. Perovskites with bromine have an intermediate absorption bandwidth compared to the other materials tested, falling 300 - 590 nm. These results are in good approximate agreement with literature reports [12,13]. Such absorption relationships between the tested materials can be explained by the electro-negativity of the halogen (I, Cl, Br) and its size. The higher the electro-negativity (χ_h) of the halogen ($\chi_{hI} = 2.66$, $\chi_{hCl} = 3.16$, $\chi_{hBr} = 2.96$) and the smaller its size ($r_I = 220\,pm$, $r_{Cl} = 181\,pm$, $r_{Br} = 196\,pm$), the more the absorption band is shifted towards shorter wavelengths. Therefore, perovskites with iodine are better suited

for photovoltaic applications, while perovskites with chlorine and bromine are more suitable for other optoelectronic applications.

In the context of the nonlinear optical properties of SHG and THG thin films, the materials must be optically transparent for the laser beam wavelength of 1064 nm. Furthermore, it is also important that for wavelengths of 355 nm and 532 nm, i.e., the wavelengths corresponding to THG and SHG, respectively (dashed lines in Figure 4.12-14), the absorption is minimal. Otherwise, the generated SHG and THG signals are absorbed simultaneously. In the recorded perovskite spectra, the absorption is often non-zero for these wavelengths. Therefore, absorption effects must be considered when calculating the SHG and THG properties, so absorption coefficients α were calculated for both wavelengths (Table 4.6-8).

4.5. Aging tests

Aging tests were carried out on thin film samples of hybrid perovskites I.1-I.3, Cl.1-Cl.3, and Br.1-Br.3. The tests were carried out as described in *Chapter 3*, S*ection 3.4*. The data obtained are summarized below in the form of 2D AFM images of 20 µm x 20 µm and tables containing information on mean crystallite height (h_{ave}) and Mean Square Roughness (MSR). These results were supported by transmission spectra of the materials studied. Surface topography and spectroscopic studies were repeated over time. The first measurement was performed immediately after the layer was obtained using the PVco-D technique, with subsequent measurements carried out after 1 week, 1 month, 2 months, and 6 months. The study aims to record the structural and spectroscopic changes over time in the thin film structures of hybrid perovskites, as perovskites are considered rapidly degrading materials [14].

4.5.1. Iodide perovskites

Aging tests of the iodide perovskites show similar relationships for all three samples I.1-I.3. As time passes, the thin film structures degrade. AFM images confirm that the degradation occurs very rapidly. After just one week, the surface topography of the layer changes - AFM images of samples I.1 and I.2 show that holes appear on the sample surface. The reason for this behaviour is ion migration. Ions migrate and accumulate to form higher

agglomerations. This has the effect of increasing the average height of the crystallites and the roughness of the sample. After 1 month, a large part of the crystallites on the surface of sample I.1 disintegrate and form a locally relatively uniform surface. A small number of single, very high crystallites are still observed on the surface, which significantly contribute to the layer's average roughness. The transmission of this layer varies a little over the 6-month period, as can be seen in Figure 4.16a. Sample I.2, with its higher methylammonium content, degrades over one month in the same way - the passage of time causes the ions to cluster and larger and larger structures are created. Such significant changes in topography are also visible in the transmission spectra. After 1 week, the 344 nm peak in the spectrum increases significantly in intensity, and after 1 month, the transmission increases significantly and the resulting spectrum is flattened (Figure 4.16b). In the case of sample I.3, after 1 week or even 1 month, the surface of the sample is uniformly covered with material, while single relatively high structures with small sizes appear. The transmission spectrum is relatively stable, and no significant changes are observed.

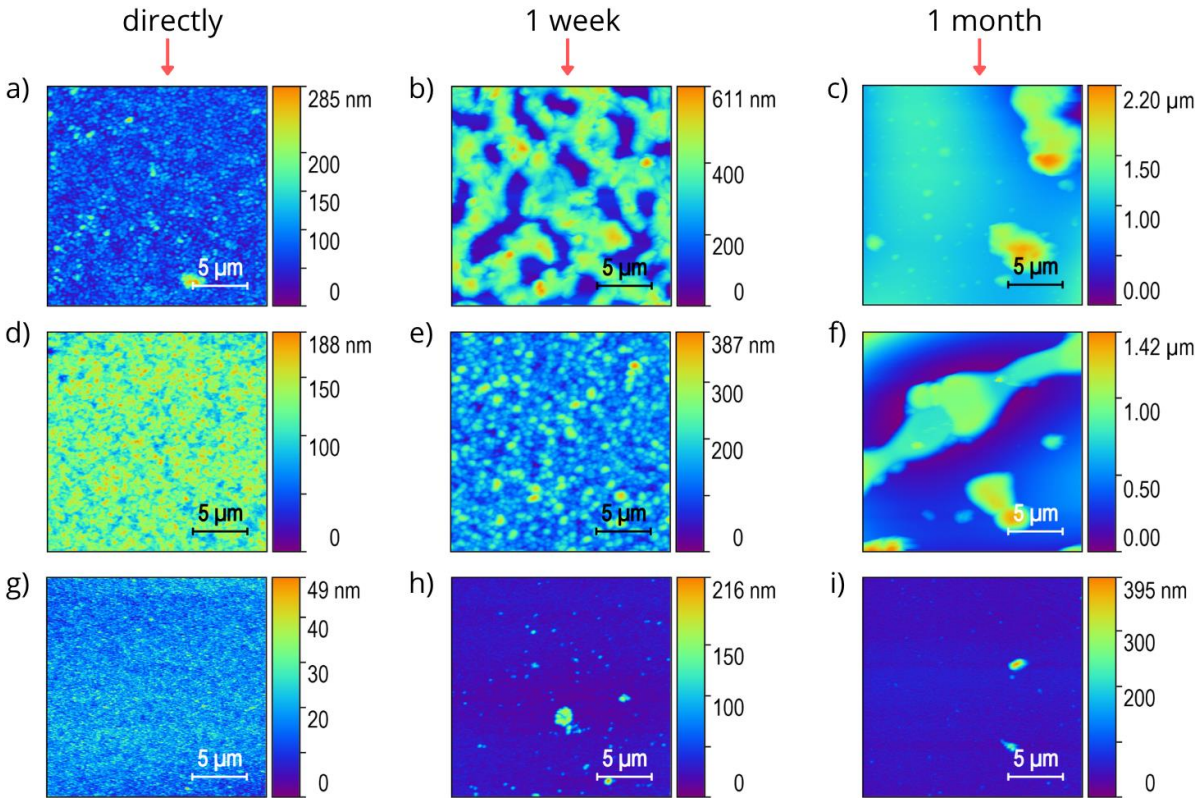

Figure 4.15. 2D AFM images of perovskite thin films I.1 (a-c), I.2 (d-f), I.3 (g-i), carried out after a specific time after sample fabrication: directly (a, d, g), after 1 week (b, e, h), after 1 month (c, f, i).

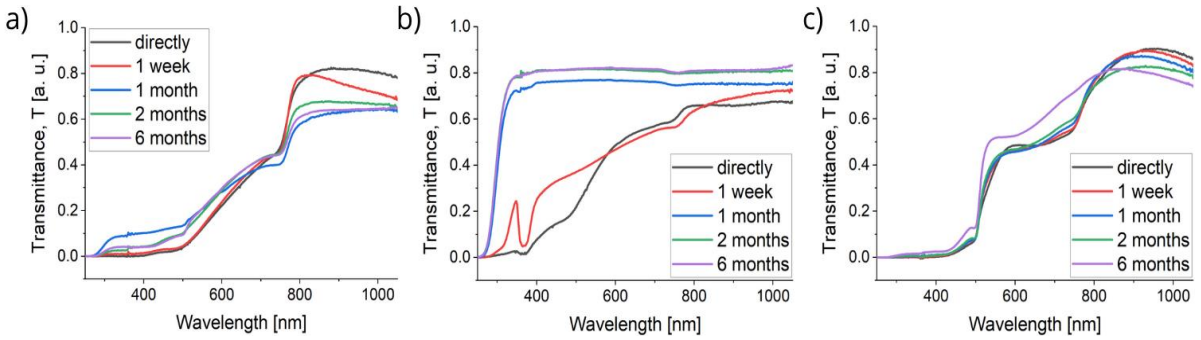

Figure 4.16. Graphs showing normalized results of transmission measurements of perovskite thin films: I.1 (a), I.2 (b), I.3 (c), which were carried out as a function of time, counting from the moment the sample was made.

Table 4.9. Mean crystallite height (h_{ave}) and Mean Square Roughness (MSR) of I.1-I.3 hybrid perovskite thin films made by the PVco-D technique, calculated from the AFM images shown in Figure 4.15.

ID	Time							
	Directly		1 week		1 month		6 months	
	h_{ave} [nm]	MSR [nm]	h_{ave} [nm]	MSR [nm]	h_{ave} [nm]	MSR [nm]	h_{ave} [nm]	MSR [nm]
I.1	76.60	26.34	290.53	128.51	1253.62	242.06	1391.00	446.40
I.2	108.96	20.04	151.85	45.02	432.00	298.70	693.28	400.35
I.3	17.81	4.46	24.90	12.93	47.70	16.28	43.50	7.28

4.5.2. Chloride perovskites

Chloride perovskites are highly degradable. Despite storing the samples in an argon atmosphere, degradation proceeds rapidly. As described in *Section 3.2* of this chapter, the Cl.1 perovskite with a 50% MACl : 50% $PbCl_2$ composition shows the most uniform structure. The other compositions form heterogeneous layers, as can be clearly seen in Figure 4.17dg. In contrast, after just one week, especially after 2 months, it is not easy to find a spot on the sample's surface where the surface topography is formed by crystallites. In the AFM images of the Cl.1 and Cl.2 samples, after 1 week, single, large, and tall structures randomly distributed over the study area are observed. After 2 months, the Cl.1 surface is formed by larger and taller crystallites, and the Cl.2 surface gradually disappears, confirming the decrease in h_{ave} and MSR values. The Cl.3 sample undergoes severe degradation after 1 week. Ion migration and disintegration of pre-existing crystallites take place. The result is the formation of very high crystallites that are difficult to measure with the microscope used for the measurements. In Figure 4.17h, it can be seen that the sample's surface is covered with the test material, and the high crystallites, difficult to measure for the microscope, have been damaged by the measuring probe. This shows that the height of the crystallites was really high (this is confirmed by the maximum value on the height scale of Figure 4.17h). Nevertheless, after 2 months, due to the progression of degradation processes, the remaining ions

on the surface formed large, but already lower structures than before, and the average height of the crystallites and the average roughness decreased. The degradation processes of samples Cl.1-Cl.3 are confirmed by the transmission spectra in Figure 4.18. For samples Cl.1 and Cl.2, an increase in the 380 nm peak intensity is characteristic. No such behaviour is observed for sample Cl.3.

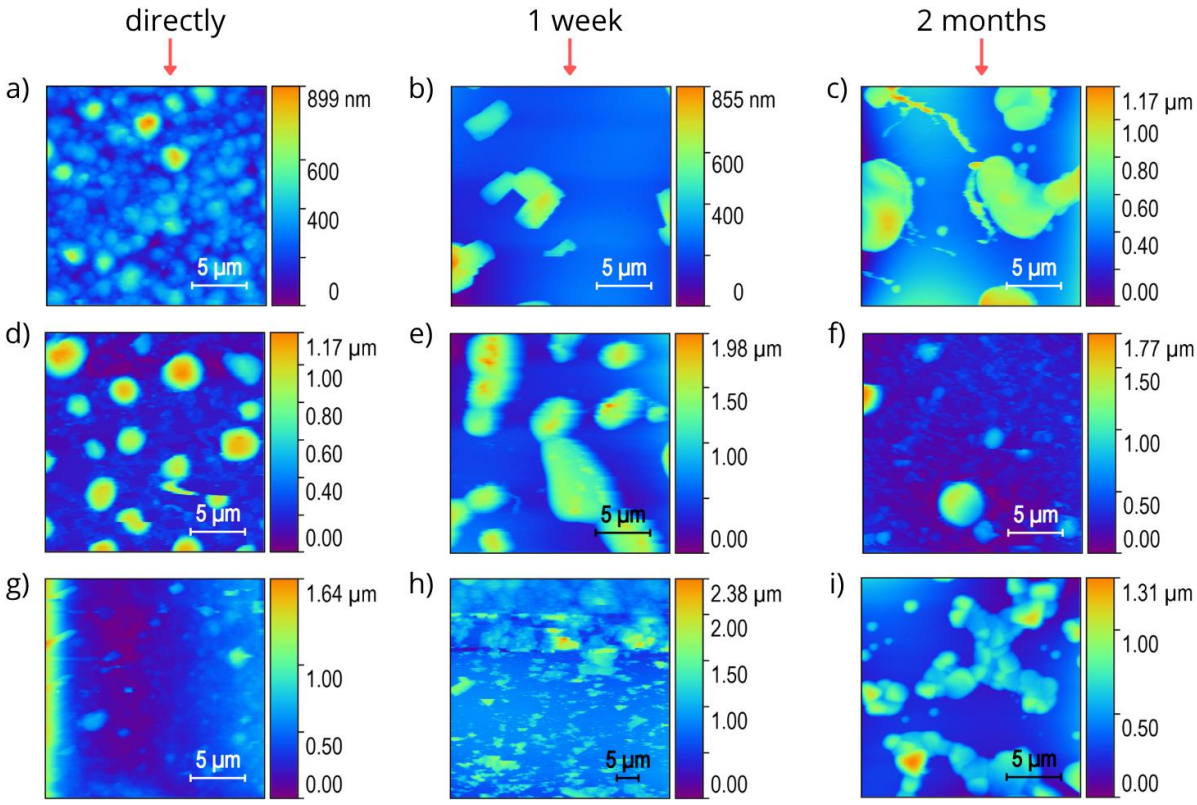

Figure 4.17. 2D AFM images of perovskite thin films Cl.1 (a-c), Cl.2 (d-f), Cl.3 (g-i), carried out after a specific time after sample fabrication: directly (a, d, g), after 1 week (b, e, h), after 2 months (c, f, i).

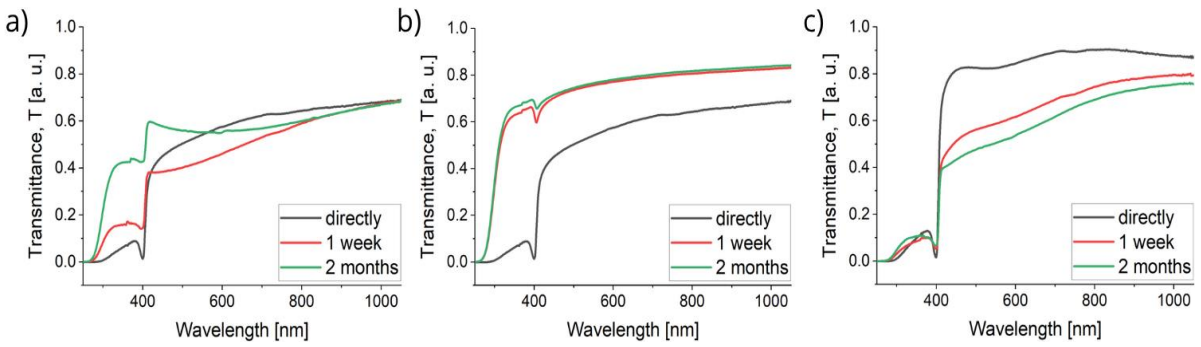

Figure 4.18. Graphs showing normalized results of transmission measurements of perovskite thin films: Cl.1 (a), Cl.2 (b), Cl.3 (c), which were carried out as a function of time, counting from the moment the sample was made.

Table 4.10. Mean crystallite height (h_{ave}) and Mean Square Roughness (MSR) of Cl.1-Cl.3 hybrid perovskite thin films made by the PVco-D technique, calculated from the AFM images shown in Figure 4.17.

ID	Time					
	Directly		1 week		2 months	
	h_{ave} [nm]	MSR [nm]	h_{ave} [nm]	MSR [nm]	h_{ave} [nm]	MSR [nm]
Cl.1	276.20	105.41	257.80	108.40	522.90	194.20
Cl.2	309.01	251.72	714.00	403.90	274.57	207.12
Cl.3	373.00	253.50	888.50	225.08	408.28	215.21

4.5.3. Bromide perovskites

While bromide perovskites degrade over time, this occurs more slowly, and after 2 months, the surfaces of the Br.1-Br.3 samples tested are still covered relatively evenly with the material. However, the nature of the layers changes. AFM images of sample Br.1 (Figure 4.19ab) show that it is formed by single, small crystallites, and after 2 months, the crystallites disintegrate and a more homogeneous surface is formed. This is confirmed by the decrease in roughness of the layer. After 6 months, the Br.1 structure parameters (h_{ave}, MSR) change little compared to those calculated for 2 months (Table 4.11). On the surface of the Br.2 sample, single structures persist for 2 months, evenly distributed over the entire test area. The crystallites' average height and roughness are very close during

this time interval. After 6 months, a significant degradation progression is observed in this case. MSR and h_{ave} significantly reduce their values. The Br.3 material changes in structure over 2 months from finer crystallites to structures that are almost twice as large, but equally abundant throughout the study area. The spectroscopic spectra provide information that the greatest changes in optical properties occur within the first week of thin film formation. Subsequent results, for longer times (1 month, 2, and 6 months), are very similar to each other.

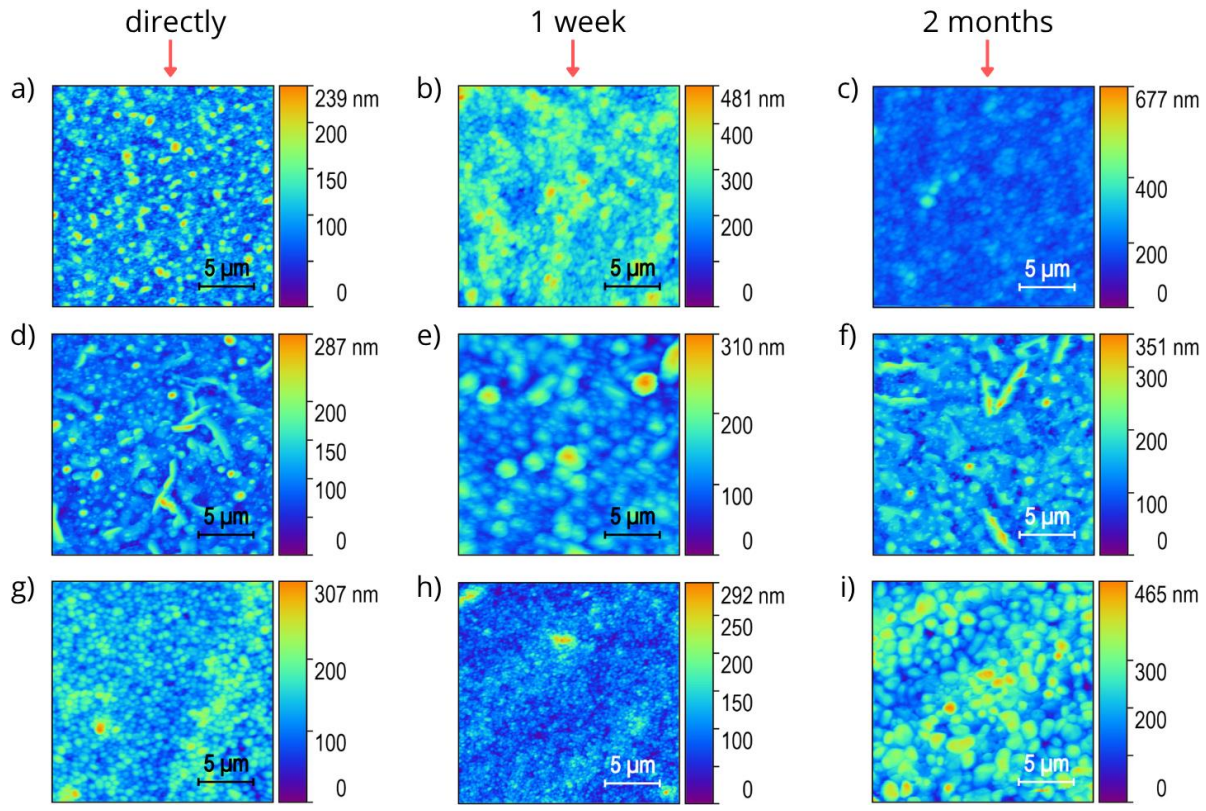

Figure 4.19. 2D AFM images of perovskite thin films Br.1 (a-c), Br.2 (d-f), Br.3 (g-i), carried out after a specific time after sample fabrication: directly (a, d, g), after 1 week (b, e, h), after 2 months (c, f, i).

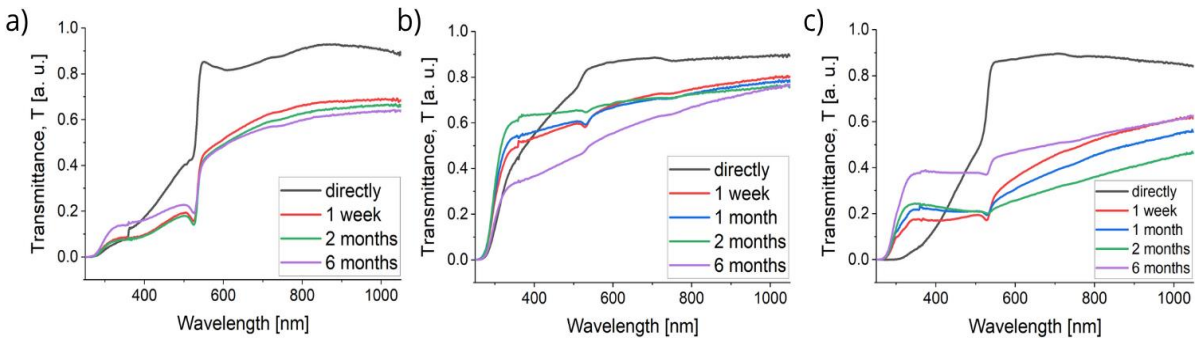

Figure 4.20. Graphs showing normalized results of transmission measurements of perovskite thin films: Br.1 (a), Br.2 (b), Br.3 (c), which were carried out as a function of time, counting from the moment the sample was made.

Table 4.11. Mean Crystallite Height (h_{ave}) and Mean Square Roughness (MSR) of Br.1-Br.3 hybrid perovskite thin films made using the PVco-D technique, calculated from the AFM images shown in Figure 4.19.

ID	Time							
	Directly		1 week		2 months		6 months	
	h_{ave} [nm]	MSR [nm]	h_{ave} [nm]	MSR [nm]	h_{ave} [nm]	MSR [nm]	h_{ave} [nm]	MSR [nm]
Br.1	96.66	31.18	251.19	53.44	193.68	33.52	193.49	56.94
Br.2	104.26	32.75	116.55	37.73	139.92	38.65	2.32	0.74
Br.3	137.45	33.02	91.13	29.02	229.99	65.20	634.4	211.21

4.5.4. Conclusions

To summarize this paragraph, it should be said that perovskites undergo significant degradation, which should be considered when conducting scientific research and designing optoelectronic perovskite devices. The investigated degradation processes in surface topography and transmission spectra indicate that, among the investigated perovskites, I.1 as well as Br.1 and Br.3 are the most stable due to surface structure for up to 6 months. The literature provides information on the stability period of perovskites with bromine exceeding 30 days [15]. On the other hand, due to optical transmission properties, I.1, I.3 and Br.1 are stable for up to 6 months. Perovskite I.2 has a shorter optical stability period

of about 1 week. In all perovskites of the Br group, the most significant changes occur during the first week after the structure is obtained. Perovskite containing chloride anions shows the greatest instability - it degrades the fastest, is very sensitive to the external environment, and is therefore a difficult material for optoelectronic applications.

4.6. Examination of phase transitions

Phase transitions in perovskite materials I.1-I.3, Cl.1-Cl.3, and Br.1-Br.3 were studied by measuring UV-VIS-NIR and PL spectroscopic properties as a function of temperature from 80 - 310 K with a step of 10 K. The measurement series of a given material was started from the lowest temperature. The measurement procedure was described in *Chapter 3*, S*ections 3.1* and *3.2.* The results obtained were analyzed. The data set from the UV-VIS-NIR spectrometer and the HORIBA spectrofluorometer for one sample was compared, paying particular attention to changes in the spectra. The observed changes were related to the intensity, shape, and direction of the spectrum shift. The data obtained are presented below, for each type of perovskite separately.

4.6.1. Iodide perovskites

The presented transmission measurement results of samples I.1-I.3 are shown in Figure 4.21. Two of the three compositions tested showed interesting changes in the transmission spectra. Shifting of the spectrum in the wavelength ranges tested is observed, while the most interesting changes in the shape of the spectrum occur in the areas from 700 nm to 860 nm (sample I.1) and 710 - 790 nm (sample I.3). Paying particular attention to these wavelength ranges, it is observed that temperature changes shift the absorption edge towards shorter or longer wavelengths. Such shifts in the spectrum occur alternately - at one time they are smooth and at other times they occur abruptly. Based on the observed shifts, the temperature specific points at which the investigated materials' phase transitions occurred were determined (Table 4.12).

In the transmittance spectra of perovskite I.1, the spectrum initially shifts towards shorter wavelengths as the temperature increases to 120 K, and then from 120 K to 150 K, shifts towards longer wavelengths. At higher temperatures, the spectrum again moves towards shorter

wavelengths. Along the way, two sudden jumps towards longer wavelengths are observed at temperatures of 220 K and 240 K. Hence, the phase transition from the orthorhombic to the tetragonal phase in sample I.1 is defined in the temperature range 120 - 150 K. For this material, the temperature range indicated is the range in which the two phases can coexist. Below 120 K, the sample is in the orthorhombic phase, and above 150 K in the tetragonal phase. The spectra of sample I.3 initially, up to 140 K, move towards longer wavelengths, and in the range 140 - 300 K, they gently move towards shorter wavelengths. At 310 K, an abrupt but small transition towards longer wavelengths is observed. Hence, two phase transitions are indicated here - from orthorhombic to tetragonal phase at ~140 K and from tetragonal to cubic phase at 310 K. For composition I.2, no change is observed in the spectrum. The spectrum is flat in the wavelength range larger than 350 nm, which may indicate that the thin film has degraded significantly.

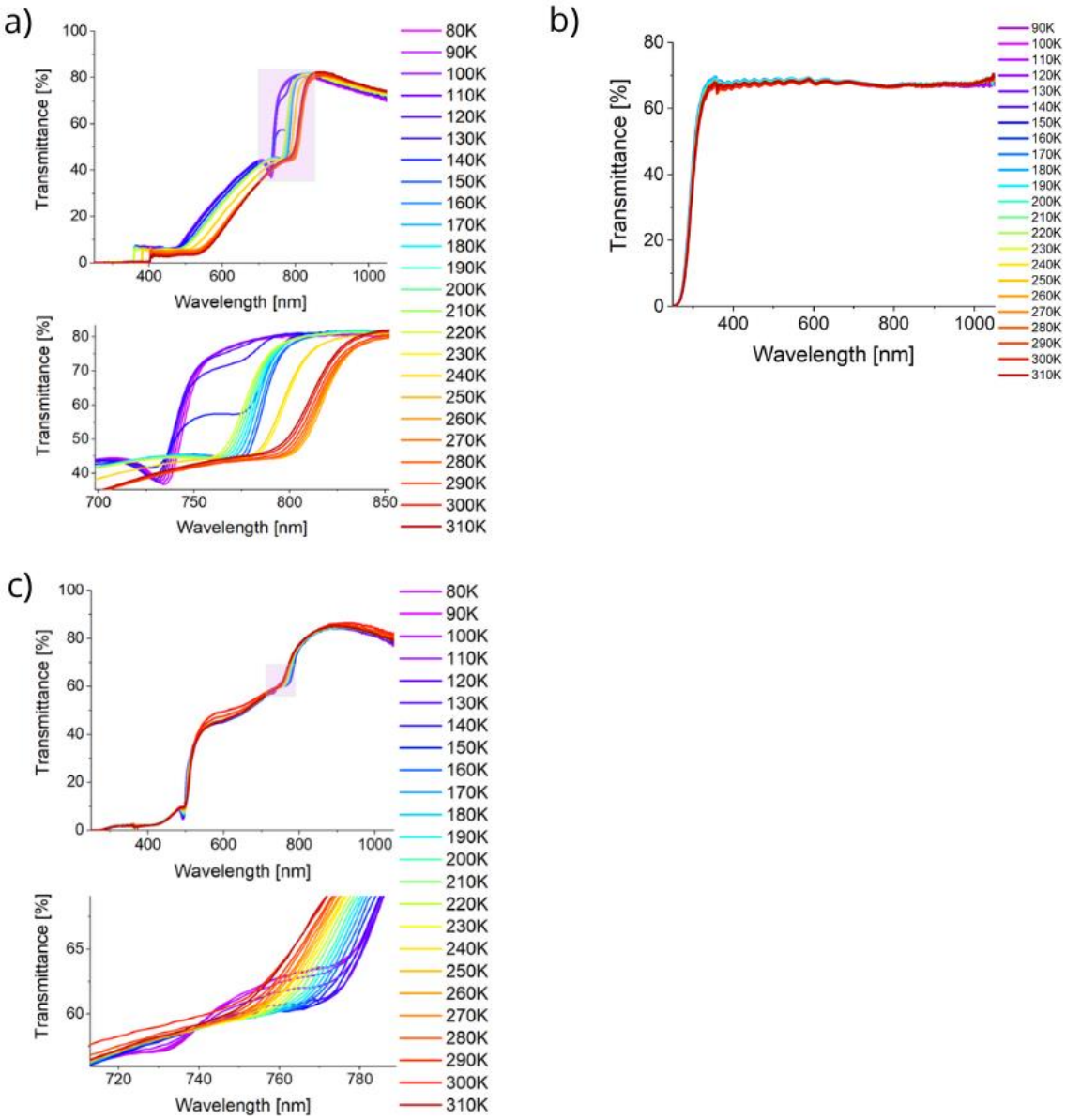

Figure 4.21. UV-VIS-NIR transmission spectra of perovskite thin films I.1-I.3 as a function of temperature: I.1 (a), I.2 (b), I.3 (c). Shaded areas have been magnified.

For the PL measurements, initial measurements were carried out to determine the excitation wavelength (Figure 4.22). To maintain the same measurement conditions for the three different perovskite compositions I.1-I.3, a single common excitation wavelength of 420 nm was chosen. The results of testing and analysis are presented in Figure 4.23-25. The graphs in Figure 4.24 indicate the intensity of the peaks appearing in the spectrum and their position as a function of temperature. Given this data set, a phase transition temperature of 140 K was indicated for sample I.1. This is the particular place where the most intense peak (Peak 2) disappears

and the place where the second most intense peak (Peak 3) reaches an intensity that already changes little with further temperature increase. Sample I.2, is very similar - the phase transition occurs at 140 K, confirmed by the disappearance of three of the four peaks appearing in the spectra. In material I.3, two phase transitions were detected at 140 - 160 K and at ~RT based on changes in the intensity of the main peak (Peak 2) and the appearance of an additional peak - Peak 3. Figure 4.25 compares the PL spectra of materials at the lowest and highest temperatures from the selected range. It is interesting to note that the intensities of the ~775 nm peak are comparable at high temperature for all three materials studied, while at low temperature, the intensity of this peak for I.1 is about 4 times higher than for the other two materials.

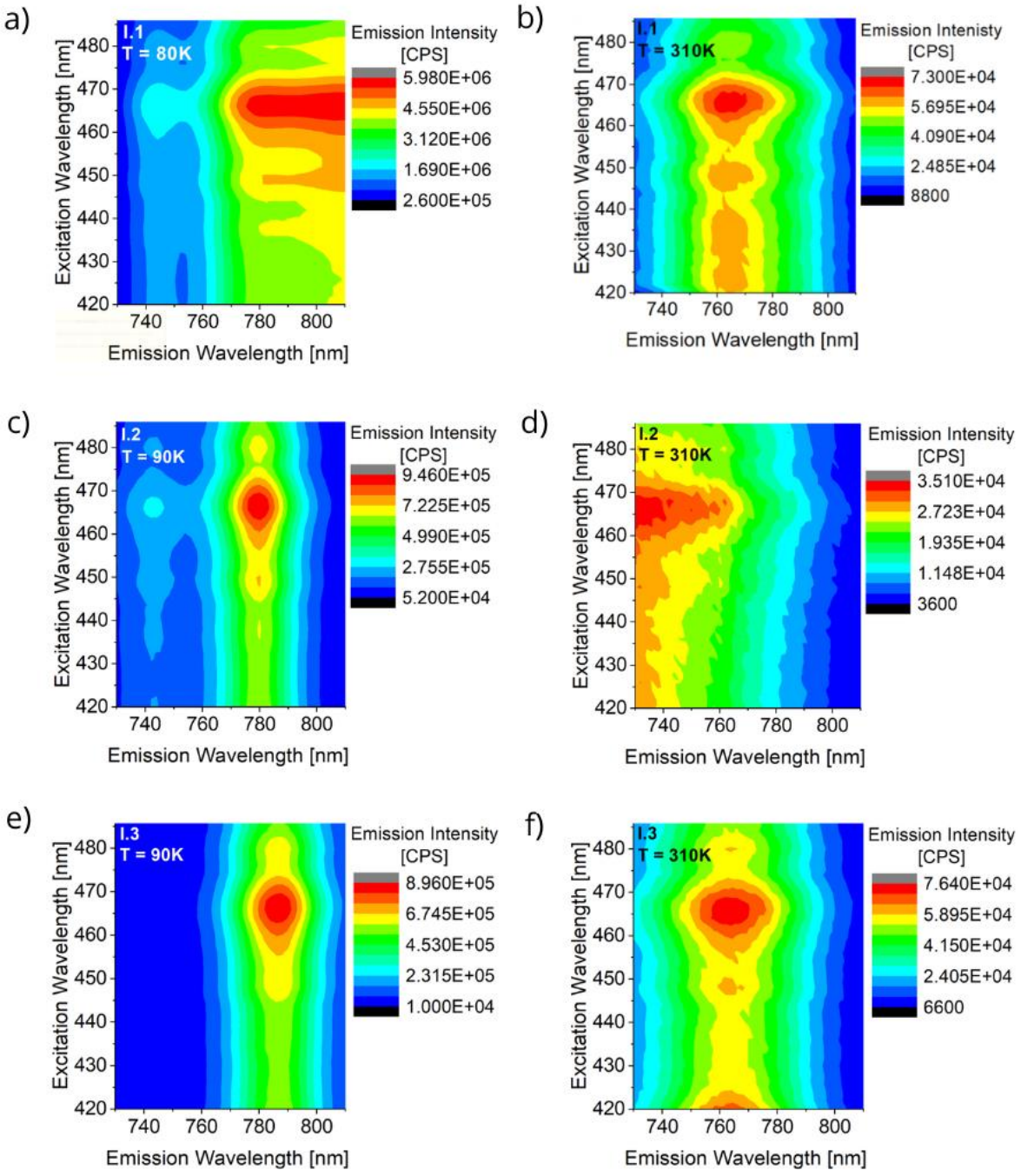

Figure 4.22. Experimental 3D photoluminescence spectra of perovskite thin films I.1 (a, b), I.2 (c, d), I.3 (e, f) for temperatures of 80 K, 90 K, 310 K.

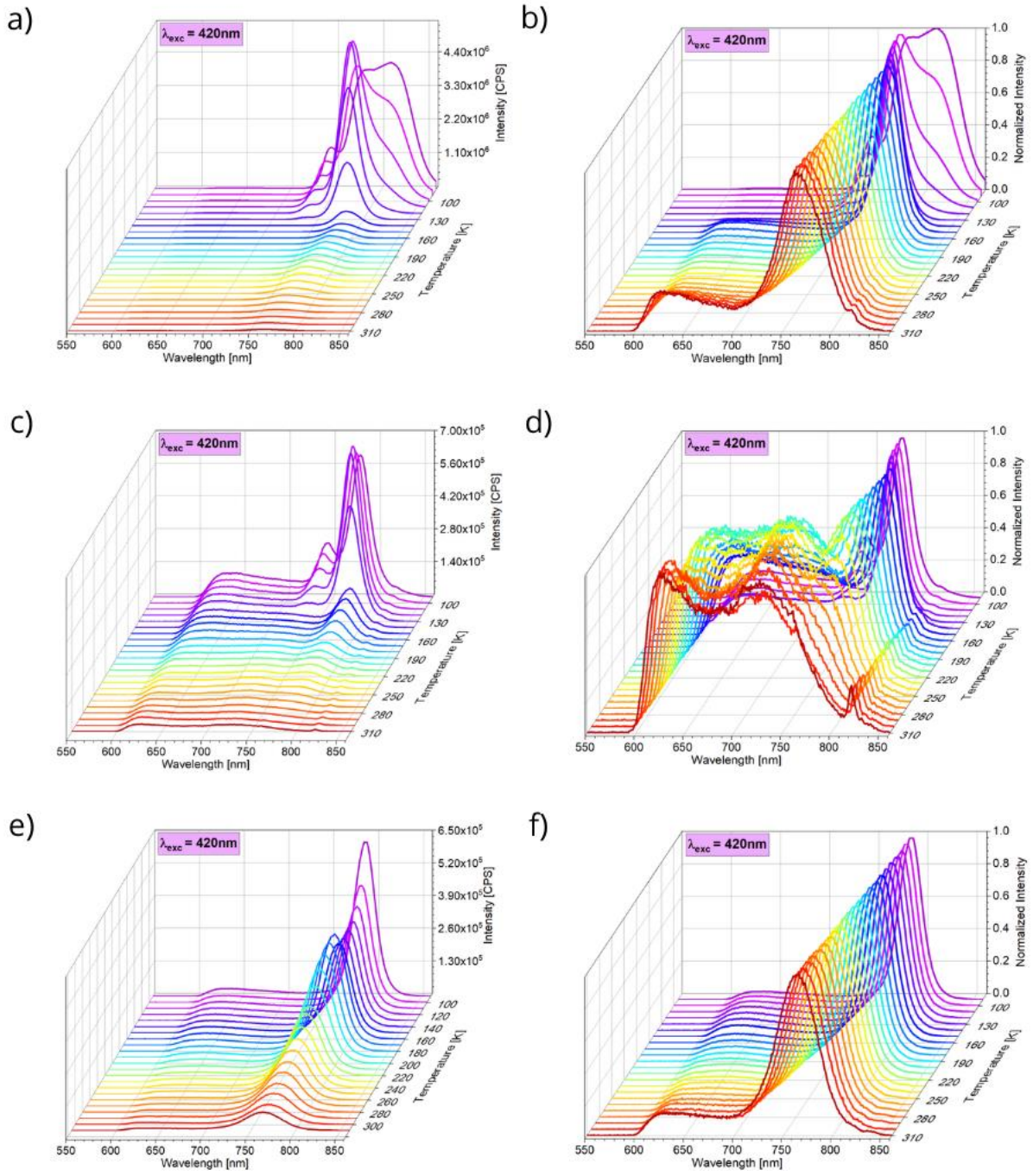

Figure 4.23. Experimental photoluminescence spectra of perovskite thin films I.1 (a, b), I.2 (c, d), I.3 (e, f) as a function of temperature 90 - 310 K. The image shows spectra obtained directly from the measurement and normalized spectra. Excitation wavelength λ_{exc} = 420 nm.

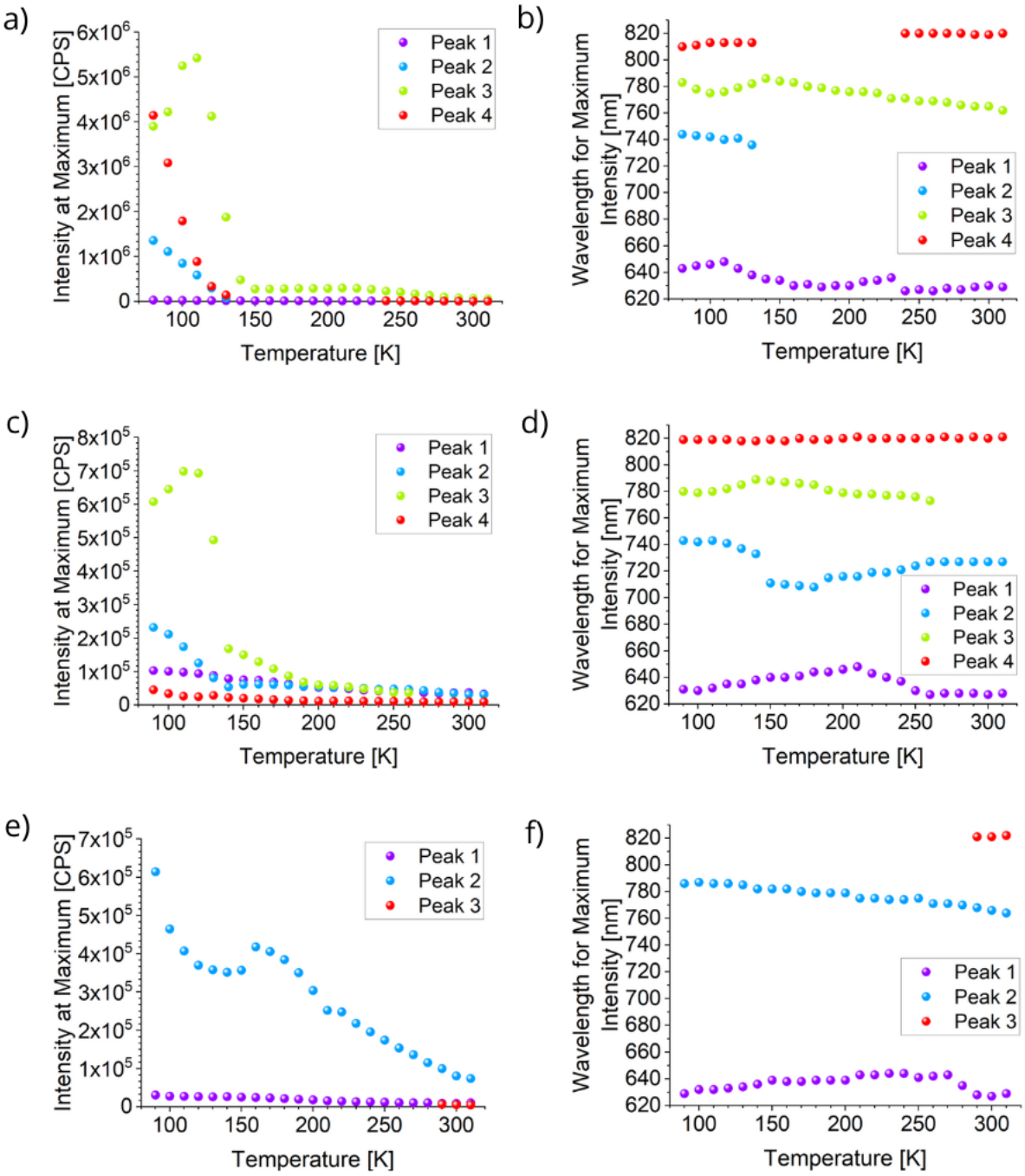

Figure 4.24. The dependence of the maximum intensity of the peaks observed in PL spectra and the position of these peaks as a function of temperature: I.1 (a, b), I.2 (c, d), I.3 (e, f).

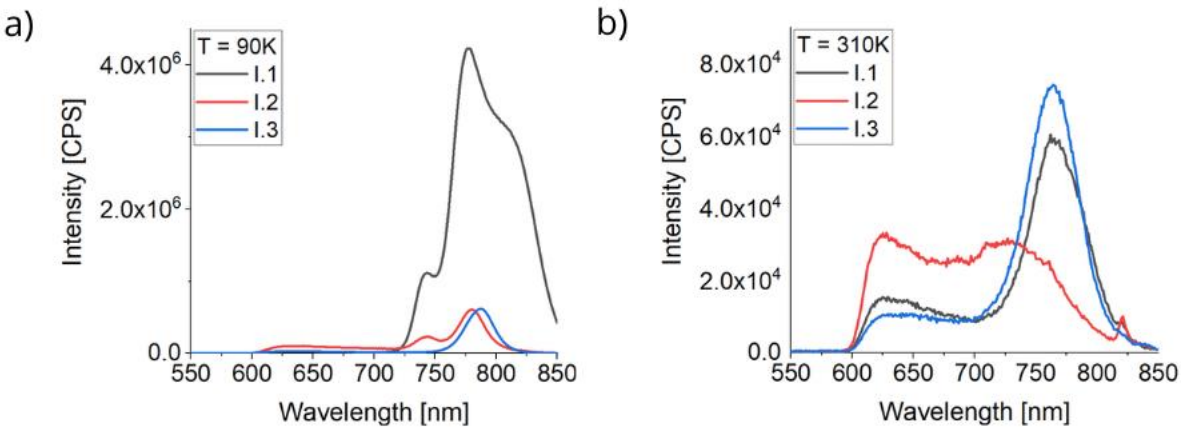

Figure 4.25. Comparison of photoluminescence spectra for minimum and maximum temperatures from the selected temperature range for materials I.1-I.3: T = 90 K (a), T = 310 K (b).

Table 4.12. Phase transition temperatures of materials I.1-I.3 determined from UV-VIS-NIR spectroscopy and PL measurements as a function of temperature.

ID	Phase transition based on		Phase transition
	UV-VIS-NIR (T)	PL (T)	
I.1	120 – 150 K	140 K	From orthorhombic to tetragonal
I.2	Not found	140K	From orthorhombic to tetragonal
I.3	~140 K	140 – 160 K	From orthorhombic to tetragonal
	310K	~RT	From tetragonal to cubic

4.6.2. Chloride perovskites

The results of transmission measurements of the Cl.1-Cl.3 samples are shown in Figure 4.26. All the studied perovskite compositions containing chloride anion showed interesting changes in the transmission spectra, from which the phase transitions from orthorhombic to tetragonal and from tetragonal to cubic phases were determined. A gentle shifting of the spectrum in the wavelength range studied is observed, while the most interesting changes in the spectra occur in the areas from 380 nm to 440 nm (sample Cl.1), from 330 nm to 420 nm (sample Cl.2) and from 310 – 410 nm (sample Cl.3). Based on the observed changes, the temperature specific

points at which the phase transitions of the studied materials occur were determined (Table 4.13).

The peak around 410 nm in the Cl.1 spectrum initially shifts to the left towards shorter wavelengths, and its intensity increases slightly with increasing temperature. At 160 K, a change occurs - the peak intensity starts to decrease, which has been linked to the transition from the orthorhombic to the tetragonal phase. In the Cl.2 material, based on changes in the UV-VIS-NIR spectrum, two phase transitions occur at ~100 K and 280 K. Barely noticeable changes occur in the spectrum - at ~100 K, there is a change in the direction of the spectral shift, and at 280 K, a more dynamic shift of the peak around 390 nm is noticeable. The Cl.3 composition also shows two phase transitions. In the temperature range 160 - 200 K, where a change in peak intensity ~385 nm and a decrease in valley depth ~400 nm are observed, the orthorhombic and tetragonal phases can coexist. A second phase transition confirmed by a spectral change around 400 nm is observed at 280 K.

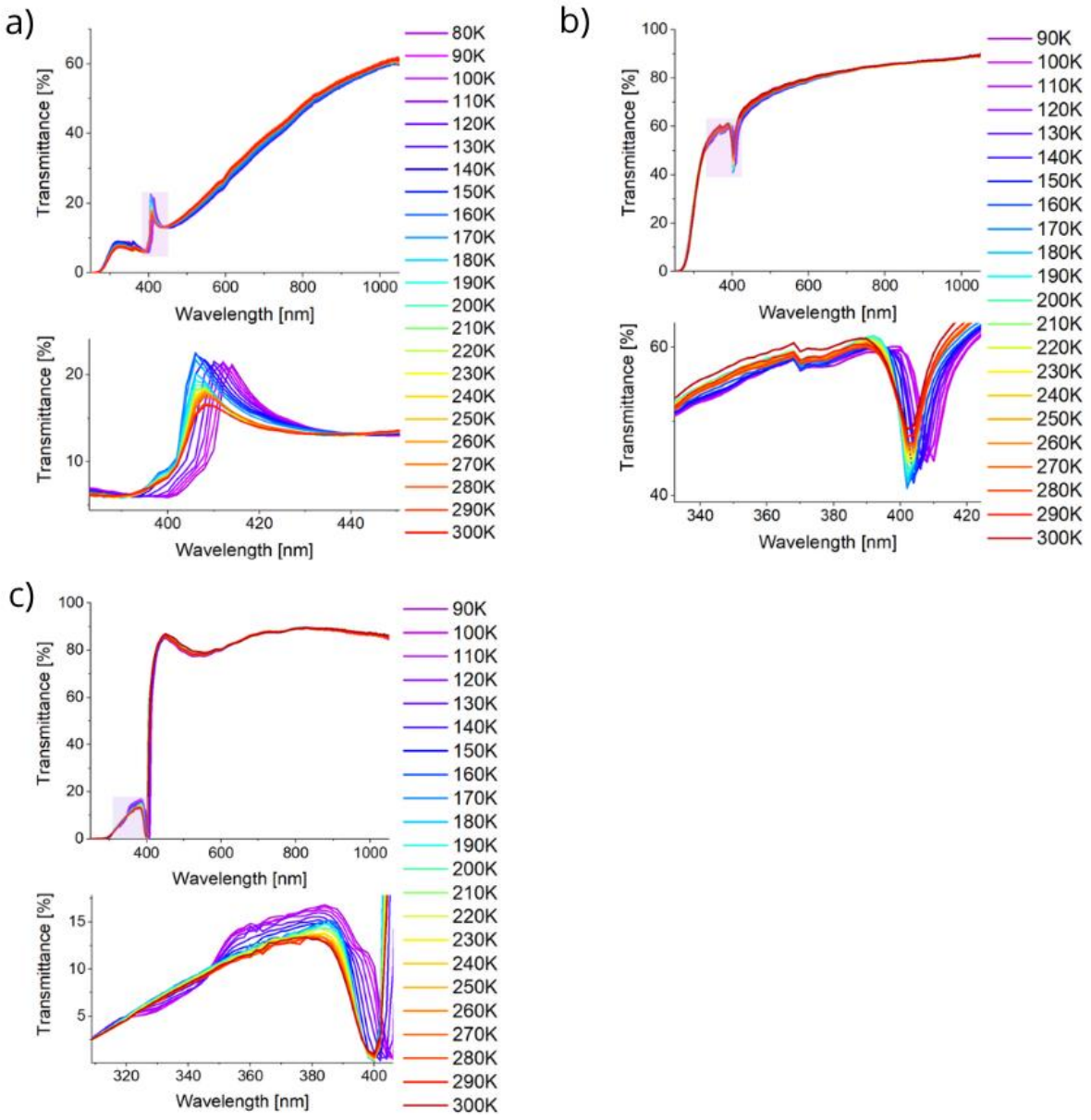

Figure 4.26. UV-VIS-NIR transmission spectra of Cl.1-Cl.3 perovskite thin films as a function of temperature: Cl.1 (a), Cl.2 (b), Cl.3 (c). Shaded areas have been magnified.

For the PL measurements, initial measurements were carried out to determine the excitation wavelength. To maintain the same measurement conditions for the three different perovskite compositions Cl.1 - Cl.3, a single common excitation wavelength of 350 nm was chosen. The results of the tests and analysis are provided in Figure 4.27-29. The graphs in Figure 4.28 indicate the intensity of the peaks appearing in the spectrum and their position as a function of temperature. The collected data from PL measurements indicate the presence of two phase

transitions for all tested chlorine-containing samples Cl.1-Cl.3. For sample Cl.1, the first phase transition was identified at the temperature range of 130 – 150 K. This is the only range where the intensity of Peak 2 increases, while outside this range the intensity decreases. The second phase transition was determined at a temperature of ~230 K, where Peak 1 appears at around a wavelength of 400 nm. In the case of sample Cl.2, phase transitions were observed at ~100 K and 280 K. The first transition temperature was determined based on the most significant change in the intensity of Peak 1. The second phase transition at 280 K is confirmed by the decrease in the intensity of all Peaks observed in the PL spectrum. For sample Cl.3, the first phase transition temperature was determined at ~190 K. This is where two additional peaks appear in the observed PL spectra. The second phase transition is observed at a temperature of 280 K, where the intensity of all observed Peaks significantly increases. The PL spectra intensities at both low and high temperatures are compared for all Cl.1-Cl.3 samples, with Cl.3 showing the highest intensity at low and high temperatures, and Cl.2 the lowest.

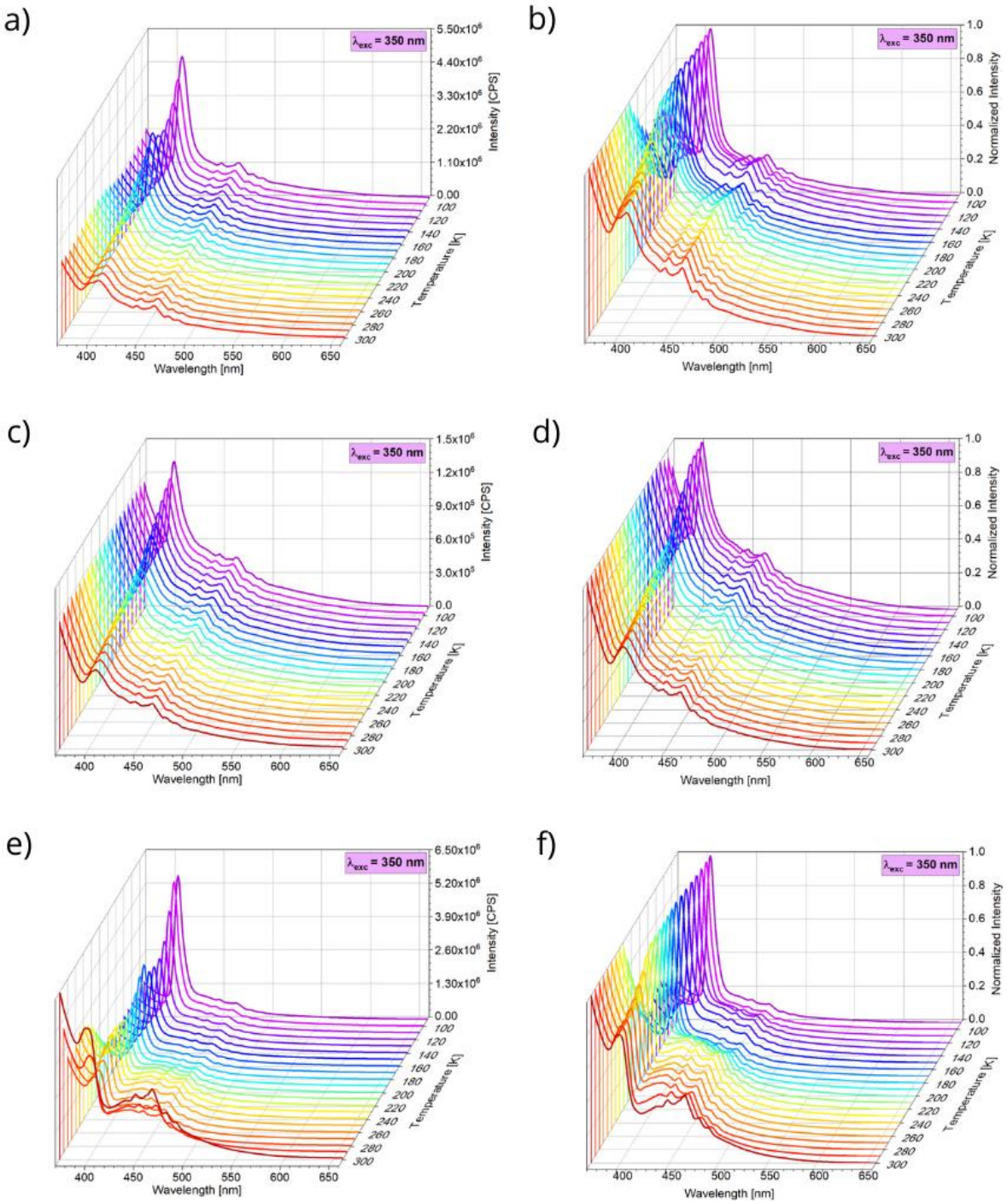

Figure 4.27. Experimental photoluminescence spectra of Cl.1 (a, b), Cl.2 (c, d), Cl.3 (e, f) perovskite thin films as a function of temperature 90 - 300 K. The image shows the spectra obtained directly from the measurement and the normalized spectra. Excitation wavelength λ_{exc} = 350 nm.

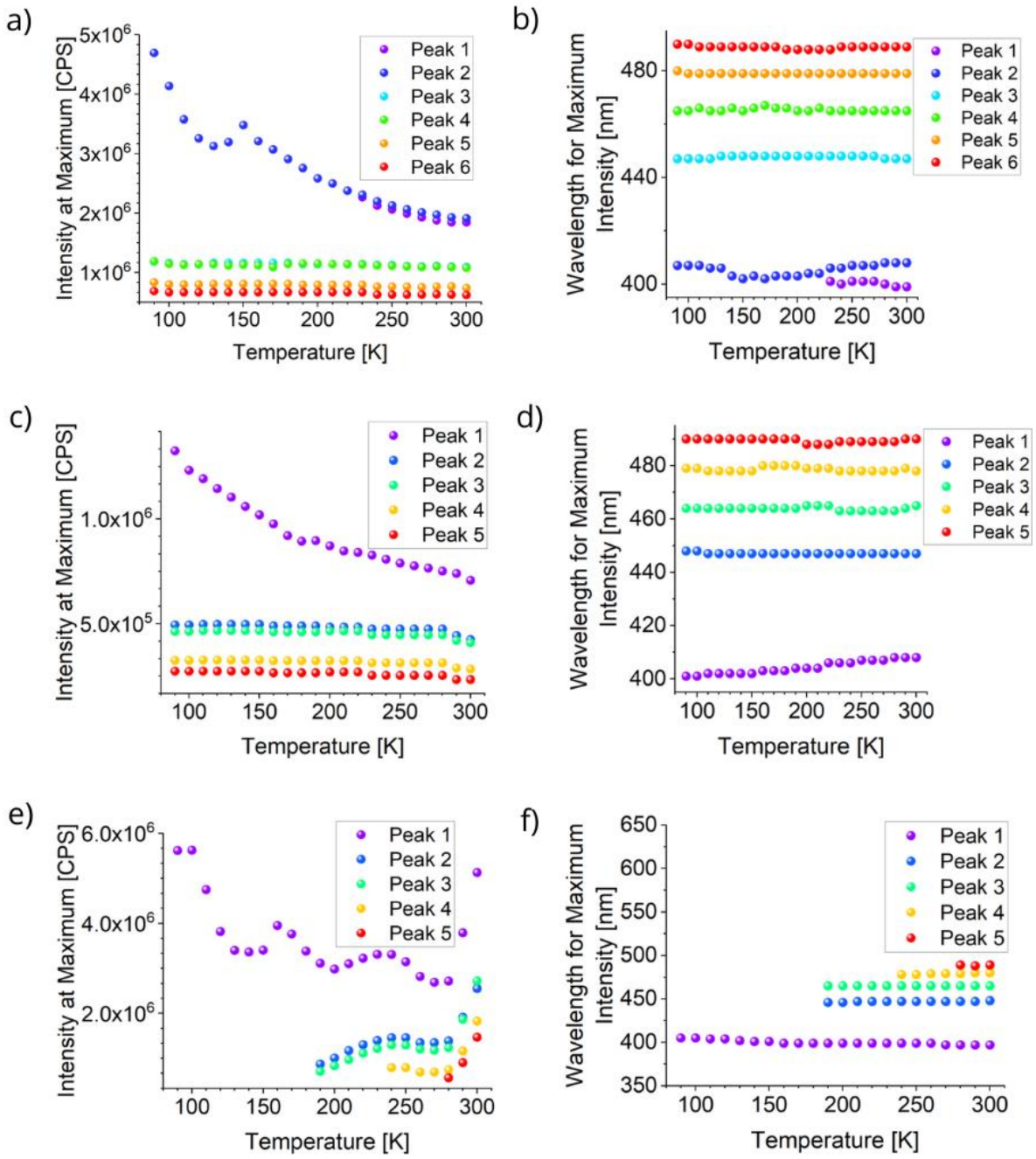

Figure 4.28. Dependence of the maximum intensity of the peaks observed in PL spectra and the position of these peaks as a function of temperature: Cl.1 (a, b), Cl.2 (c, d), Cl.3 (e, f).

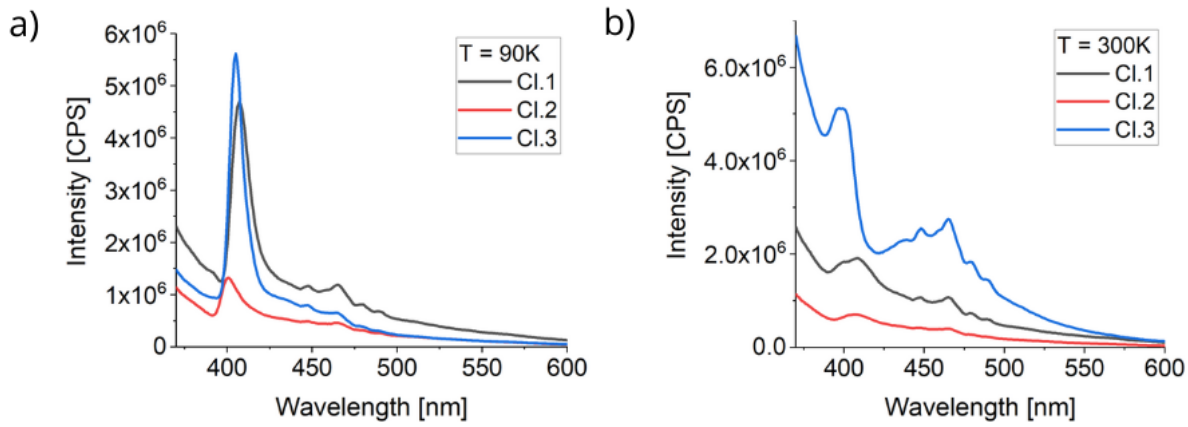

Figure 4.29. Comparison of photoluminescence spectra for minimum and maximum temperatures from the chosen temperature range for the materials Cl.1-Cl.3: T = 90 K (a), T = 300 K (b).

Table 4.13. Phase transition temperatures of Cl.1-Cl.3 materials determined from UV-VIS-NIR spectroscopy and PL measurements as a function of temperature.

ID	Phase transition based on		Phase transition
	UV-VIS-NIR (T)	PL (T)	
Cl.1	160 K	130 - 150 K	From orthorhombic to tetragonal
	Not found	~230 K	From tetragonal to cubic
Cl.2	~100 K	~100 K	From orthorhombic to tetragonal
	280 K	280 K	From tetragonal to cubic
Cl.3	160 – 200 K	~190 K	From orthorhombic to tetragonal
	280 K	280 K	From tetragonal to cubic

4.6.3. Bromide perovskites

The presented transmission results of the Br.1-Br.3 samples are shown in Figure 4.30. Only one of the Br.3 perovskite compositions tested showed interesting changes in the transmission spectrum, from which the phase transitions were determined - at 110 K from orthorhombic to tetragonal phase and at 240 K from tetragonal to cubic phase. The temperatures indicated are the locations where there is a change in valley depth around

540 nm and 550 nm. In both cases, the valley becomes increasingly shallow (the spectrum shifts direction and increases in intensity).

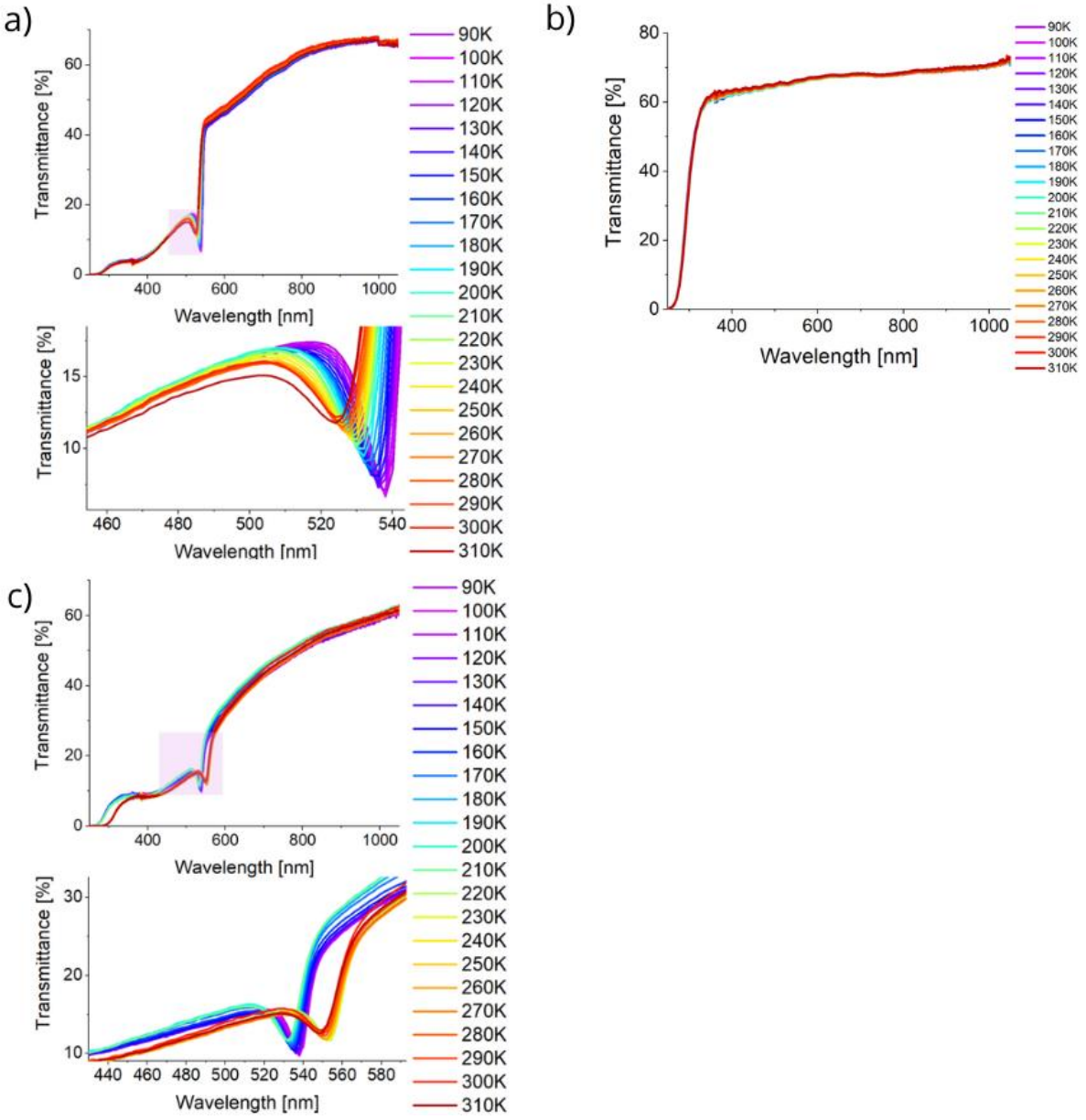

Figure 4.30. UV-VIS-NIR transmission spectra of Br.1-Br.3 perovskite thin films as a function of temperature: Br.1 (a), Br.2 (b), Br.3 (c). Shaded areas have been magnified.

For the PL measurements, initial measurements were carried out to determine the excitation wavelength (Figure 4.31). To maintain the same measurement conditions and the same slit for the three different perovskite compositions Br.1-Br.3, a single common excitation

wavelength of 420 nm was chosen. The results of testing and analysis are presented in Figure 4.32-34. The graphs in Figure 4.33 indicate the intensity of the peaks appearing in the spectrum and their position as a function of temperature. Based on the data obtained, two phase transitions were determined for all samples (Table 4.14). For Br.1, the transitions for temperatures of ~110 K and ~250 K were determined based on a step change in the position of Peak 1 and the appearance of an additional Peak 2 in the spectrum. In the Br.2 material, phase transitions were observed at ~110 K and ~300 K. Sample Br.3 exhibits phase transitions at temperatures of approximately 160 K and 300 K. The first phase transition is evidenced by the disappearance of Peak 2 and a marked decrease in the intensity of Peak 1. The second phase transition is indicated by an increase in the intensity of Peak 1 at 300 K, accompanied by a shift of the maximum of Peak 2 toward longer wavelengths. Figure 4.34 compares the PL spectra of all samples with the bromide anion at 90 K and 310 K. At low temperatures, the PL spectra of samples Br.1 and Br.2 exhibit similar intensities. The intensity of the Br.3 spectrum at low temperature is nearly an order of magnitude lower than that of the other Br materials. At high temperatures, the most intense spectrum is observed for Br.2, while the PL intensity of Br.3 is approximately 4 times lower than that of Br.2.

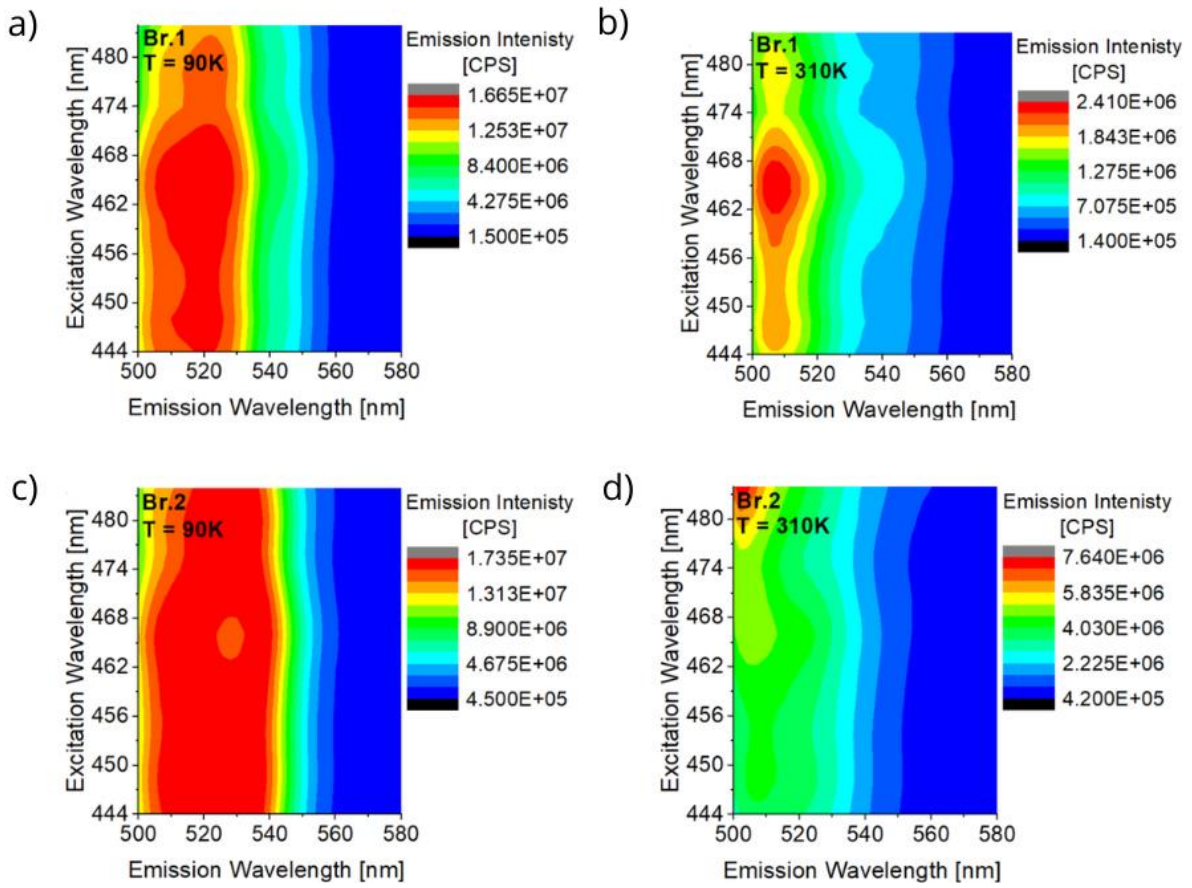

Figure 4.31. Experimental 3D photoluminescence spectra of Br.1 (a, b), Br.2 (c, d) perovskite thin films for temperatures of 90 K, 310 K.

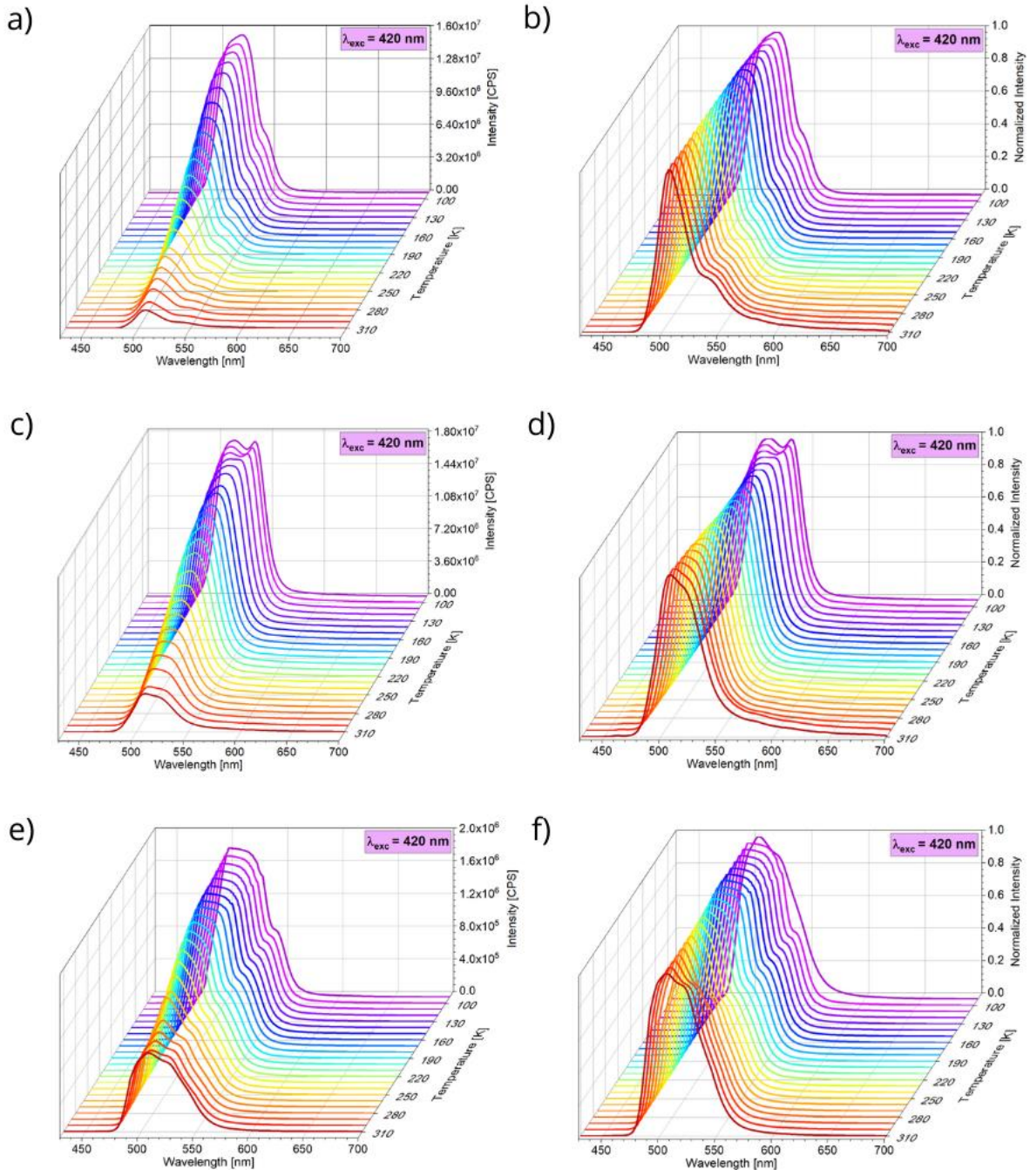

Figure 4.32. Experimental photoluminescence spectra of perovskite thin films Br.1 (a, b), Br.2 (c, d), Br.3 (e, f) as a function of temperature 90 - 310 K. The image shows the spectra obtained directly from the measurement and the normalized spectra. Excitation wavelength λ_{exc} = 420 nm.

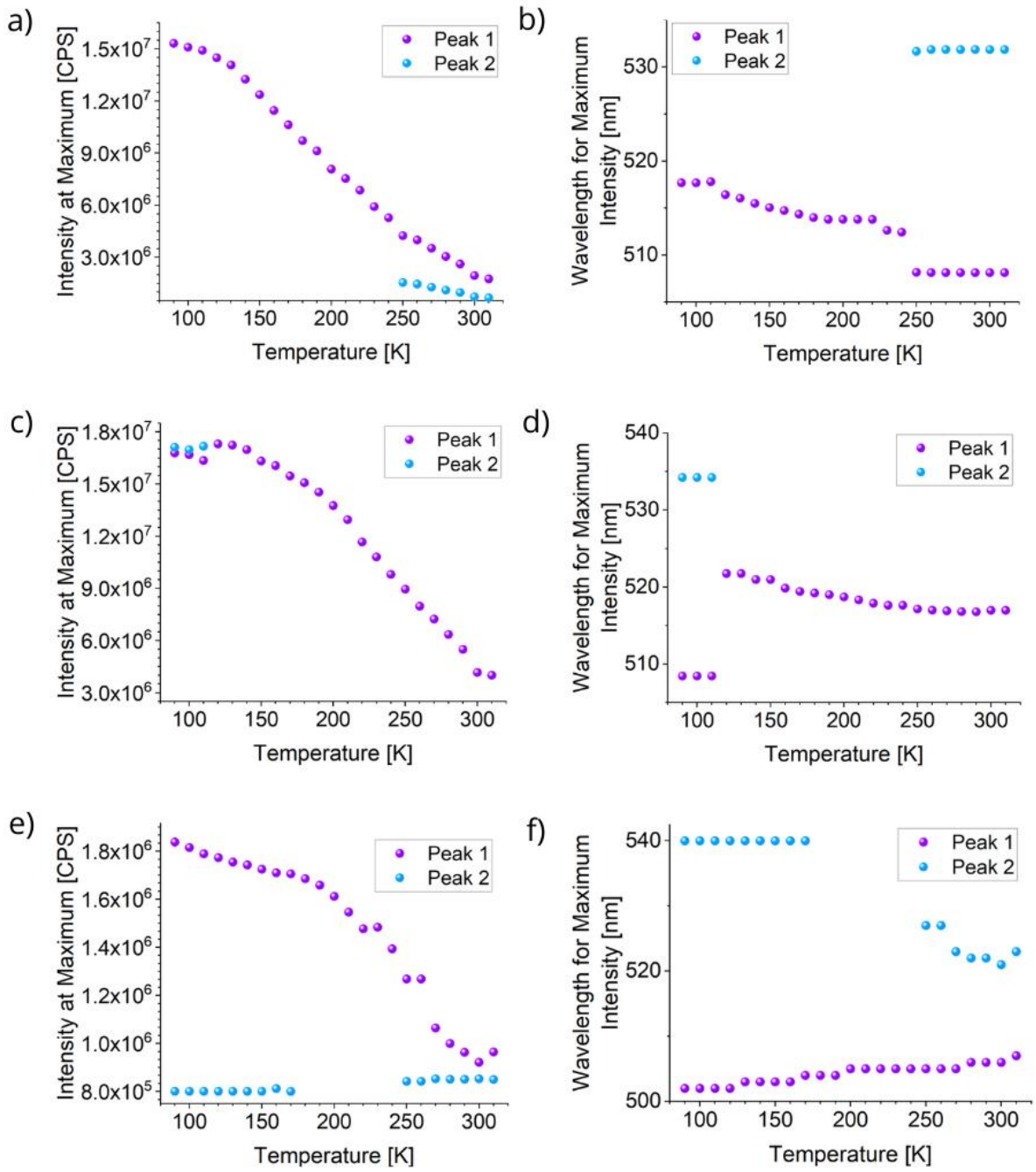

Figure 4.33. Dependence of the maximum intensity of the peaks observed in PL spectra and the position of these peaks as a function of temperature: Br.1 (a, b), Br.2 (c, d), Br.3 (e, f).

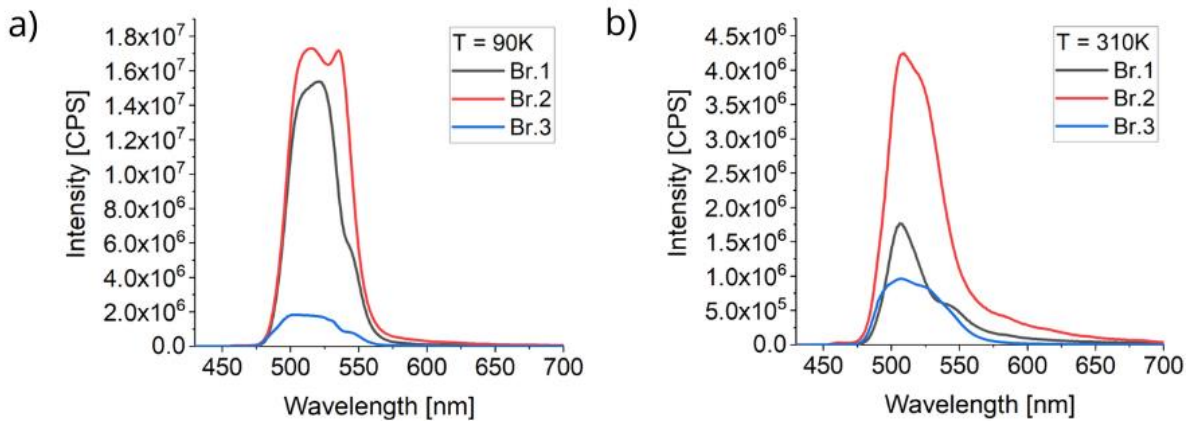

Figure 4.34. Comparison of photoluminescence spectra for minimum and maximum temperatures from the chosen temperature range for materials Br.1-Br.3: T = 90 K (a), T = 310 K (b).

Table 4.14. Phase transition temperatures of materials Br.1-Br.3 determined from UV-VIS-NIR spectroscopy and PL measurements as a function of temperature.

ID	Phase transition based on		Phase transition
	UV-VIS-NIR (T)	PL (T)	
Br.1	Not found	~110 K	From orthorhombic to tetragonal
	Not found	~250 K	From tetragonal to cubic
Br.2	Not found	~110 K	From orthorhombic to tetragonal
	Not found	~300 K	From tetragonal to cubic
Br.3	110 K	~160 K	From orthorhombic to tetragonal
	240 K	300 K	From tetragonal to cubic

4.6.4. Conclusions

The data results above provide information on the temperatures at which phase transitions occur in the perovskite materials studied. Phase transitions were determined from the transmission and PL spectra changes observed over a wide temperature range. Transition temperatures were indicated separately from transmission and PL measurements. The results are summarized in Table 4.12-14. Phase transitions - from orthorhombic to tetragonal and from tetragonal to cubic phases - occur in all the materials studied.

For samples I.2, Br.1, and Br.2, no phase changes could be found based on transmission measurements, while phase changes were detected in measurements of PL spectra. For the phase transition temperatures indicated by the two measurement techniques, a high degree of agreement can be seen, with emerging discrepancies generally not exceeding 10 K (except in the case of Br.3). Sources report that the perovskite material can adopt an orthorhombic, tetragonal, or cubic phase. Various dissertations relating to the crystal structure report phase transitions of iodide perovskite materials occurring at 160 K (transition from the orthorhombic to the tetragonal phase) and 330 K (transition from the tetragonal to cubic phase) [16,17]. The results obtained from PL spectra of iodide perovskites are similar to those presented in the work [18], in which the transition from the orthorhombic to the tetragonal phase occurs in the range 120 - 150 K.

4.7. Studies of nonlinear optical effects

Nonlinear optical effects were studied for all perovskite thin films with iodine, chlorine, and bromine. The apparatus described in *Sections 3.5*, *3.8,* and *3.9* was used for the measurements. SHG and THG were analyzed using the Lee (SHG) and Kubodera-Kobayashi (THG) theoretical Models, used in thin film analysis, and consider linear absorption coefficients.

4.7.1. Second Harmonic Generation

SHG measurements were carried out with two laser light polarization configurations (S-P and P-P). Most of the materials tested did not exhibit second-order nonlinear optical effects, so the Corona Poling (CP) technique was used to obtain the uniaxial orientation of the molecules. The polarization temperature in CP was set at 95 °C, and the applied voltage at 7 $\frac{kV}{cm}$. SHG measurements were performed again after the CP was applied. For selected materials, measurements were repeated after 2 weeks.

4.7.1.1. Iodide perovskites

Figure 4.35 shows the SHG signals after applying the CP technique as a function of rotation angle for selected perovskite materials with iodine I.1-I.3. Comparing the SHG signals, it was noted that their intensity did not differ significantly. The strongest second-order nonlinear response was obtained for sample I.2 in P-P polarization, while the weakest response was also obtained for this material, but in S-P polarization (Table 4.15). Relating the obtained results to the compositions of materials I.1-I.3, one can observe the dependence of the $\chi^{(2)}$ value on the content of the organic part MAI, and the inorganic part PbI_2. With an increase in the PbI_2 content and, at the same time, with a decrease in the MAI content, the $\chi^{(2)}$ value increases. In the group of perovskites with iodine, SHG was observed in five of the seven samples tested. Second-order nonlinear effects were not exhibited by materials I.5 and I.7 even after the application of CP. The weakest second-order response has I.4. Comparing the results obtained with the second-order nonlinear susceptibility of the reference material, quartz, it can be seen that perovskites with iodine generate signals generally lower than the reference material. The standout material among those presented here is I.2, whose $\chi^{(2)}$ after CP increased by 2.5 times compared to the reference material.

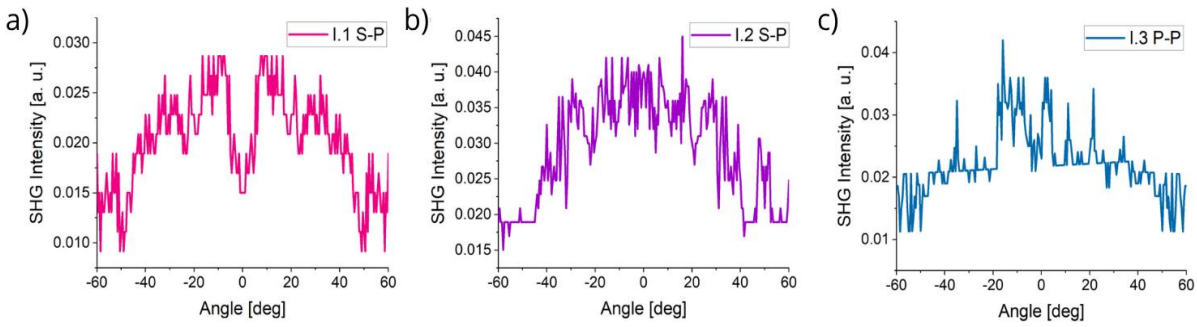

Figure 4.35. SHG intensity after CP as a function of rotation angle in a laser beam with S-P or P-P polarization for materials I.1-I.3.

Table 4.15. Second-order nonlinear susceptibility values of perovskites I.1-I.7 before and after application of the Corona Poling (CP) technique, calculated with the help of the theoretical Lee Model.

ID	$\chi^{(2)}\left[\frac{pm}{V}\right]$			
	Before CP		After CP	
	S-P	P-P	S-P	P-P
	Directly			
I.1	-	1.052±0.302	0.580±0.201	-
I.2	-	-	0.483±0.139	2.522±0.113
I.3	-	-	-	0.679±0.273
I.4	-	-	0.057±0.005	-
I.5	-	-	-	-
I.6	-	-	-	0.485±0.195
I.7	-	-	-	-
Quartz (reference sample)	1			

4.7.1.2. Chloride perovskites

Figure 4.36 shows the SHG signals as a function of rotation angle for selected Cl.1-Cl.3 chloride perovskite materials obtained two weeks after the CP technique. In contrast, Table 4.16 collects the $\chi^{(2)}$ results. The first observation is that the materials in this group did not show nonlinear optical effects before the application of CP. After applying CP, samples Cl.1 and Cl.3 showed second-order nonlinear behaviour reaching values up to 7.5 times higher than the reference material. Sample Cl.2 did not show second-order nonlinear behaviour in this measurement series. The SHG measurement was repeated after two weeks. This time, second-order optical nonlinearity was demonstrated by all three materials in the S-P laser beam polarization. After two weeks of CP, the $\chi^{(2)}$ value of sample Cl.1 remained similar, and sample Cl.3 showed an $\chi^{(2)}$ about 15 times lower than in the first measurement series. Interestingly, the Cl.2 sample in the second series of measurements showed second-order optical nonlinearity. This surprising behaviour may be due to the fact that chloride perovskite materials are transparent and unstable,

so there is a chance that an inappropriate site, lacking sufficient material to observe the nonlinearity, was chosen for the first series of measurements. An interesting observation is the dependence of the $\chi^{(2)}$ value on the composition of the Cl.1-Cl.3 samples. As the $PbCl_2$ content increases and, simultaneously, as the MACl content decreases, the $\chi^{(2)}$ value increases.

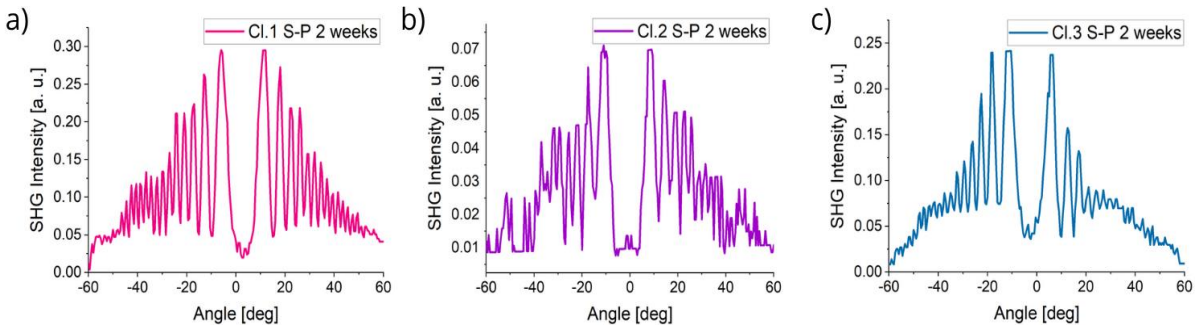

Figure 4.36. SHG intensity after CP application as a function of rotation angle in the S-P polarized laser beam for Cl.1-Cl.3 materials. The graphs show the results of measurements taken two weeks after the first measurement and CP application.

Table 4.16. Second-order nonlinear susceptibility values of Cl.1-Cl.3 perovskites after applying the Corona Poling (CP) technique, calculated with the theoretical Lee Model.

ID	$\chi^{(2)}\left[\frac{pm}{V}\right]$ After CP			
	S-P	P-P	S-P	P-P
	Directly		2 weeks later	
Cl.1	0.524±0.038	7.571±3.790	0.508±0.038	-
Cl.2	-	-	0.316±0.045	-
Cl.3	7.599±3.051	-	0.589±0.031	-
Quartz (reference sample)	1			

4.7.1.3. Bromide perovskites

Figure 4.37 shows the SHG signals after application of the CP technique as a function of rotation angle for selected perovskite materials with bromine Br.1-Br.3. Comparing the SHG signals in Figure 4.37, it is noted that their intensity does not differ significantly for the Br.1-Br.3 samples, which is confirmed by the numerical $\chi^{(2)}$ results obtained in Table 4.17. Before application of the CP technique, second-order nonlinear effects were exhibited by three of the four materials tested, i.e., Br.1-Br.3. The values obtained for these materials were close to the $\chi^{(2)}$ values of the reference material. After the application of CP, all four samples responded nonlinearly. The $\chi^{(2)}$ values after CP are higher, confirming that the uniaxial orientation of the molecules is crucial to improve second-order nonlinear effects. SHG measurements were repeated after two weeks. The results obtained after this time are lower than the first time, as seen in Table 4.17. The most significant decrease in $\chi^{(2)}$ was observed for Br.4. The $\chi^{(2)}$ results obtained approximate or exceed the $\chi^{(2)}$ of the reference material.

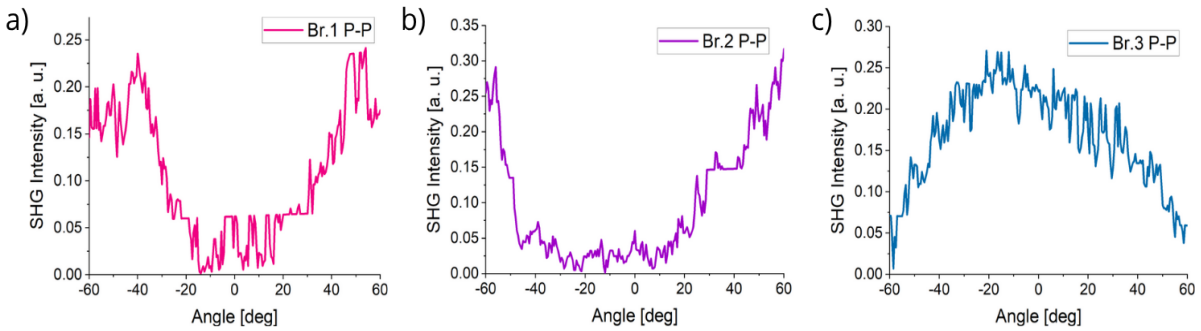

Figure 4.37. SHG intensity after CP as a function of rotation angle in a P-P polarized laser beam for materials Br.1-Br.3.

Table 4.17. Second-order nonlinear susceptibility values of Br.1-Br.4 perovskites before and after application of the Corona Poling (CP) technique, calculated with the help of the theoretical Lee Model.

ID	$\chi^{(2)}\left[\frac{pm}{V}\right]$					
	Before CP		After CP			
	S-P	P-P	S-P	P-P	S-P	P-P
	Directly				2 weeks later	
Br.1	0.584±0.088	1.403±0.068	1.502±0.062	1.422±0.077	-	1.046±0.088
Br.2	-	1.215±0.067	0.961±0.055	1.454±0.070	-	1.055±0.076
Br.3	0.954±0.057	-	1.229±0.056	1.853±0.076	-	1.419±0.072
Br.4	-	-	-	1.627±0.054	-	0.603±0.087
Quartz (reference sample)	1					

4.7.2. Third Harmonic Generation

Measurements of third-order nonlinear optical effects due to the polarization independence of THG were made in the S-P laser beam polarization configuration. The CP technique was not used in this part of the study.

4.7.2.1. Iodide perovskites

Figure 4.38 shows the THG intensity as a function of incidence angle for selected materials I.1-I.3. Calculated with the help of the Kubodera-Kobayashi Model, the $\chi^{(3)}$ values are given in Table 4.18. All materials exhibited third-order optical nonlinearity, and the values obtained significantly exceeded those of the reference sample, even by more than 100 times. The strongest THG effect was shown by sample I.3 reaching $\chi^{(3)} = (209.80 \pm 7.66) \cdot 10^{-22}\ \frac{m^2}{V^2}$, and the weakest by sample I.6, for which $\chi^{(3)} = (31.77 \pm 1.23) \cdot 10^{-22}\ \frac{m^2}{V^2}$.

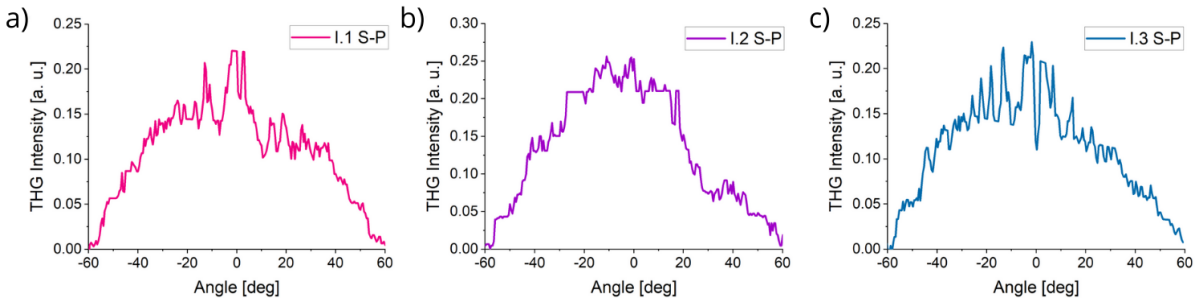

Figure 4.38. THG intensity as a function of incidence angle of an S-P polarized laser beam for materials I.1-I.3.

Table 4.18. Third-order nonlinear susceptibility values of perovskites I.1-I.7 calculated with the help of the Kubodera-Kobayashi Model.

ID	$\chi^{(3)}\left[10^{-22}\ \frac{m^2}{V^2}\right]$
I.1	64.24±2.42
I.2	124.40±4.53
I.3	209.80±7.66
I.4	75.34±4.47
I.5	88.48±12.60
I.6	31.77±1.23
I.7	42.80±2.08
Silica (reference sample)	2

4.7.2.2. Chloride perovskites

Figure 4.39 shows the THG intensity as a function of incidence angle for samples Cl.1-Cl.3. Calculated with the help of the Kubodera-Kobayashi Model, the $\chi^{(3)}$ values are given in Table 4.19. All materials exhibited third-order optical nonlinearity, and the values obtained were significantly higher than those of the reference sample. The strongest THG effect was shown by sample Cl.1, reaching $\chi^{(3)} = (421.90 \pm 22.61) \cdot 10^{-22}\ \frac{m^2}{V^2}$, and the weakest by sample Cl.2, for which $\chi^{(3)} = (58.95 \pm 3.51) \cdot 10^{-22}\ \frac{m^2}{V^2}$. In turn, comparing the THG intensities in Figure 4.39, it can be seen that they are not significantly different.

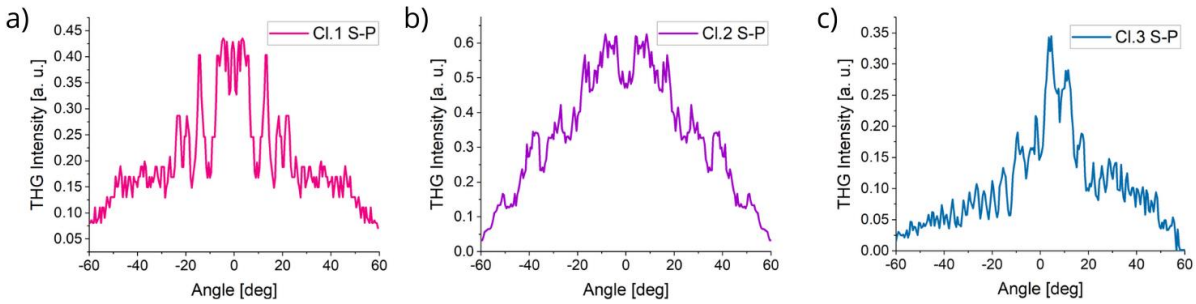

Figure 4.39. THG intensity as a function of incidence angle of an S-P polarized laser beam for Cl.1-Cl.3 materials.

Table 4.19. Third-order nonlinear susceptibility values of Cl.1-Cl.3 perovskites calculated with the Kubodera-Kobayashi Model.

ID	$\chi^{(3)}\left[10^{-22}\,\frac{m^2}{V^2}\right]$
Cl.1	421.90±22.61
Cl.2	58.95±3.51
Cl.3	260.62±14.01
Silica (reference sample)	2

4.7.2.3. Bromide perovskites

Figure 4.40 plots the dependence of the THG signal as a function of the incidence angle of the laser beam for samples Br.1-Br.3. Noting the intensities, the THG signal of sample Br.1 has the highest, and that of Br.2 the lowest. These differences are very well reflected in the $\chi^{(3)}$ results in Table 4.20. The strongest THG effect and the largest value of the third-order nonlinear susceptibility of $(293.30 \pm 25.40) \cdot 10^{-22}\,\frac{m^2}{V^2}$ is shown by material Br.1, while the smallest, equal to $(58.18 \pm 5.22) \cdot 10^{-22}\,\frac{m^2}{V^2}$ is shown by material Br.2. Also, sample Br.4 generates third-order nonlinear optical effects, with a value of $\chi^{(3)} = (80.86 \pm 6.87) \cdot 10^{-22}\,\frac{m^2}{V^2}$. Compared to the reference material, the bromide perovskites exhibit strong optical nonlinearity.

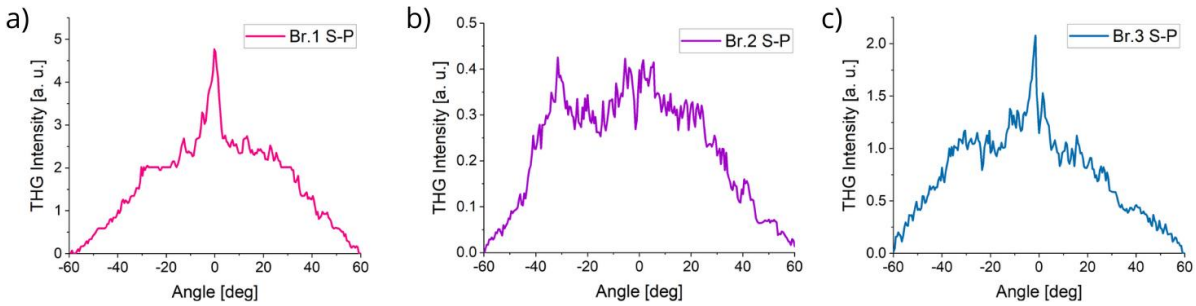

Figure 4.40. THG intensity as a function of incidence angle of an S-P polarized laser beam for Br.1-Br.3 materials.

Table 4.20. Third-order nonlinear susceptibility values of Br.1-Br.4 perovskites calculated with the Kubodera-Kobayashi Model.

ID	$\chi^{(3)}\left[10^{-22}\frac{m^2}{V^2}\right]$
Br.1	293.30±25.40
Br.2	58.18±5.22
Br.3	210.73±18.30
Br.4	80.86±6.87
Silica (reference sample)	2

4.7.3. Z-scan results

Figure 4.41 shows an example of Z-scan measurements, and Table 4.21 collects the nonlinear absorption coefficient values calculated from the recorded data. Z-scan studies were carried out for a laser beam with an energy of 2 μJ. Proper signals could only be obtained for materials I.1, I.4, and Cl.1. In the closed Z-scan configuration, the Cl.1 sample showed a characteristic "peak-to-valley" pattern, indicating a negative nonlinear refractive index. In the open Z-scan configuration, the same sample shows a positive coefficient β, as confirmed by Figure 4.41b. The measurement result of sample I.4 in the open configuration indicates that this material manifests saturable absorption (SA), which is characterized by increased transmission near the focus.

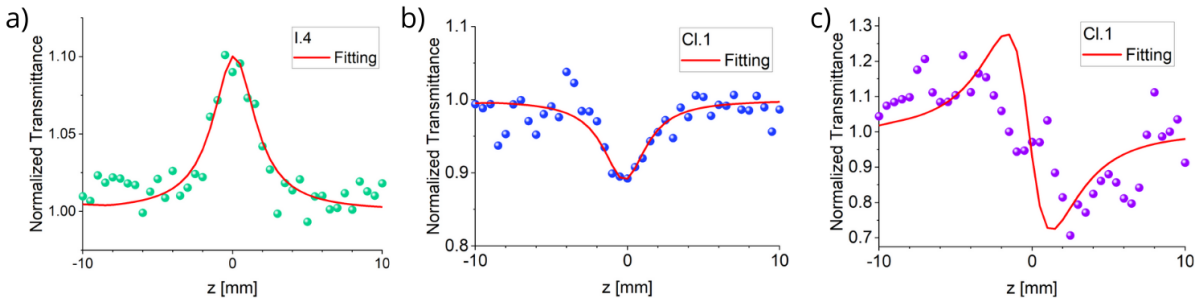

Figure 4.41. Characteristics obtained by an Open Z-scan (a, b) and a Closed Z-scan (c) of I.4 and Cl.1 materials and 2 μJ laser pulse energy.

Table 4.21. Values of the nonlinear absorption coefficient β of materials I.1, I.4-I.7, Cl.1 calculated from measurements carried out using the Z-scan technique.

ID	$\beta\left[10^{-8}\frac{m}{W}\right]$
I.1	-40.00±10%
I.4	-1.20±6%
I.5	-
I.6	-
I.7	-
Cl.1	1.60±2%

4.7.4. Conclusions

The data presented in the chapter describing nonlinear SHG, THG, and Z-scan optical effects confirm that perovskite materials are capable of optical nonlinearity. Second-order nonlinear effects were not observed for materials I.5 and I.7. In contrast, there is information in the available sources about SHG effects also occurring in material I.5 [19,20]. For the other materials, the SHG signals after CP application were small, often smaller than the $\chi^{(2)}$ value of the reference material. The standout materials are the bromine samples, whose calculated $\chi^{(2)}$ values were usually larger than the $\chi^{(2)}$ of the reference material and the most stable temporally. The SHG data show that using the CP technique for the uniaxial orientation of molecules is key to improving the SHG response. Samples are characterized by high $\chi^{(3)}$ values, well above the $\chi^{(3)}$ of the reference material.

For similar perovskite structures $(C_4H_9NH_3)_2PbI_4$ and $CH_3NH_2/PbBr_2$: 1/1, other researchers have investigated that $\chi^{(3)}$ is $3.5 \cdot 10^{-18}\ \frac{m^2}{V^2}$ and $1.25 \cdot 10^{-13}\ \frac{m^2}{V^2}$, respectively [21,22]. Z-scan measurements were carried out only for materials I.1, I.4-I.7, and Cl.1, only three of which provided satisfactory results. From the calculated β coefficient values, it can be seen that perovskite materials with iodide anion show a negative β, which is due to the SA phenomenon. Perovskite with chloride manifests the opposite behaviour - the β parameter is positive, and this is associated with RSA. In the context of RSA, a similar behaviour for Cl.1 material was observed in the work [23].

4.8. Application in photovoltaic cell

The target task in the work presented here, in addition to investigating the structural and optical properties of various perovskite thin films, was to apply them to a photovoltaic cell. Perovskite thin films I.1, Cl.1, and Br.1 were used in a photovoltaic cell, as shown in Figure 4.42a. The structure of the proposed cell consists of four thin layers: an ITO thin layer, acting as a transparent conductive electrode, a SnO_2 layer, an electron transport layer, a perovskite thin layer, which is the active layer that absorbs light, and a Spiro-MeOTAD layer responsible for hole transport. The cell structure was designed according to the principles described in *Section 1.3*. All thin layers were fabricated using the PVD technique and deposited on a transparent BK7 glass substrate with a rectangular shape and 2.5 cm x 3 cm dimensions.

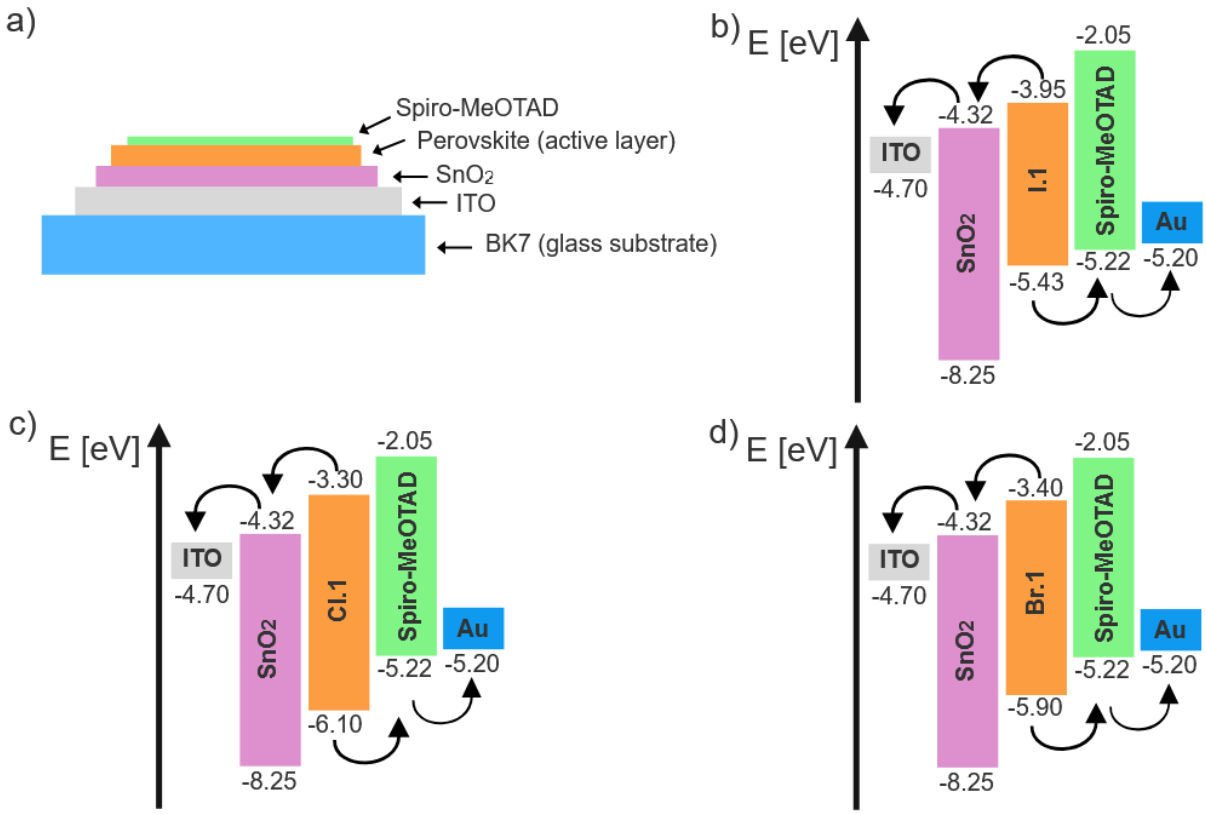

Figure 4.42. Structure of thin film photovoltaic cells with perovskite layers (a) and a schematic of the energy levels of the materials making up the solar cell with I.1 (b), Cl.1 (c), Br.1 (d) perovskites as active layer.

4.8.1. Photovoltaic tests

Characterization tests of the photocells were carried out using the apparatus described in *Sections 3.10* and *3.11*. A negative measuring probe was applied to the ITO thin film, and a positive measuring probe to the top of the photocell, i.e., to the Spiro-MeOTAD layer. The cell thus polarized was illuminated with an LCS-100 sunlight simulator (Oriel), and its response to light was checked. Measurements were carried out at atmospheric pressure and room temperature. The experimentally obtained I-V dark and light characteristics of the cells are presented in Figure 4.43a-c, and the cell characterization parameters calculated from them are given in Table 4.22. Figure 4.43 also includes the experimental power curves of the tested solar cells, and the dark and illuminated I-V characteristics of the individual perovskite thin films forming the given solar cell.

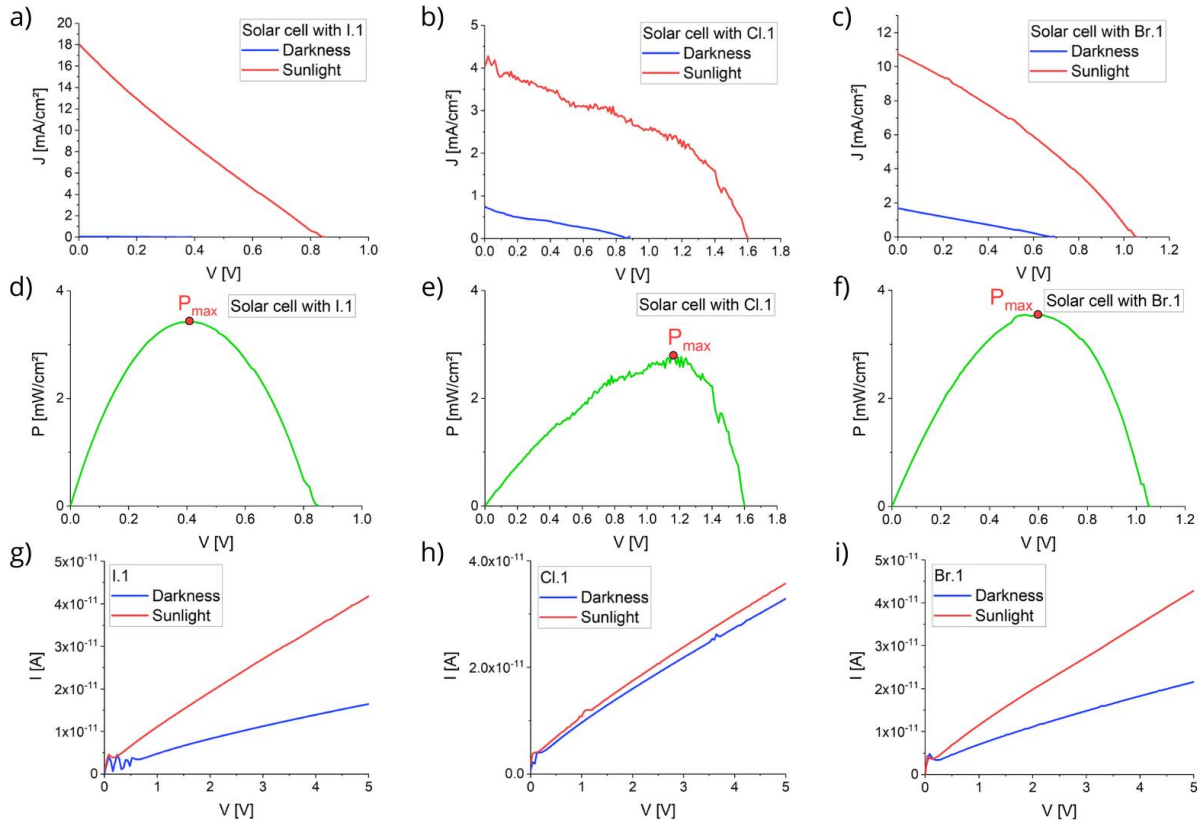

Figure 4.43. Experimental I-V characteristics of tested solar cells with perovskite active layers: I.1, Cl.1, Br.1 (a-c), power curves of these solar cells (d-f), and I-V characteristics of the perovskite thin films forming the given solar cell (g-i).

Table 4.22. Main parameters of perovskite solar cells calculated based on light I-V characteristics.

Perovskite used in tested solar cell	**Solar cells parameters**				
	$V_{OC}[V]$	$J_{SC}\left[\frac{mA}{cm^2}\right]$	$P_{max}\left[\frac{mW}{cm^2}\right]$	FF [%]	η [%]
I.1	0.84	18.06	3.43	22.61	3.43
Cl.1	1.56	4.04	2.80	44.52	2.80
Br.1	1.05	10.76	3.55	31.44	3.55

The effect of illumination on the tested solar cells with different perovskite materials (I.1, Cl.1, Br.1) is evident from the I-V characteristics shown in Figure 4.43a-c. The cells showed a clear response to illumination with simulated sunlight. The obtained values of short-circuit current (J_{SC}) and open-circuit voltage (V_{OC}) are 18.06 $\frac{mA}{cm^2}$ and 0.84 V for the cell with active layer I.1, 4.04 $\frac{mA}{cm^2}$ and 1.56 V for the cell with active layer Cl.1, and 10.76 $\frac{mA}{cm^2}$ and 1.05 V for the cell with active layer Br.1, respectively. Comparing the obtained parameters of the solar cells, with particular attention to the FF parameter, it is evident that the solar cell with Cl.1 achieves the best FF value. This is also confirmed by the shape of the I-V characteristic in Figure 4.43b, which is the most similar to the ideal solar cell characteristic among the three tested solar cells. The second-best FF is achieved by the solar cell with Br.1, and the third by the solar cell with I.1. The influence of series resistance (R_S) and shunt resistance (R_{SH}) is evident in the presented I-V characteristics of the solar cells and has a significant impact on the obtained photovoltaic parameters. Comparing the results obtained here with the theoretical considerations presented in Figure 1.9 (*Chapter 1*), it can be concluded that the photocell with I.1 was characterized by a relatively high R_S, as indicated by the triangular shape of the I-V curve. A considerable R_S value is associated with a reduction of current at higher voltages, a decrease in the FF, and consequently, a reduction in efficiency. The R_S had the most negligible impact on the operation of the cell with Cl.1, while the R_{SH} was the highest in this case, which is confirmed by the shape of the obtained I-V characteristic. The I-V characteristic of the solar cell with Br.1 indicates that its R_S and R_{SH} parameters have an intermediate effect on the device performance compared to the solar cells with I.1 and Cl.1. The calculated efficiencies of the investigated solar cells with I.1, Cl.1, and Br.1, determined from light I-V characteristics, are 3.43%, 2.80%, and 3.55%, respectively. It turns out that the solar cells with I.1 and Br.1, despite exhibiting lower FF values compared to the device with Cl.1, achieve higher efficiencies. This results from these two cells having a higher maximum power point (P_{max}), as clearly illustrated in Figures 4.43d-f. It is also worth noting that the cell efficiencies for all tested solar cells under dark conditions were less than 1%.

Comparing the results presented here with the studies presented in the dissertation [24], it can be seen that for cells containing perovskite with iodine, the FF coefficients were higher,

amounting to about 50%. The efficiency of a solar cells with a similar structure and an active layer of $MAPbI_3$, calculated by SCAPS simulations, is about 23% [25]. Results of other SCAPS-based simulations [26] for perovskite solar cells with a $MAPbCl_3$ thin film indicate that their efficiency can reach up to ~21%. In contrast, experimental data for solar cells with $MAPbBr_3$ thin active layer report efficiencies in the range of 2-5% [27]. The experimental results for Br.1 obtained in this study are comparable to those presented in [27]. Apparent discrepancies are observed, however, when comparing experimental results with simulation outcomes. The experimental efficiencies achieved here for devices with I.1 and Cl.1 are significantly lower than those predicted by simulations.

The results obtained in this section are exciting. They confirm that thin films of hybrid perovskites $MAPbI_3$, $MAPbCl_3$, and $MAPbBr_3$ respond well to light, and that solar cells containing these perovskite active thin films can generate voltage. It turns out that, despite the lowest stability of perovskite thin films with chloride anion, solar cells with this active layer work very well under laboratory conditions, achieving the highest FF but the lowest efficiency among the studied photovoltaic solar cells. The efficiencies of the devices with Br.1 and I.1 are comparable. I.1 perovskites are popular materials in scientific research, and it was initially expected that cells with I.1 would be the most efficient. However, it is also interesting to note that the cell with I.1 is most responsive to light, as seen in Figure 4.43a, where the dark and light characteristics are compared. In the context of the stability of perovskite materials and their application in solar technology, aging tests of perovskite thin film photovoltaic cells should be carried out. On this basis, the usefulness of the tested perovskites in photovoltaics should be resolved.

References

1. G. Rose, Beschreibung Einiger Neuen Mineralien Des Urals. *Ann. Phys.* (1839) 124, 551–573, https://doi.org/10.1002/andp.18391241205
2. D. Weber *et al.* CH3NH3PbX3, ein Pb(II)-System mit kubischer Perowskitstruktur/CH3NH3PbX3, a Pb(II)-System with Cubic Perovskite Structure. *Z. Naturforsch. B* (1978) 33, 1443–1445, https://doi.org/10.1515/znb-1978-1214
3. A. Kojima *et al.* Organometal Halide Perovskites as Visible-Light Sensitizers for Photovoltaic Cells. *J. Am. Chem. Soc.* (2009), 131, 6050–6051, https://doi.org/10.1021/ja809598r
4. J. Liu *et al.* Perovskite/silicon tandem solar cells with bilayer interface passivation. *Nature* (2024) 635, 596–603, https://doi.org/10.1038/s41586-024-07997-7
5. S. Mirershadi *et al.* Third order nonlinear optical properties of organometal halide perovskite by means of the Z-scan technique. *Chem. Phys. Lett.* (2016) 647, 7–13, https://doi.org/10.1016/j.cplett.2016.01.041
6. P.S. Whitfield *et al.* Structures, phase transitions and tricritical behavior of the hybrid perovskite methyl ammonium lead iodide. *Sci. Rep. 6* (2016) 35685, https://doi.org/10.1038/srep35685
7. F. Yongping *et al.* Incorporating Large A Cations into Lead Iodide Perovskite Cages: Relaxed Goldschmidt Tolerance Factor and Impact on Exciton–Phonon Interaction. *ACS Cent. Sci.* (2019) 5, 8, 1377–1386, https://doi.org/10.1021/acscentsci.9b00367
8. Z. Ying *et al.* Synchrotron-Based X-Ray-Sensitive Nanoprobes for Cellular Imaging. *Adv. Mat.* 26, 46, Special Issue:Synchrotron Light for Materials Science, (2014) 7889-7895, https://doi.org/10.1002/adma.201304281
9. S.D. Stranks *et al.* Electron-Hole Diffusion Lengths Exceeding 1 Micrometer in an Organometal Trihalide Perovskite Absorber.. *Science* (2013) 342, 341-344, DOI:10.1126/science.1243982
10. L. Shiqiang *et al.* The influence of chloride on interdiffusion method for perovskite solar cells. *Mat. Lett.* (2016) 169, 236-240, https://doi.org/10.1016/j.matlet.2016.01.114

11. J. Hidalgo *et al.* Imaging and Mapping Characterization Tools for Perovskite Solar Cells. *Adv. Energy Mater.* (2019), 9, 1900444, https://doi.org/10.1002/aenm.201900444
12. M.A. Green *et al.* Optical Properties of Photovoltaic Organic–Inorganic Lead Halide Perovskites. *Phys. Chem. Lett.* (2015) 6, 4774–4785, https://doi.org/10.1021/acs.jpclett.5b01865
13. https://www.orientjchem.org/staging/vol40no4/advances-in-methylammonium-lead-halide-perovskites-synthesis-structural-optical-and-photovoltaic-insights/, access: 1.06.2025
14. D. Zhang *et al.* Degradation pathways in perovskite solar cells and how to meet international standards. *Commun Mater* (2022) 3, 58, https://doi.org/10.1038/s43246-022-00281-z
15. N. Calisi *et al.* Composition-Dependent Degradation of Hybrid and Inorganic Lead Perovskites in Ambient Conditions. *Top Catal* (2018) 61, 1201–1208, https://doi.org/10.1007/s11244-018-0922-5
16. B. Kim *et al.* First-principles identification of the charge-shifting mechanism and ferroelectricity in hybrid halide perovskites. *Sci. Rep.* (2020) 10, 19635, https://doi.org/10.1038/s41598-020-76742-7
17. M. Keshavarz *et al.* Tracking Structural Phase Transitions in Lead-Halide Perovskites by Means of Thermal Expansion. *Adv. Mater.* (2019) 31, 1900521, https://doi.org/10.1002/adma.201900521
18. W. Kong *et al.* Characterization of an abnormal photoluminescence behavior upon crystal-phase transition of perovskite CH3NH3PbI3. *Phys. Chem.* (2015) 17, 16405, DOI https://doi.org/10.1039/C5CP02605A
19. C.C. Stoumpos *et al.* Germanium Iodide Perovskite Semiconductors: Active Lone Pairs, Structural Distortions, Direct and Indirect Energy Gaps, and Strong Nonlinear Optical Properties. *J. Am. Chem. Soc.* (2015) 137, 6804–6819, https://doi.org/10.1021/jacs.5b01025
20. Y. Zhou *et al.* Nonlinear optical properties of halide perovskites and their applications. *Appl. Phys. Rev.* (2020) 7, 041313, https://doi.org/10.1063/5.0025400

21. I. Abdelwahab *et al.* Highly Enhanced Third-Harmonic Generation in 2D Perovskites at Excitonic Resonances. *ACS Nano* (2018) 12, 644–650, https://doi.org/10.1021/acsnano.7b07698
22. S. Mirershadi *et al.* Third order nonlinear optical properties of organometal halide perovskite by means of the Z-scan technique. *Chem. Phys. Lett.* (2016) 647, 7–13, https://doi.org/10.1016/j.cplett.2016.01.041
23. R. Ganeev *et al.* Strong nonlinear absorption in perovskite films. *Opt. Mater. Express* (2018) 8(6):1472-1483, DOI: 10.1364/OME.8.001472
24. A. Zawadzka *et al.* Low-temperature influence on the properties and efficiency of thin-film perovskite solar cells fabricated by the PVco-D technique. *Sol. Energy Mater. Sol. Cells* (2024) 274, 112993, https://doi.org/10.1016/j.solmat.2024.112993
25. N. Nowshad *et al.* Photovoltaic performance analysis of CH3NH3PbI3 perovskite solar cell using SCAPS simulation. *Chemistry of Inorganic Materials* (2025) 6, 100107, https://doi.org/10.1016/j.cinorg.2025.100107
26. P. Sarkar *et al.* Polyvinylpyrrolidone capped electrospun CH3NH3PbCl3 perovskite film as the electron transport layer in perovskite solar cell application. *Solar Energy* (2021) 230(33):390-400, DOI: 10.1016/j.solener.2021.10.053
27. H. Mehdi *et al.* MAPbBr3 perovskite solar cells via a two-step deposition process. *RSC Adv.* (2019) 9, 12906-12912, https://doi.org/10.1039/C9RA02036E

SUMMARY

This monograph presents research on the optoelectronic properties (photovoltaic and nonlinear optical effects) and structural properties of thin films of selected hybrid perovskites. The goals of this work were to develop a technique for fabricating perovskite structures using PVco-D, to investigate the effect of perovskite composition on linear and nonlinear optical and structural properties, to determine the potential of the studied materials in the field of photovoltaics, to fabricate a complete photovoltaic cell structure, and to investigate its fundamental photovoltaic parameters. In a broader sense, all of the aforementioned goals of this work are intended to accelerate the development and commercialization of perovskite optoelectronic devices.

The studies are divided based on the analyzed properties: structural studies, UV-VIS-NIR spectroscopic studies, aging tests, phase transition studies, nonlinear optical effects (SHG, THG, Z-scan), and photovoltaic properties. Each section describes results for three groups of perovskites: iodide, chloride, and bromide. This approach aims to compare a given property among different perovskite structures.

The first stage of the study was to develop a technique for depositing perovskites using the PVco-D method. Perovskite materials were selected for the study to compare the effect of crystal structure on optoelectronic parameters. Therefore, the perovskites described in this work consist of an organic methylammonium iodide, chloride, or bromide, and an inorganic moiety of iodide, chloride, or bromide, respectively. These perovskites are $MAPbI_3$, $MACdI_3$, $MAGeI_3$, $MASnI_3$, $MAZnI_3$, $MAPbCl_3$, $MAPbBr_3$, and $MASnBr_3$. Furthermore, using the PVco-D technique, the selected samples were prepared in three versions, differing in the percentage of organic and inorganic components.

In the following steps, the topographic properties of perovskite thin films were described, based on the AFM results. The focus was on characterizing the structures forming the film, determining the RMS parameter defining the film roughness, determining the average crystallite height, and performing MFs analysis. Based on this, it was concluded that the most uniform surfaces were obtained for perovskites with I and Br halogens, particularly for the compositions of 50% organic part : 50% inorganic part

and 70% organic part : 30% inorganic part. At the same time, the poorest topographic quality was observed for samples with Cl halogen.

Spectroscopic studies provide information about the optical properties of the materials in the UV-VIS-NIR range. The strongest absorption is observed in $MAPbI_3$ and $MASnI_3$ samples, while the weakest is in Cl-based perovskites. All tested samples demonstrate an influence of absorption on the nonlinear optics studies conducted in subsequent stages. Furthermore, the results suggest that I-based perovskites are more suitable for photovoltaic applications, while Cl and Br-based perovskites are more suitable for broadly defined optoelectronics applications.

Aging tests confirm that perovskites are materials that degrade rapidly, which limits their application potential. The results presented in this dissertation were based on studies conducted over six months following sample acquisition and demonstrate the effect of storing thin film perovskite samples in the dark and an argon atmosphere on their optical and structural parameters. The obtained results indicate that the most resistant to external factors are samples containing I and Br halogens, particularly samples I.1, Br.1, and Br.3, whose optical and structural parameters change only slightly over six months. Samples containing Cl halogen are most susceptible to degradation, which poses a potential threat to further applications.

The next part of the perovskite research focused on detecting phase transitions. Measurements were made using two methods over a wide temperature range of 80 – 310 K, with 10 K steps. The obtained results confirm changes in the crystallographic structure in the studied perovskite materials. The determined temperatures or temperature ranges of the phase transitions vary depending on the perovskite composition. However, for all samples tested in the phase transition range, phase transitions from the orthorhombic phase to the tetragonal phase and from the tetragonal phase to the cubic phase were detected.

NLO studies (SHG, THG, Z-scan) focused primarily on determining the suitability of perovskite thin films for nonlinear optics and the effect of perovskite composition on the resulting NLO response. Only a few studied materials exhibited minor second-order nonlinear effects (SHG), so the CP technique enhanced the SHG signal. This goal was

achieved. However, the SHG response, even after CP, was typically smaller than the SHG of the reference material. The SHG response after CP was repeated after two weeks to verify whether the CP effect was still present. The results indicate that the nonlinear SHG response decreases, but the materials are still helpful for second-harmonic generation. The strongest and most stable SHG effects were observed for bromide perovskites. Third-order nonlinearity (THG) studies show that all tested perovskite materials exhibit strong third-order optical nonlinearity, and the THG values obtained are significantly higher than those determined for the reference material. The third experiment related to NLO studies, i.e., Z-scan, was conducted only for perovskites with halogen I and one perovskite with Cl. Satisfactory results were obtained only for three materials tested in this respect. These results showed that the samples with halogen I (I.1, I.4) exhibit strong saturable absorption (SA). In contrast, the sample with halogen Cl (Cl.1) exhibits reverse saturable absorption (RSA).

In the final stage of research, three prototypes of perovskite photovoltaic cells were designed and constructed with selected thin perovskite layers: I.1, Cl.1, and Br.1. The entire solar cell was fabricated on a glass substrate, and all individual thin layers constituting the cell were deposited using PVD or PVco-D techniques. Measurements of electrical properties (dark and light I-V characteristics) showed that the cell with the $MAPbI_3$ (I.1) perovskite active layer had the strongest light sensitivity. For this cell, the FF parameter was 22.61%. Cells with $MAPbCl_3$ (Cl.1) and $MAPbBr_3$ (Br.1) achieved FF equal to 44.52% and 31.44%, respectively. In both cases, the cell's light sensitivity was lower than that of the I.1 cell. In the context of the achieved efficiencies, the solar cell with I.1 reached 3.43%, the solar cell with Cl.1 reached 2.80%, and with Br.1, 3.55%.

In summary, the primary research objectives of this work have been achieved. A technique for depositing thin film perovskite structures of various compositions using the PVco-D method was developed, the effect of perovskite composition on structural, optical, and photovoltaic properties was investigated, aging tests were conducted, and prototypes of perovskite photovoltaic cells were fabricated. This work provides significant information on fundamental optoelectric properties and phase transitions and can be a starting point for further research in perovskite technologies. Additional research related to perovskite structures may address the chemical and structural stability of perovskites, including methods

for protecting perovskite structures from the negative effects of environmental factors, so that they can be successfully used in photovoltaics. Other directions of perovskite research should focus on their application in nonlinear optics. Perovskites exhibit strong third-order nonlinear properties and can generate second-order nonlinear optical effects, some exhibiting SA and RSA. The potential applications in nonlinear optics are enormous, and subsequent research should include a thorough analysis of NLO using quantum chemical simulations. Furthermore, due to toxic elements in the tested samples, future efforts should be made to replace these harmful components with more sustainable and environmentally friendly compounds.

LIST OF FIGURES

CHAPTER 1

CHAPTER 2

CHAPTER 3

CHAPTER 4

LIST OF TABLES

CHAPTER 1

CHAPTER 4

LIST OF PUBLICATIONS

1. El-Marbet, M.; Bouich, A.; Tarbi, A.; Chtouki, T.; Erguig, H.; Zawadzka, A.; **Marjanowska, A.**; Migalska-Zalas, A.; Kityk, A.; Andruschchak, A.; Myronchuk, G.; Sahraoui, B Advancing solar cell efficiency: insights from cesium lead halide perovskite analysis. *Journal of Materials Science: Materials in Electronics* (2025) 36, 1759, https://doi.org/10.1007/s10854-025-15827-3
2. Hachimi, M.A.; Tarbi, A.; El-Marbet, M.; Erguig, H.; Zawadzka, A.; **Marjanowska, A.**; Płóciennik, P.; Kityk, A.V.; Sahraoui, B. Combined experimental and numerical approach for the optimization of double Cs2AgBiBr6 perovskite solar cells: Ab initio study, simulation and performance comparison. *Solid State Sciences*, (2025) 169, 108101, https://doi.org/10.1016/j.solidstatesciences.2025.108101
3. Hachimi, M.A.; Tarbi, A.; El-Marbet, M.; Erguig, H.; Zawadzka, A.; **Marjanowska, A.**; Płóciennik, P.; Kityk, A.V.; Sahraoui, B. Structural, Electronic, Mechanical, and Optical Properties of X3OCl (X = Li, Na, K) Antiperovskites: An Ab-Initio Study for Energy Applications. *Physica B: Condensed Matter* (2025) S0921-4526(25)00869-5, https://doi.org/10.1016/j.physb.2025.417752
4. Hachimi, M.A.; Tarbi, A.; El-Marbet, M.; Erguig, H.; Zawadzka, A.; **Marjanowska, A.**; Płociennik, P.; Kityk, A.V.; Sahraoui, B. DFT and device simulation of KGeCl3 perovskite: A dual-function material for solar energy and hydrogen storage. *Int. J. Hydrogen Energy* (2025) 169, 151106, https://doi.org/10.1016/j.ijhydene.2025.151106
5. Tarbi, A.; Erguig, H; Sellam, M.A.; Zawadzka, A.; **Marjanowska, A.**; Migalska-Zalas, A.; Goncharova, I.; Myronchuk, G.; Kityk, A.V.; Sahraoui, B. Diagnostics of the stability of CsPbX3 (X = Cl, Br, and I) inorganic halide perovskites for photovoltaic applications: An in-depth review with an original contribution on impedance characterization. *Renew. Sust. Energ. Rev.* (2026) 226, 116234. https://doi.org/10.1016/j.rser.2025.116234
6. **Marjanowska, A.**; Wisniewski, K.; Sahraoui, B.; Zawadzka, A. Phase Transitions in Halide Perovskite Thin Films Fabricated by PVco-D Method. *25th International Conference on Transparent Optical Networks,* ICTON 2025, Barcelona, Spain,

6-10 July 2025: conference proceedings (2025) Danvers, IEEE. DOI: 10.1109/ICTON67126.2025.11125021

7. Płóciennik, P.; Zawadzka, A.; Laouid, A.; Mientki, M.; **Marjanowska, A.**; Łukasiak, Z. Physical vacuum co-deposition (PVco-D) method for various thin film materials. *25th International Conference on Transparent Optical Networks*, ICTON 2025, Barcelona, Spain, 6-10 July 2025: conference proceedings (2025) Danvers, IEEE. DOI: 10.1109/ICTON67126.2025.11125176
8. Zawadzka, A.; **Marjanowska, A.**; Płóciennik, P.; Laouid, A.; Mientki, M. Electron Transport Layers for Perovskite Solar Cells. *25th International Conference on Transparent Optical Networks*, ICTON 2025, Barcelona, Spain, 6-10 July 2025: conference proceedings (2025) Danvers, IEEE. doi: 10.1109/ICTON67126.2025.11125082
9. **Marjanowska, A.**; Wiśniewski, K.; Płóciennik, P.; Sahraoui, B.; Zawadzka, A. Role of Composition and Temperature in Shaping the Structural and Optical Properties of Iodide-Based Hybrid Perovskite Thin Films Produced by PVco-D Technique. *Materials* (2025) 18, 1336. https://doi.org/10.3390/ma18061336
10. **Marjanowska, A.**; Zawadzka, A.; El Karout, H.; Sahraoui, B. Protective Layer Engineering: Impact of SnO_2 and PbI_2 on the Optical Parameters and Stability of Hybrid Perovskite Thin Films. *Molecular Crystals and Liquid Crystals GMCL* (2025) Nanotechnologies and Nanomaterials NANO-2023. DOI:10.1080/15421406.2025.2458934
11. **Marjanowska, A.**; El Karout, H.; Zawadzka, A.; Płóciennik, P.; Guichaoua, D.; Sahraoui, B. Argon Environment Influence on Perovskite Thin Film Durability. *24th International Conference on Transparent Optical Networks*, ICTON 2024, Bari, Italy, 14-18 July 2024: conference proceeding (2024) Danvers, IEEE. DOI:10.1109/ICTON62926.2024
12. El Karout, H.; **Marjanowska, A.**; Zawadzka, A.; Płóciennik, P.; Andruschak, A.; Wielgosz, R.; Sahraoui, B. Unveiling the nonlinear optical potential of N719 dye-based thin film. *24th International Conference on Transparent Optical Networks*, ICTON 2024, Bari, Italy, 14-18 July 2024: conference proceedings (2024) Danvers, IEEE. DOI:10.1109/ICTON62926.2024

13. Zawadzka, A.; **Marjanowska, A.**; Laouid, A.; Wiśniewski, K.; Zawadzki, M.; Płócennik, P. Low-temperature perovskites thin films solar cell. *24th International Conference on Transparent Optical Networks*, ICTON 2024, Bari, Italy, 14-18 July 2024: conference proceedings (2024) Danvers, IEEE. DOI:10.1109/ICTON62926.2024
14. Płóciennik, P.; Zawadzka. A.; El Ouedghiri Idrissi, I.; Sofiani, Z.; Wiśniewski, K.; Laouid, A.; **Marjanowska A.**; Łukasiak, Z. ZnO-based thin-film transparent contacts for applications in perovskite solar cells. *24th International Conference on Transparent Optical Networks*, ICTON 2024, Bari, Italy, 14-18 July 2024: conference proceedings (2024) Danvers, IEEE. DOI:10.1109/ICTON62926.2024
15. Zawadzka, A.; **Marjanowska, A.**; Laouid, A; Wiśniewski, K; El Kouari, Y.; Płóciennik, P. Low-temperature influence on the properties and efficiency of thin-film perovskite solar cells fabricated by the PVco-D technique. *Solar Energy Materials and Solar Cells* (2024) 274, 112993. DOI: 10.1016/j.solmat.2024.112993
16. **Marjanowska, A.**; El Karout, H.; Guichaoua, D.; Sahraoui, B.; Płóciennik, P.; Zawadzka, A. Topography and Nonlinear Optical Properties of Thin Films Containing Iodide-Based Hybrid Perovskites. *Nanomaterials* (2024) 14, 1, 50. https://doi.org/10.3390/nano14010050
17. **Marjanowska, A.**; Zawadzka, A.; Sahraoui, B.; Guichaoua, D.; Płóciennik, P. Perovskite Thin Films for Optoelectronic Devices: Study of Their Stability. *23rd International Conference on Transparent Optical Networks,* ICTON 2023 (2023) IEEE. DOI:10.1109/ICTON59386.2023.10207408
18. Zawadzka, A.; **Marjanowska, A.**; Płóciennik, P.; Korcala, A.; Wiśniewski, K.; Sahraoui, B. Properties and applications of hybrid organic-inorganic halide perovskites thin films. *SPIE Organic Photonic Materials and Devices XXII.* 2020, Proc. SPIE 11277, 112770S. DOI:10.1117/12.2545957
19. Zawadzka, A.; **Marjanowska, A.**; Płóciennik, P.; Korcala, A.; Wiśniewski, K. Photophysical Properties of Metal Halide Perovskite Thin Films. IEEE. 2019, *21st International Conference on Transparent Optical Networks*, ICTON 2019. DOI:10.1109/ICTON.2019.8840299

LIST OF ORAL PRESENTATIONS

1. **Marjanowska, A.**; Wisniewski, K.; Sahraoui, B.; Zawadzka, A. Phase Transitions in Halide Perovskite Thin Films Fabricated by PVco-D Method. *International Conference on Transparent Optical Networks* (ICTON) (July 2025) Barcelona, Spain
2. **Marjanowska, A.**; El Karout, H.; Zawadzka, A.; Guichaoua, D.; Płóciennik, P.; Sahraoui, B. Argon Encapsulation: Safeguarding Perovskite Thin Films from Degradation. *12th International Conference on "Nanotechnologies and Nanomaterials"* NANO-2024 (August 2024) Uzhorod, Ukraine
3. **Marjanowska, A.**; El Karout, H.; Zawadzka, A.; Płóciennik, P.; Guichaoua, D.; Sahraoui, B. Argon Environment Influence on Perovskite Thin Film Durability. *International Conference on Transparent Optical Networks (*ICTON) (July 2024) Bari, Italy
4. **Marjanowska, A.**; El Karout, H.; Zawadzka, A.; Płóciennik, P.; Guichaoua, D.; Sahraoui, B. Argon Atmosphere: A Protective Shield for Perovskite Thin Films. *JED 3MG* (June 2024) Angers, France
5. **Marjanowska, A.**; Zawadzka, A.; El Karout, H.; Sahraoui, B. Diagnostic of the Role of SnO2 and PbI2 in Enchancing the Stability of Perovskite Thin Films. *11th International Conference on "Nanotechnologies and Nanomaterials"* NANO-2023 (August 2023) Bukovel, Ukraine
6. **Marjanowska, A.**; Zawadzka, A.; Sahraoui, B.; Płóciennik, P. Perovskite Thin Films for Optoeletronic Devices: Study of Their Stability. *International Conference on Transparent Optical Networks* (ICTON) (July 2023) Bucharest, Romania
7. **Marjanowska, A.**; Płóciennik, P.; Wiśniewski, K.; Zawadzka, A. Przejścia Fazowe w Cienkich Warstwach Perowskitowych. *XV Kopernikańskie Seminarium Doktoranckie* (June 2022) Toruń, Poland
8. **Marjanowska, A.**; Płóciennik, P.; Wiśniewski, K.; Zawadzka, A. Cienkowarstwowe Ogniwa Fotowoltaiczne na Bazie Perowskitów. *XIV Kopernikańskie Seminarium Doktoranckie* (September 2021) Toruń, Poland

LIST OF POSTERS

1. **Marjanowska, A.**; Wisniewski K.; Mientki, M.; Zawadzka, A. Influence of Composition on the Structural and Optical Properties of Hybrid Perovskite Thin Films. *International Nano-Optoelectronics Workshop* (iNOW), 21-31 July 2025, Wrocław, Poland
2. **Marjanowska, A.**; Zawadzka, A.; Sahraoui, B.; Płóciennik, P. Badanie Stabilności Cienkich Warstw Perowskitowych. *XVI Kopernikańskie Seminarium Doktoranckie*, 6 June 2023, Toruń, Poland
3. **Marjanowska, A.**; Zawadzka, A.; Sahraoui, B.; Płóciennik, P. Stability of Perovskite Thin Films for Use in Optoelectronic Devices. *JED 3MG*, May 2023, Nantes, France

COLLEGE DOCTORAL PAYS DE LA LOIRE
ED MATIERE, MOLECULES MATERIAUX ET GEOSCIENCES

université angers

NICOLAUS COPERNICUS UNIVERSITY IN TORUŃ
Doctoral Schools

Title: **Photovoltaic and nonlinear optical effects of thin films based on perovskites**

Keywords: hybrid perovskites, perovskite solar cells, nonlinear optics, phase transition, perovskite stability, thin films

Abstract: Perovskites are a group of materials discovered in the 19th century, whose optoelectronic potential has yet to be fully realized. Over the past two decades, their structural properties, linear and nonlinear optical properties, and photovoltaic characteristics have been intensively studied. The results indicate that these materials, due to their unique photovoltaic and nonlinear properties, represent a promising class of compounds for optoelectronic applications.

This dissertation studies selected thin film hybrid perovskites with the $MABX_3$ structure, where B = Pb, Cd, Ge, Sn, Zn, and X = I, Cl, Br. The materials were synthesized by physical vapor co-deposition (PVco-D) and then characterized using a variety of techniques, including atomic force microscopy (AFM), UV-VIS-NIR spectrophotometry, photoluminescence (PL) spectroscopy, second- and third-harmonic generation (SHG, THG), Z-scan, and electrical and photovoltaic measurements. These studies provided detailed information on the effect of chemical composition and composition percentage on the surface topography, structural stability, linear and nonlinear optical properties, and electrical parameters of perovskite solar cells. The studies demonstrated that the stability of perovskites strongly depends on their chemical composition, with materials containing I and Br atoms proving to be the most stable. Spectroscopic measurements over a wide temperature range confirmed the occurrence of phase transitions – from orthorhombic to tetragonal and from tetragonal to cubic. The strongest second-order nonlinear properties were observed for the perovskite containing the Br halogen. Third-order nonlinear effects were observed for all tested materials. Thin film photovoltaic cells with perovskites containing I, Cl, and Br halogens responded to illumination by generating an electrical voltage and achieving efficiencies of 3.43%, 2.80%, and 3.55%, respectively. These research results emphasize the crucial role of optimizing perovskites' chemical and structural composition in developing new materials for future optoelectronic and photovoltaic applications.

COLLEGE ED MATIERE, MOLECULES
DOCTORAL MATERIAUX ET
PAYS DE LA LOIRE GEOSCIENCES

université angers

NICOLAUS COPERNICUS UNIVERSITY IN TORUŃ
Doctoral Schools

Tytuł: **Fotowoltaiczne i nieliniowe efekty optyczne cienkich warstw perowskitów**

Słowa kluczowe: perowskity hybrydowe, perowskitowe ogniwa słoneczne, optyka nieliniowa, przejście fazowe, stabilność perowskitów, cienkie warstwy

Streszczenie: Perowskity to grupa materiałów odkryta w XIX wieku, której potencjał optoelektroniczny wciąż nie został w pełni wykorzystany. W ostatnich dwóch dekadach intensywnie badane są ich właściwości strukturalne, liniowe i nieliniowe właściwości optyczne oraz charakterystyka fotowoltaiczna. Uzyskane wyniki wskazują, że materiały te, ze względu na unikalne właściwości fotowoltaiczne i nieliniowe, stanowią obiecującą klasę związków w zastosowaniach optoelektronicznych.

Niniejsza rozprawa poświęcona jest badaniom wybranych cienkowarstwowych perowskitów hybrydowych o strukturze $MABX_3$, gdzie B = Pb, Cd, Ge. Sn, Zn, a X = I, Cl, Br. Materiały otrzymano techniką fizycznego współosadzania z fazy gazowej (PVco-D), a następnie scharakteryzowano przy użyciu szeregu technik, takich jak mikroskopia sił atomowych (AFM), spektrofotometria UV-VIS-NIR, spektroskopia fotoluminescencyjna (PL), generacja drugiej i trzeciej harmonicznej (SHG, THG), metoda Z-scan oraz pomiary elektryczne i fotowoltaiczne. Badania te dostarczyły szczegółowych informacji na temat wpływu składu chemicznego i kompozycji procentowej na topografię powierzchni, stabilność strukturalną, liniowe i nieliniowe właściwości optyczne oraz parametry elektryczne perowskitowych ogniw słonecznych. Badania wykazały, że stabilność perowskitów silnie zależy od ich składu chemicznego – najbardziej stabilne okazały się materiały zawierające atomy I i Br. Pomiary spektroskopowe w szerokim zakresie temperatur potwierdziły występowanie przejść fazowych – z fazy rombowej do tetragonalnej i z fazy tetragonalnej do kubicznej. Najsilniejsze właściwości nieliniowe drugiego rzędu zaobserwowano dla perowskitu z halogenem Br. Nieliniowe efekty trzeciego rzędu zaobserwowano dla wszystkich badanych materiałów. Cienkowarstwowe ogniwa fotowoltaiczne z perowskitami zawierającymi halogeny I, Cl i Br reagowały na oświetlenie generując napięcie elektryczne i osiągając sprawności odpowiednio: 3.43%, 2.80% i 3.55%. Otrzymane wyniki badań podkreślają kluczową rolę optymalizacji składu chemicznego i strukturalnego perowskitów w rozwoju nowych materiałów dla przyszłych zastosowań optoelektronicznych i fotowoltaicznych.

COLLEGE DOCTORAL PAYS DE LA LOIRE — ED MATIERE, MOLECULES MATERIAUX ET GEOSCIENCES

université angers

NICOLAUS COPERNICUS UNIVERSITY IN TORUŃ Doctoral Schools

Titre: **Effets optiques photovoltaiques et effet optique non linéaires de films minces à base de pérovskites**

Mots clés: pérovskites hybrides, cellules solaires à pérovskite, optique non linéaire, transition de phase, stabilité des pérovskites, couches minces

Résumé: Les pérovskites sont un groupe de matériaux découverts au XIXe siècle, dont le potentiel optoélectronique n'a pas encore été pleinement exploité. Au cours des deux dernières décennies, leurs propriétés structurales, leurs propriétés optiques linéaires et non linéaires, ainsi que leurs caractéristiques photovoltaïques ont fait l'objet d'études approfondies. Les résultats indiquent que ces matériaux, grâce à leurs propriétés photovoltaïques et non linéaires uniques, représentent une classe de composés prometteuse pour les applications optoélectroniques.

Cette thèse étudie une sélection de pérovskites hybrides en couches minces de structure $MABX_3$, où B = Pb, Cd, Ge, Sn, Zn et X = I, Cl, Br. Les matériaux ont été synthétisés par codéposition physique en phase vapeur (PVco-D), puis caractérisés à l'aide de diverses techniques, notamment la microscopie à force atomique (AFM), la spectrophotométrie UV-VIS-NIR, la spectroscopie de photoluminescence (PL), la génération de deuxième et troisième harmoniques (SHG, THG), la technique Z-scan, ainsi que des mesures électriques et photovoltaïques. Ces études ont fourni des informations détaillées sur l'effet de la composition chimique et de la proportion des constituants sur la topographie de surface, la stabilité structurelle, les propriétés optiques linéaires et non linéaires, ainsi que sur les paramètres électriques des cellules solaires à pérovskites. Les résultats ont montré que la stabilité des pérovskites dépend fortement de leur composition chimique, les matériaux contenant des atomes d'I et de Br étant les plus stables. Des mesures spectroscopiques sur une large gamme de températures ont confirmé l'apparition de transitions de phase – de l'orthorhombique au tétragonale et du tétragonale au cubique. Les propriétés non linéaires du second ordre les plus marquées ont été observées pour la pérovskite contenant l'halogène Br. Des effets non linéaires du troisième ordre ont été observés pour tous les matériaux testés. Les cellules photovoltaïques en couches minces à base de pérovskites contenant les halogènes I, Cl et Br ont réagi à l'illumination en générant une tension électrique et en atteignant des rendements respectifs de 3.43%, 2.80% et 3.55%. Ces résultats de recherche soulignent le rôle déterminant de l'optimisation de la composition chimique et structurelle des pérovskites dans le développement de nouveaux matériaux destinés aux futures applications optoélectroniques et photovoltaiques.